



HELLENIC REPUBLIC  
UNIVERSITY OF IOANNINA  
SCHOOL OF ENGINEERING  
DEPARTMENT OF MATERIALS SCIENCE AND ENGINEERING

Design and Study of Pillared Graphenes and Nanoporous Carbon Materials for Energy,  
Environmental and Catalytic Applications

Eleni Thomou

DOCTORAL THESIS

Ioannina, 2021





ΕΛΛΗΝΙΚΗ ΔΗΜΟΚΡΑΤΙΑ  
ΠΑΝΕΠΙΣΤΗΜΙΟ ΙΩΑΝΝΙΝΩΝ  
ΠΟΛΥΤΕΧΝΙΚΗ ΣΧΟΛΗ  
ΤΜΗΜΑ ΜΗΧΑΝΙΚΩΝ ΕΠΙΣΤΗΜΗΣ ΥΛΙΚΩΝ

Σχεδιασμός και μελέτη υποστηλωμένων γραφενίων και νανοπορωδών υλικών άνθρακα για ενεργειακές, περιβαλλοντικές και καταλυτικές εφαρμογές

Ελένη Θώμου

ΔΙΔΑΚΤΟΡΙΚΗ ΔΙΑΤΡΙΒΗ

Ιωάννινα, 2021

«Η έγκριση της διδακτορικής διατριβής από το Τμήμα Μηχανικών Επιστήμης Υλικών της Πολυτεχνικής Σχολής του Πανεπιστημίου Ιωαννίνων δεν υποδηλώνει αποδοχή των γνώμων του συγγραφέα Ν. 5343/32, άρθρο 202, παράγραφος 2».

**Ημερομηνία αίτησης της κ. Ελένης Θώμου:** 18/7/2016

**Ημερομηνία ορισμού Τριμελούς Συμβουλευτικής Επιτροπής:** 5/10/2016

**Μέλη Τριμελούς Συμβουλευτικής Επιτροπής:**

Επιβλέπων: Δημήτριος Γουρνής, Καθηγητής του Τμήματος Μηχανικών Επιστήμης Υλικών της Πολυτεχνικής Σχολής του Πανεπιστημίου Ιωαννίνων

Μέλη

Μιχαήλ Καρακασίδης, Καθηγητής του Τμήματος Μηχανικών Επιστήμης Υλικών της Πολυτεχνικής Σχολής του Πανεπιστημίου Ιωαννίνων

Γεώργιος Ρωμανός, Διευθυντής ερευνών του Ινστιτούτου Νανοεπιστήμης και Νανοτεχνολογίας του ΕΚΕΦΕ «Δημόκριτος»

**Ημερομηνία ορισμού θέματος:** 5/10/2016

Σχεδιασμός και μελέτη υποστηλωμένων γραφενίων και νανοπορωδών υλικών άνθρακα για ενεργειακές, περιβαλλοντικές και καταλυτικές εφαρμογές

**ΔΙΟΡΙΣΜΟΣ ΕΠΤΑΜΕΛΟΥΣ ΕΞΕΤΑΣΤΙΚΗΣ ΕΠΙΤΡΟΠΗΣ:** 6/10/2021

<b>Δημήτριος Γουρνής</b>	Καθηγητής του Τμήματος Μηχανικών Επιστήμης Υλικών της Πολυτεχνικής Σχολής του Πανεπιστημίου Ιωαννίνων
<b>Μιχαήλ Καρακασίδης</b>	Καθηγητής του Τμήματος Μηχανικών Επιστήμης Υλικών της Πολυτεχνικής Σχολής του Πανεπιστημίου Ιωαννίνων
<b>Γεώργιος Ρωμανός</b>	Διευθυντής ερευνών του Ινστιτούτου Νανοεπιστήμης και Νανοτεχνολογίας του ΕΚΕΦΕ «Δημόκριτος»
<b>Petra Rudolf</b>	Καθηγήτρια του Zernike Institute for Advanced Materials του University of Groningen
<b>Αλκιβιάδης Παϊπέτης</b>	Καθηγητής του Τμήματος Μηχανικών Επιστήμης Υλικών της Πολυτεχνικής Σχολής του Πανεπιστημίου Ιωαννίνων
<b>Θεόδωρος Στεριώτης</b>	Διευθυντής ερευνών του Ινστιτούτου Νανοεπιστήμης και Νανοτεχνολογίας του ΕΚΕΦΕ «Δημόκριτος»
<b>Παντελής Τρικαλίτης</b>	Καθηγητής του Τμήματος Χημείας της Σχολής Θετικών και Τεχνολογικών Επιστημών του Πανεπιστημίου Κρήτης

Έγκριση Διδακτορικής Διατριβής με βαθμό «ΑΡΙΣΤΑ» στις 3/12/2021

**Ο Πρόεδρος του Τμήματος**



**Απόστολος Αυγερόπουλος**  
Καθηγητής



**Η Γραμματέας του Τμήματος**



**Μαρία Κόντου**

**Date of application of Ms. Eleni Thomou:** 18/7/2016

**Date of appointment of the three-membered advisory committee:** 5/10/2016

**Members of the three-membered advisory committee:**

Supervisor: Dimitrios Gournis, professor of the Department of Materials Science and Engineering, School of Engineering, University of Ioannina

Members

Michael Karakassides, Professor of the Department of Materials Science and Engineering, School of Engineering, University of Ioannina

Georgios Romanos, Research Director, Institute of Nanoscience and Nanotechnology, NCSR “Demokritos”

**Thesis definition date:** 5/10/2016

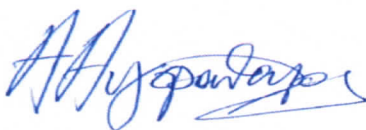
Design and Study of Pillared Graphenes and Nanoporous Carbon Materials for Energy, Environmental and Catalytic Applications

**APPOINTMENT OF SEVEN-MEMBERED EXAMINATION COMMITTEE:** 6/10/2021

<b>Dimitrios Gournis</b>	Professor of the Department of Materials Science and Engineering, School of Engineering, University of Ioannina
<b>Michael Karakassides</b>	Professor of the Department of Materials Science and Engineering, School of Engineering, University of Ioannina
<b>Georgios Romanos</b>	Research Director, Institute of Nanoscience and Nanotechnology, NCSR “Demokritos”
<b>Petra Rudolf</b>	Professor at the Zernike Institute for Advanced Materials, University of Groningen
<b>Alkiviadis Paipetis</b>	Professor of the Department of Materials Science and Engineering, School of Engineering, University of Ioannina
<b>Theodoros Steriotis</b>	Research Director, Institute of Nanoscience and Nanotechnology, NCSR “Demokritos”
<b>Pantelis Trikalitis</b>	Professor of the Department of Chemistry, School of Sciences and Engineering, University of Crete

Approval of doctoral thesis with grade ‘EXCELLENT’ on 3/12/2021

**The Head of the Department**



**Apostolos Avgeropoulos**  
Professor



**The Secretary of the Department**



**Maria Kontou**

## Περίληψη

Οι ανάγκες της σύγχρονης κοινωνίας για νέα υλικά, καινοτόμες εφαρμογές και τεχνολογίες αιχμής, αυξάνονται μέρα με τη μέρα, και η επιστημονική κοινότητα δείχνει να βρίσκεται σε ένα συνεχή αγώνα δρόμου για νέες ανακαλύψεις. Η αντικατάσταση των παραδοσιακών υλικών από νέα και πιο αποδοτικά υλικά κρίνεται πλέον επιτακτική, ιδιαίτερα όταν για την παραγωγή τους γίνεται χρήση που βρίσκονται σε έλλειψη. Επιπλέον, κάθε νέα προσέγγιση πρέπει να εναρμονίζεται με τις απαιτήσεις για ένα πιο πράσινο μέλλον, χωρίς απόβλητα, και χαμηλότερο ενεργειακό και υλικό αποτύπωμα.

Τα νανοπορώδη υλικά, των οποίων η εκμετάλλευση απαντάται ήδη από την αρχαιότητα, βρίσκουν εφαρμογή στην εποχή μας στα πεδία της κατάλυσης, της ενέργειας (αποθήκευση υδρογόνου, πυκνωτές, μπαταρίες ιόντων λιθίου, κελιά καυσίμων και αισθητήρες), την περιβαλλοντική αποκατάσταση (μοριακά κόσκινα/προσροφητικά, απομάκρυνση οξειδίων αζώτου και υδρόθειου), ακόμη και την ιατρική, χάρη στη δυνατότητα ελέγχου του μεγέθους των πόρων, της ποικιλόμορφης γεωμετρίας, των επιφανειακών ιδιοτήτων και της ικανότητάς τους να αλληλοεπιδρούν με μόρια και άτομα, ή να τα απορροφούν/απελευθερώνουν. Δεδομένου ότι ο άνθρακας συγκαταλέγεται μεταξύ των πλέον άφθονων στοιχείων στη γη, και μπορεί να βρεθεί σε πληθώρα μορφών, τα υλικά άνθρακα αποτελούν εξαιρετικές επιλογές για εφαρμογές που περιλαμβάνουν πορώδες.

Το πορώδες στα υλικά μπορεί να σχηματιστεί με πολλούς τρόπους: η παρούσα διδακτορική διατριβή εστιάζει στους πορώδεις άνθρακες που προκύπτουν από την ανθρακοποίηση, τη 'χημική χάραξη' (chemical etching), τη σύνθεση με χρήση προτύπου και την ενεργοποίηση, αλλά και υποστυλωμένες δομές που προσομοιάζουν αυτή του Παρθενώνα. Τα τελευταία κατασκευάστηκαν μέσω της παρεμβολής στιβαρών οργανικών ή/και ανόργανων πυλώνων μεταξύ φύλλων γραφενίου, ώστε να διαχωρίζονται τα στρώματα και να δημιουργούνται διασυνδεδεμένοι κενοί χώροι, συνδυάζοντας με τον τρόπο αυτό τις ιδιότητες του γραφενίου με το πορώδες.

Η διατριβή αυτή χωρίζεται σε δύο μέρη: το πρώτο που είναι αφιερωμένο στα υποστυλωμένα γραφένια (Κεφάλαια 3 & 4), και το δεύτερο μέρος (Κεφάλαια 5 & 6) που αναφέρεται σε υψηλού πορώδους δομές άνθρακα.

Στο Κεφάλαιο 3, παρουσιάζεται μία ταχεία συνθετική διαδικασία για τη δημιουργία ετεροδομών υψηλού πορώδους με προσαρμοσμένες ιδιότητες μέσω της πυριτίωσης οργανικά τροποποιημένου οξειδίου του γραφενίου. Τρεις ξεχωριστές οργανοπυριτικές πρόδρομες ενώσεις (1,4-δισ(τριαιθοξυσιλυλο)-βενζόλιο - BTB, τετρα(αιθοξείδιο) του πυριτίου - TEOS και 3-αμινοπροπυλο τριαιθοξείδιο του πυριτίου - APTEOS) με διαφορετικά δομικά χαρακτηριστικά χρησιμοποιήθηκαν ως δομικά στοιχεία για τη δημιουργία υποστυλωτών μεταξύ των στρωμάτων του οργανικά τροποποιημένου οξειδίου του γραφενίου. Η ιδέα ήταν να αναπτυχθούν υψηλής απόδοσης πυριτικά δίκτυα στον ενδοστρωματικό χώρο, μέσω αντιδράσεων sol-gel. Η θερμική αποσύνθεση επέτρεψε την απομάκρυνση των οργανικών μορίων δημιουργώντας έτσι πορώδεις ετεροδομές με πολύ υψηλή ειδική επιφάνεια και σπογγοειδή δομή, οι οποίες είναι πολύ ελκυστικές για πιθανή χρήση σε κατάλυση, προσρόφηση, αλλά και ως πληρωτικά υλικά σε νανοσύνθετα πολυμερή. Τα τελικά υλικά χαρακτηρίστηκαν πλήρως με έναν συνδυασμό τεχνικών (περίθλαση ακτίνων-X, φασματοσκοπίες μέσου υπερύθρου και φωτοηλεκτρονίων ακτίνων-X, θερμική ανάλυση, ηλεκτρονική μικροσκοπία σάρωσης και μετρήσεις ειδικής επιφάνειας) και αξιολογήθηκε ο βαθμός πυριτίωσης για κάθε αντιδραστήριο. Η γεφυρωμένη με φαινυλομάδες πορώδης ετεροδομή έδειξε την μεγαλύτερη περιεκτικότητα σε πυρίτιο στην τελική του δομή, και η επακόλουθη πυρόλυση έδειξε να δημιουργεί την επιθυμητή πορώδη δομή με μία ειδική

επιφάνεια που άγγιξε τα 550 m<sup>2</sup>/g. Για το συγκεκριμένο υβριδικό υλικό διερευνήθηκε εν συντομία η δυνατότητα προσρόφησης διοξειδίου του άνθρακα, και διαπιστώθηκε η υψηλή ικανότητα προσρόφησης του έως και 3.5 mmol/g στα 5 bar και 0 °C, τιμή η οποία το καθιστά πολλά υποσχόμενο για περαιτέρω εξέταση ως υλικό αποθήκευσης διοξειδίου του άνθρακα.

Το Κεφάλαιο 4 περιγράφει την ένθεση των ειδών υποστύλωσης ανάμεσα στις στρώσεις οξειδίου του γραφενίου με σκοπό τη δημιουργία ενός στιβαρού τρισδιάστατου δικτύου φύλλων γραφενίου. Τα οκταμερή ολιγοσιλοξάνια σχηματίστηκαν μέσω της υδρολυτικής πολυσυμπύκνωσης της N[-3-(τριμεθοξυσιλυλ)προπυλο]-αιθυλενοδιαμίνης (EDAPTEOS) και εντέθηκαν σε τρία διαφορετικά φορτία (1.5, 4.5 και 9 mmol). Τα σιλοξάνια πέραν της συνεισφοράς τους στη δημιουργία της νανοπορώδους δομής, καθιστούν τα υλικά ισχυρούς προσροφητές διοξειδίου του άνθρακα χάρη στις μη αντιδρώσες αμινομάδες τους που με την παρουσία τους στον ανοιχτό χώρο μεταξύ των φύλλων γραφενίου, εγγυόνται την δέσμευση του διοξειδίου του άνθρακα. Χρησιμοποιώντας ξήρανση σε αέρα αλλά και λυοφιλίωση, δύο διακριτές μορφολογίες επιτεύχθηκαν, οι οποίες επαληθεύτηκαν με τη χρήση μικροσκοπίας SEM. Η επιτυχής ένθεση επιβεβαιώθηκε με περίθλαση ακτίνων-X και φασματοσκοπία FT IR, το σχετικό ποσοστό οξειδίου του πυριτίου για κάθε φορτίο ορίστηκε με θερμική ανάλυση, και τα ατομικά ποσοστά των στοιχείων που υπάρχουν στα δείγματα, καθώς και μία εικόνα για το είδος των αλληλεπιδράσεων, αποκτήθηκαν μέσω της φασματοσκοπίας XPS. Τα πορώδη χαρακτηριστικά μελετήθηκαν με ποροσιμετρία αζώτου, και η δυνατότητα προσρόφησης διοξειδίου του άνθρακα για όλα τα δείγματα διερευνήθηκε μέσω της καταγραφής ισοθέρμων προσρόφησης στους 273 K και 298 K, μέχρι 1 bar. Καταφέραμε να δείξουμε ότι η λυοφιλίωση ενισχύει σημαντικά το πορώδες σε σχέση με την ξήρανση σε αέρα, και ότι η μορφολογία αυτή μπορεί να οδηγήσει σε ενισχυμένη ικανότητα προσρόφησης διοξειδίου του άνθρακα εάν επιλεγεί το βέλτιστο φορτίο παράγοντα υποστύλωσης.

Το Κεφάλαιο 5 επικεντρώνεται σε μια διαφορετική περιβαλλοντική πρόκληση, την απομάκρυνση του υδρόθειου. Με βάση την αποδεδειγμένη απόδοση των πορωδών μητρών σε διαδικασίες αποθείωσης όταν αυτές συνδυάζονται με οξειδία μετάλλων, η χρήση εμπλουτισμένου με χαλκό πορώδη κυβοειδή άνθρακα για δέσμευση υδρόθειου παρουσιάζεται για πρώτη φορά. Μέσω μιας αντίδρασης συντονισμού η οποία ακολουθήθηκε από ένα στάδιο πυρόλυσης, τρία διαφορετικά δείγματα παρασκευάστηκαν: μία δομή πλούσια σε χαλκό αλλά με χαμηλή ειδική επιφάνεια, μία μορφή άνθρακα με υψηλό πορώδες αλλά χωρίς προσθήκη μετάλλου, και τέλος την ίδια μορφή πορώδους άνθρακα αλλά αυτή τη φορά διακοσμημένης με χαλκό. Τα πορώδη χαρακτηριστικά των δειγμάτων μελετήθηκαν με ανάλυση προσρόφησης-εκρόφησης αζώτου, και η περιεκτικότητά τους σε μέταλλο προσδιορίστηκε με θερμική ανάλυση. Η φασματοσκοπία φωτοηλεκτρονίων ακτίνων-X έδωσε πληροφορίες για την στοιχειακή σύνθεση και το χημικό περιβάλλον των στοιχείων, ενώ η μορφολογία των νέων ροφητικών μέσων μελετήθηκε με μικροσκοπία SEM. Για να διερευνηθεί το πώς η υψηλή ειδική επιφάνεια και η παρουσία οξειδίου του χαλκού μπορούν να εξισοροποιηθούν, και το πώς επηρεάζουν συνεργατικά την απομάκρυνση του υδρόθειου, η απόδοση των πορωδών κυβοειδών ανθράκων αξιολογήθηκε με ένα πείραμα χημειορόφησης υδρόθειου στους 150 °C. Τα ροφητικά με το υψηλότερο πορώδες έδειξαν μικρότερη ικανότητα ρόφησης και ήταν παράλληλα καταλυτικά ενεργά. Το πλούσιο σε χαλκό αλλά με χαμηλή ειδική επιφάνεια δείγμα αποδείχτηκε ότι λειτουργεί επίσης ως καταλύτης, με επιλεκτική οξείδωση του υδρόθειου να λαμβάνει χώρα. Το δείγμα αυτό μελετήθηκε περαιτέρω και παρουσιάστηκαν ιδέες για τον πιθανό μηχανισμό που κρύβεται πίσω από την καταλυτική δραστηριότητα. Περαιτέρω βελτίωση των υλικών που σχεδιάστηκαν, θα μπορούσε να οδηγήσει σε καταλύτες υψηλής απόδοσης κατάλληλους για μετατροπή υδρόθειου.

Στοχεύοντας στην επαναχρησιμοποίηση αποβλήτων για την ανάπτυξη υψηλής απόδοσης ροφητικών υλικών, στο Κεφάλαιο 6 παρουσιάζεται για πρώτη φορά μία σειρά καινοτόμων



ιεραρχημένων πορωδών ανθράκων (πορώδεις άνθρακες που συνδυάζουν και τα τρία είδη πορώδους) οι οποίοι συντέθηκαν με την ενσωμάτωση αποβλήτων ζάχαρης και καφέ. Τέσσερα είδη πορώδους άνθρακα αναπτύχθηκαν συνολικά: ένα που χρησιμοποιεί λύματα μελάσας σε συνδυασμό με διοξείδιο του πυριτίου ως σύνθετο αρχικό υλικό, ένα που χρησιμοποιεί απόβλητα εκχυλισμάτων ριζών ζαχαρότευτλων και διοξείδιο του πυριτίου, ένα τρίτο, όπου χρησιμοποιημένοι κόκκοι καφέ χρησίμευσαν ως ενίσχυση σε μια προσπάθεια εισαγωγής λειτουργικών ομάδων που θα μπορούσαν να είναι επωφελείς για μελλοντικές εφαρμογές, και ένα τελευταίο όπου δύο είδη αποβλήτων (μελάσα και χρησιμοποιημένοι κόκκοι καφέ) συνδυάστηκαν. Οι ιδιότητες και τα επιφανειακά χαρακτηριστικά όλων των παραγόμενων ιεραρχημένων πορωδών ανθράκων μελετήθηκαν με ποροσιμετρία αζώτου και ηλεκτρονική μικροσκοπία σάρωσης. Επιτεύχθηκαν ειδικές επιφάνειες στο εύρος των 260-1009 m<sup>2</sup>/g. Τρία από τα δείγματα υποβλήθηκαν σε φυσική ενεργοποίηση με διοξείδιο του άνθρακα, που είχε ως αποτέλεσμα τη μεγιστοποίηση της ειδικής επιφάνειας έως και κατά 127 % μετά την εισαγωγή μικροπορώδους. Όλα τα δείγματα παρουσιάζουν μεγάλες δυνατότητες και θα μπορούσαν να είναι ιδανικοί υποψήφιοι για εφαρμογές προσρόφησης και πυκνωτών, καθώς και αποκατάστασης λιμασμένων υδάτων.



## Summary

The demands of modern society for new materials, novel applications and cutting-edge technologies are increasing day by day, and the scientific community seems to be involved in a never-ending race for new breakthroughs. Time weighs in on the emergent need for replacement of traditional materials by new and more efficient ones, especially when nearly depleted sources are involved in their production. Furthermore, any new approach has to conform with the demands for a greener, waste-free, and less energy- and resource-demanding future.

Nanoporous materials have been exploited since antiquity, and are nowadays applied in the fields of catalysis, energy (hydrogen storage, supercapacitors, Li-ion batteries, fuel cells and sensors), environmental remediation (molecular sieves/adsorbents, NO<sub>x</sub> and H<sub>2</sub>S removal, CO<sub>2</sub> capture), and even medicine because of their controllable pore size, diverse geometries, surface properties and their ability to interact with molecules and atoms or adsorb/release them. Since carbon is amongst the most abundant elements on earth, and can be found in a plethora of forms, carbon materials are excellent candidates for applications that involve porosity.

Porosity in materials can be obtained in many ways; in this PhD project the focus lays on porous carbons resulting from carbonization, chemical etching, template synthesis and activation, or 'Parthenon like' structures. The latter were constructed through the intercalation of robust organic and/or inorganic pillars between graphene sheets in order to keep the layers apart and create interconnected void spaces, combining in this way the properties of graphene with porosity.

This thesis is divided in two parts; the first half is devoted to pillared graphenes (Chapters 3 & 4), and the second part (Chapters 5 & 6) is dedicated to highly porous carbon structures.

In Chapter 3, a rapid synthetic procedure to create highly porous heterostructures with tailored properties through the silylation of organically modified graphene oxide is presented. Three distinct silica precursors (1,4-bis(triethoxysilyl)-benzene - BTB, tetraethylorthosilicate – TEOS and (3-aminopropyl)triethoxysilane - APTEOS) with different structural characteristics were used as building blocks for pillars between organo-modified graphene oxide layers. The idea was to develop high yield silica networks within the interlayer space through sol-gel reactions. Thermal decomposition enabled the removal of the organic molecules thereby generating porous heterostructures with very high surface area and sponge-like make-up, which are very attractive for potential use in catalysis, sorption and as fillers in polymer nanocomposites. The final products were fully characterized with a combination of techniques (X-ray diffraction, Fourier transform infrared and X-ray photoelectron spectroscopies, thermogravimetric analysis, scanning electron microscopy and porosity measurements) and the degree of silylation of each reagent was evaluated. The porous heterostructure bridged with a phenyl group showed the maximum amount of silica content in the final heterostructure and subsequent pyrolysis was found to create the desired porous structure with a specific surface area up to 550 m<sup>2</sup>/g. For this hybrid the potential as sorbent of CO<sub>2</sub> was briefly explored and a high CO<sub>2</sub> adsorption capacity of 3.5 mmol/g at 5 bar and 0 °C was found, which is promising for further consideration as CO<sub>2</sub> storage material.

Chapter 4 describes the intercalation of pillaring species between graphene oxide (GO) layers to create a robust 3-D network of graphene sheets. Octameric oligosiloxanes were formed through the hydrolytic polycondensation of N-[3-(trimethoxysilyl)propyl]-ethylenediamine (EDAPTEOS) and intercalated in three different loadings (1.5, 4.5 and 9 mmol). Silsesquioxanes, apart from helping to create a nanoporous structure, render the materials strong CO<sub>2</sub> adsorbents due to the unreacted amine groups emanating in the open space between the GO sheets, which warrant CO<sub>2</sub>

binding. Air-drying and freeze-drying were used to achieve distinct morphologies, verified by SEM microscopy. The successful intercalation was confirmed by X-ray diffraction and FT-IR spectroscopy, the relative amount of silicon oxide for each loading was defined by thermogravimetric analysis, the atomic percentages of the elements present in the samples as well as an insight on the type of interactions were gained through X-ray photoelectron spectroscopy. The pore characteristics were studied by nitrogen porosimetry, and the CO<sub>2</sub> adsorption behaviour for all samples was investigated by recording the corresponding adsorption isotherms at 273 K and 298 K, up to 1 bar. We could show that freeze-drying significantly enhances the porosity as compared to air-drying and this morphology can lead to an enhanced CO<sub>2</sub> adsorption capacity if an optimal loading of the pillaring agent is chosen.

Chapter 5 focalises on a different environmental challenge, namely hydrogen sulfide removal. Based on the proven desulfurization performance of porous matrixes when combined with metal oxides, the use of copper enriched porous carbon cuboids in H<sub>2</sub>S capture is reported for the first time. Through a coordination reaction followed by a pyrolysis step, three different samples were prepared; a low-surface-area copper-rich structure, a highly porous carbon form without metal addition, and finally the same porous carbon decorated with copper. The pore characteristics of the samples were investigated by nitrogen adsorption-desorption analysis, and their metal content was determined by thermogravimetric analysis. X-ray photoelectron spectroscopy gave insight in the elemental composition and the chemical environment of the elements, while the morphology of the novel sorbents was studied with scanning electron microscopy. To explore how the high surface area and the presence of copper oxide can be balanced and how they synergistically affect hydrogen sulphide removal, the performance of the porous carbon cuboids was evaluated with a H<sub>2</sub>S chemisorption experiment at 150 °C. The sorbents with the higher porosity showed lower sorption capacity and were also catalytically active. The copper-rich sample with the lowest surface area was proved to function also as a catalyst, with selective oxidation of hydrogen sulphide taking place. This copper-rich sample was investigated a bit further and the chapter reports on ideas about the potential mechanism behind the catalytic activity put forward. Further improvement of the designed materials could lead in high performance catalysts suitable for H<sub>2</sub>S conversion.

Aiming at waste reuse for the development of high-performance sorbents, in Chapter 6, a set of novel hierarchical porous carbons (carbons that combine all three kinds of porosity), which were synthesized by incorporating sugar waste and spent coffee grounds, is presented for the first time. Four kinds of porous carbons were developed in total: one using molasses wastewater in combination with silica as a composite starting material; another one using sugar beet root extract waste and silica; a third one where spent coffee grounds served as reinforcement in an attempt to introduce functional groups that could be beneficial for future applications; and a last one where two kinds of waste (molasses and spent coffee grounds) were combined. The properties and surface characteristics of all the produced hierarchical porous carbons were studied with N<sub>2</sub> porosimetry and scanning electron microscopy. Specific surface areas in the range of 260-1009 m<sup>2</sup>/g were achieved. Three of the samples were subjected to physical activation with CO<sub>2</sub>, that resulted in maximization of the specific area up to 127 % after the introduction of microporosity. All the synthesized samples show a great potential and could be ideal candidates for sorption, water remediation and supercapacitor applications.





## Table of Contents

Chapter 1: Introduction .....	1
1.1. Porous materials .....	1
1.2. Carbon .....	2
1.2.1. Graphene .....	2
1.2.2. Graphene oxide .....	3
1.2.2.1. Graphene Pillaring.....	3
1.2.2.2. Silsesquioxanes as pillaring agents .....	4
1.2.3. Porous Carbons .....	4
1.2.3.1. Hierarchical Porous Carbons.....	5
1.2.3.2. Porous Carbon Cuboids.....	5
1.3. Applications .....	6
1.3.1. Energy .....	6
1.3.2. Environmental remediation .....	6
1.3.3. Catalytic Applications .....	6
1.4. Thesis Outline .....	6
References .....	8
Chapter 2: Characterization techniques.....	11
2.1. X-Ray Diffraction .....	12
2.2. Fourier Transform Infrared Spectroscopy .....	12
2.3. Surface Area and Porosity Measurements .....	13
2.4. X-Ray Photoelectron Spectroscopy .....	17
2.5. Thermal Analysis .....	18
2.6. Scanning Electron Microscopy .....	19
2.7. CO <sub>2</sub> adsorption measurements.....	20
2.8. Anion exchange chromatography.....	21
References .....	22
Chapter 3: New Porous Heterostructures Based on Organo-Modified Graphene Oxide for CO <sub>2</sub> capture .....	23

3.1. Introduction.....	24
3.2. Experimental Section.....	26
3.2.1. Materials.....	26
3.2.2. Graphene Oxide Synthesis.....	26
3.2.3. Organo-Modified Graphene Oxide.....	27
3.2.4. Silica-GO Heterostructures.....	27
3.3. Results and Discussion.....	28
3.4. Conclusions.....	41
References.....	43
Chapter 4: A diamino-functionalized silsesquioxane pillared graphene oxide for CO <sub>2</sub> capture.....	47
4.1. Introduction.....	48
4.2. Experimental Section.....	50
4.2.1. Materials.....	50
4.2.2. Graphene Oxide Synthesis.....	50
4.2.3. Formation of the pillaring agent.....	51
4.2.4. Preparation of silsesquioxane pillared graphene oxide.....	51
4.3. Results and Discussion.....	52
4.4. Conclusions.....	66
References.....	67
Chapter 5: H <sub>2</sub> S removal by copper enriched and porous carbon cuboids.....	71
5.1. Introduction.....	72
5.2. Materials and methods.....	73
5.2.1. Materials.....	73
5.2.2. Materials synthesis.....	74
5.2.2.1. PCC synthesis.....	74
5.2.2.2. PCC-Cu synthesis.....	74
5.2.3. H <sub>2</sub> S adsorption experiments.....	74
5.3. Results and discussion.....	76



5.3.1. Structural and morphological characterization of the sorbents	76
5.3.2. H <sub>2</sub> S removal study	85
5.3.3. Possible reactions – proposed mechanism	91
5.4. Conclusions	93
References	94
Chapter 6: Hierarchical porous carbon structures derived from sugar and coffee waste	97
6.1. Introduction	98
6.2. Materials and methods	100
6.2.1. Materials	100
6.2.2. Materials synthesis	100
6.2.3. CO <sub>2</sub> activation	102
6.3. Results and Discussion	103
6.4. Conclusions	116
References	117
Summary	121
Samenvatting	125
Περίληψη	129
Acknowledgements	133
List of publications	141
The author	143



# Chapter 1: Introduction

“Porous materials are like music: the gaps are as important as the filled-in bits.”<sup>1</sup>

The technological evolution has led to breakthroughs that could never have been imagined a couple of decades ago, and at the same time has set the scientific community on a constant search for novel materials with extraordinary properties that will be able to keep up with the ever-increasing demands for efficient solutions. Among them, nanoporous materials, which have been used since ancient times, have been attracting a lot of attention throughout the last past years due to their controllable pore size, diverse geometries, surface properties and their ability to interact with molecules and atoms or adsorb them, that can be easily exploited in various fields such as catalysis, gas storage, environmental remediation, sensorics, and medical applications.

## 1.1. Porous materials

As suggested by the International Union of Pure and Applied Chemistry (IUPAC), porous materials can be categorized according to the width of their pores in three big categories: microporous ( $< 2$  nm), mesoporous ( $2 \text{ nm} < w < 50 \text{ nm}$ ) and macroporous ( $> 50 \text{ nm}$ ).<sup>2</sup> This classification though, is not sufficient if someone bears in mind the rest of criteria by which one can differentiate porous materials such as the pore structure and shape (cylindrical, spherical, hexagonal and slit types). High surface area ( $\text{m}^2/\text{g}$ ), controlled pore diameter, thermal stability and catalytic properties make porous materials outstanding candidates for gas adsorption, energy storage and heterogenous catalysis applications. The most known porous solids are:

- ❖ zeolites; microporous crystalline silicate frameworks that occur naturally;
- ❖ metal organic frameworks (MOFs); porous crystalline materials formed by metal clusters/ions linked with organic ligands;
- ❖ clays; naturally occurring aluminium phyllosilicates;
- ❖ silica nanoparticles; inorganic high pore volume nanometer sized structures, and

- ❖ carbonaceous porous sorbents (among which activated carbons); materials that are made up solely of carbon.

## 1.2. Carbon

Carbon is present everywhere around us. In the things we touch, the things we eat, the ones we breathe. It is a dominant element of our lives, and it is not surprising that carbon research has been the focus of thousands of researchers within the global scientific community, with major accomplishments like two Nobel prizes in Chemistry and Physics within 15 years. The first one was awarded to Harry Kroto in 1996 for the discovery of the ‘buckminsterfullerene’, a spherical hollow carbon structure made of 60 carbon atoms arranged in hexagons and pentagons.<sup>3</sup> A couple of years later it was the turn of Andre Geim and Konstantin Novoselov to get recognition in 2010 "for ground-breaking experiments regarding the two-dimensional material graphene" for which they isolated a single flake of graphene using simple scotch tape.<sup>4</sup>

Carbon can be encountered in a variety of forms due to its ability to form structures with diverse properties depending on the way its atoms are covalently bonded between them in diverse hybridization states ( $sp$ ,  $sp^2$ ,  $sp^3$  and mixtures of the latter).<sup>5</sup> Till the 80's, graphite and diamond were the only carbon allotropes known but over the following years a lot of new members were added to the carbon family, namely in addition to the already mentioned fullerenes and graphene, carbon dots,<sup>6</sup> single and multi-wall carbon nanotubes (SWCNTs and MWCNTs),<sup>7, 8</sup> nanodiamonds<sup>9</sup> and graphene nanoribbons<sup>10</sup>. Apart from C-C bonds, carbon can be covalently connected with other elements in a strong and stable manner as well, allowing the formation of an almost infinite number of compounds.

### 1.2.1. Graphene

Graphene is a two-dimensional (2D) sheet made of  $sp^2$  bonded carbon atoms (Figure 1.1), each of which is connected to three neighbouring ones creating this way a strong honeycomb lattice. Chemical vapour deposition (CVD) on liquid or crystalline copper, micromechanical exfoliation and liquid-phase exfoliation of graphite are the most common ways of producing high quality graphene.<sup>11, 12</sup>

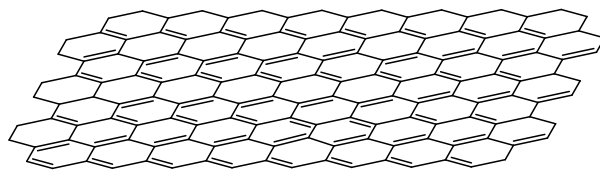


**Figure 1.1.** Structural representation of graphene

Its outstanding properties include a very high carrier mobility,<sup>13</sup> extraordinary thermal conductivity,<sup>14</sup> high surface area (theoretically 2630 m<sup>2</sup>/g),<sup>15</sup> mechanical stiffness,<sup>16</sup> impermeability,<sup>17</sup> flexibility<sup>18</sup> and transparency,<sup>19</sup> which render it a perfect candidate for industrial applications in sectors like transport, (bio)medicine, electronics, photonics, energy, or desalination.<sup>20-23</sup>

### 1.2.2. Graphene oxide

Starting from graphite and choosing one of the oxidation methods developed long before graphene became fashionable by Brodie,<sup>24</sup> Staudenmaier,<sup>25</sup> and Hummers<sup>26</sup> or their more recent variations, oxygen containing functional groups (epoxy, methoxy, carboxyl) are introduced on the basal planes and edges of the carbon nanosheets (Figure 1.2). The resulting layered structure is hydrophilic and soluble in many solvents.<sup>27</sup> The presence of these groups allows for reactions (ring-opening reactions, noncovalent functionalization, cycloaddition, *etc.*)<sup>28</sup> and grafting of moieties (molecules, long chain hydrocarbons, polymers)<sup>29,30</sup> that (partially) occupy the interlayer space.

#### 1.2.2.1. Graphene Pillaring

Graphene and graphene oxide's lack of permanent porosity can be overcome through pillaring. Once a moiety has been intercalated between the layers, stability can be gained through a thermal process, which enables the preservation of the layered structure and hence of the porosity (an example of silsesquioxane pillared graphene oxide is shown in Figure 1.2). Experiments with different pillaring agents and extensive theoretical modeling,<sup>31, 32</sup> have proven that with the insertion of a suitable and robust organic and/or inorganic species between the layers, demanding technological targets in gas storage or sensing can be easily reached. Apart from graphene and graphene oxide, the pillaring method can and has already been applied to other materials such as zeolites, clays and layered double hydroxides.

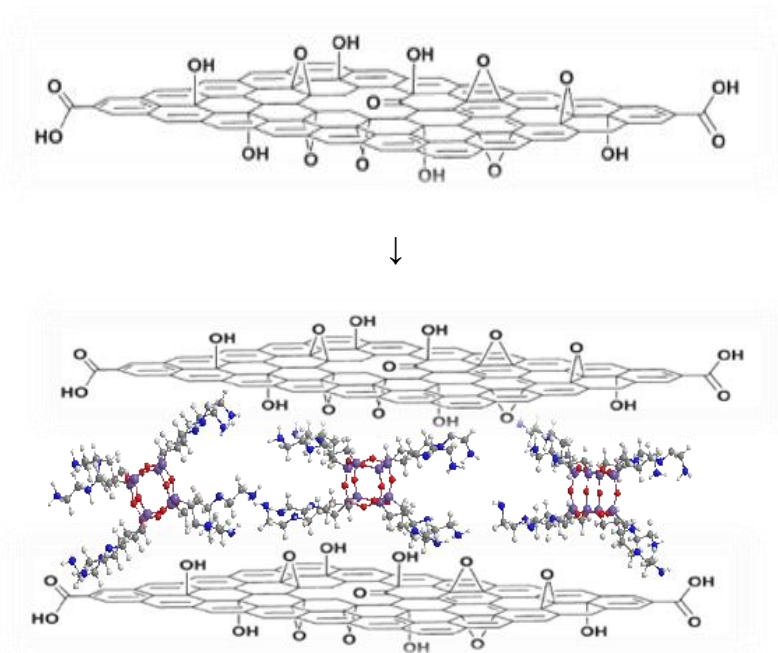


**Figure 1.2.** Structural representation of graphene oxide (up) and silsesquioxane pillared graphene oxide (down)

### 1.2.2.2. Silsesquioxanes as pillaring agents

Polyhedral silsesquioxanes (POSS) are cage-like organosilicon compounds with the chemical formula  $[XSiO_{1.5}]_n$  (where X = H, alkyl, aryl or alkoxy) that derive from the hydrolytic condensation of organosilicon monomers.<sup>33</sup> They can act as pillaring agents creating a robust three-dimensional network by attaching to the graphene oxide sheets and be exploited in this way in a variety of applications ranging from hydrogen storage<sup>34</sup> to removal of water pollutants<sup>35</sup>.

### 1.2.3. Porous Carbons

Nanoporous carbons is an important category of porous materials that combine micro and mesoporosity in their structure and have been at the centre of scientific attention for a while due to their high specific area, electrical conductivity, and chemical inertness.

### 1.2.3.1. Hierarchical Porous Carbons

Hierarchical Porous Carbons (HPCs) denotes a carbon structure that possesses a labyrinthian porous network of well-defined macropores and interconnected micro- and mesopores, which provide better accessibility and a large amount of active sites distributed all over the bulk and not only the surfaces.<sup>36</sup> HPCs are usually synthesized by employing a soft or hard template method or a combination of both, which is moreover coupled with an activation process ( $\text{CO}_2$ ,  $\text{KOH}$ , *etc.*)<sup>37-39</sup> that can induce microporosity as explained further in Chapter 6. Templating methods involve the use of suitable scaffolds that are being later removed during the synthetic procedure, leaving behind pores. Depending on the size and form of the template, the porous structure can have tailored characteristics. Thermally decaying polymers, micelles and emulsions are usually used as soft templates and simply decompose during carbonization, whereas inorganic solids (silica particles or gel,  $\text{Na}_2\text{CO}_3$ ,  $\text{MgO}$ ,  $\text{CaCO}_3$ , *etc.*) are used as hard templates, which need to be removed by chemical etching.<sup>36, 40-42</sup>

### 1.2.3.2. Porous Carbon Cuboids

In 2014, Stefan Kaskel and co-workers<sup>43</sup> came up with a new form of ultra-hydrophilic porous carbon with cuboid shape, which is decorated with uniformly distributed N and O heteroatoms (Figure 1.3). The functional groups, in combination with the relatively high specific surface area (800-900  $\text{m}^2/\text{g}$ ), abundance of narrow micropores, low weight and great stability, render carbon cuboids very promising candidates for adsorption/molecular sieving in the gas industry.

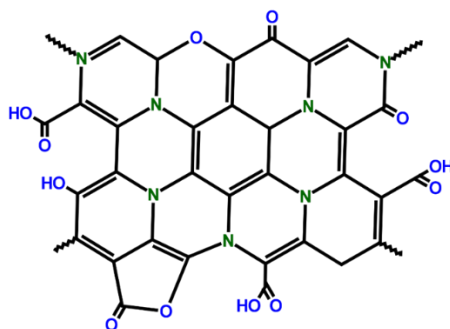


**Figure 1.3.** Structural representation of porous carbon cuboids

### **1.3. Applications**

All the forementioned categories of materials have been receiving increasing attention recently due to their potential use in a plethora of applications that can meet the demands of our modern ultra-consuming world. These applications are for the most part localized in the fields of energy, environmental remediation, and catalysis.

#### **1.3.1. Energy**

Energy storage and conversion are two of the biggest challenges of our era due to the rising demands and the changes necessary to avoid even more global warming. Porous materials are being developed and studied in order to be used in hydrogen storage applications,<sup>44</sup> as supercapacitors,<sup>45</sup> in Li-ion batteries,<sup>46</sup> fuel cells and sensors<sup>47</sup>.

#### **1.3.2. Environmental remediation**

With most limits of emissions being exceeded by far, a lot of effort is being made towards the development of technologies that can minimize or at least control the damage being caused to the environment by removing or separating pollutants from gas and waste streams, as well as from contaminated water. All these problems can find solutions through the development of materials that can serve as molecular sieves/adsorbents,<sup>47-49</sup> in NO<sub>x</sub> and H<sub>2</sub>S removal,<sup>50, 51</sup> and in assisted oil recovery among others.

#### **1.3.3. Catalytic Applications**

Porous carbons are promising candidates for the substitution of traditional catalysts and its already being studied extensively their use as catalysts or as supports for metal nanoparticles or for metal complex anchoring.<sup>47, 48, 52-54</sup>

### **1.4. Thesis Outline**

This thesis is a representative sample of the research efforts during my PhD journey towards the development of porous carbon materials with tailored properties that can be applied in energy storage, environmental remediation, and catalysis. The property that has constantly been under the spotlight all along these four years was porosity. In order to achieve high porosity materials my attempts were divided along two pathways; the



construction of ‘Parthenon like’ structures inserting columns between the sheets of layered carbon materials like graphene oxide in an attempt to create interconnected empty spaces, and the development of porous carbons cuboids and hierarchical porous carbon structures that serve as tiny waste recyclers.

As briefly described in the following paragraphs, the research conducted during this PhD project is organized in six chapters in this dissertation.

Chapter 2 explains all the characterization techniques that were employed during the preparation and characterization of the developed materials, as well as the methods used in order to determine their potential use in future applications.

Chapter 3 describes the synthesis of highly porous heterostructures with tailored properties through the creation of a silica network in the interlayer space of organically modified graphene oxide. Three distinct silica precursors were used as building blocks and the potential as sorbent of CO<sub>2</sub> was briefly explored for the heterostructure with the highest specific surface area.

Chapter 4 is devoted to our exploration of the use of silsesquioxane-pillared graphene oxide for CO<sub>2</sub> capture, where we demonstrated that modifying the silsesquioxane loading and drying method causes important variations in the adsorption capacity.

Chapter 5 gives an overview of the ability of copper-enriched porous carbon cuboids to capture H<sub>2</sub>S gas. The properties of the sorbents were explored and their hybrid behaviour acting both as adsorbents and catalysts was investigated.

Finally, in Chapter 6 a set of hierarchical porous carbons that were developed making use of sugar and coffee wastes is presented. High specific surface areas and pore volumes were achieved, and it was shown that both can be maximized by subjecting the samples to physical activation with CO<sub>2</sub>.

## References

1. G. Q. Lu and X. S. Zhao, in *Nanoporous Materials: Science and Engineering*, World Scientific Publishing Co. Ltd, Singapore, 2004.
2. K. S. W. Sing, D. H. Everett, R. A. W. Haul, L. Moscou, R. A. Pierotti, J. Rouquerol and T. Siemieniewska, *Pure and Applied Chemistry*, 1985, **57**, 603-619.
3. H. W. Kroto, J. R. Heath, S. C. O'Brien, R. F. Curl and R. E. Smalley, *Nature*, 1985, **318**, 162-163.
4. K. S. Novoselov, A. K. Geim, S. V. Morozov, D. Jiang, Y. Zhang, S. V. Dubonos, I. V. Grigorieva and A. A. Firsov, *Science*, 2004, **306**, 666-669.
5. V. Georgakilas, J. A. Perman, J. Tucek and R. Zboril, *Chemical Reviews*, 2015, **115**, 4744-4822.
6. X. Xu, R. Ray, Y. Gu, H. J. Ploehn, L. Gearheart, K. Raker and W. A. Scrivens, *Journal of the American Chemical Society*, 2004, **126**, 12736-12737.
7. S. Iijima, *Nature*, 1991, **354**, 56-58.
8. S. Iijima and T. Ichihashi, *Nature*, 1993, **363**, 603-605.
9. V. V. Danilenko, *Physics of the Solid State*, 2004, **46**, 595-599.
10. D. V. Kosynkin, A. L. Higginbotham, A. Sinitskii, J. R. Lomeda, A. Dimiev, B. K. Price and J. M. Tour, *Nature*, 2009, **458**, 872-876.
11. Y. Zhu, S. Murali, W. Cai, X. Li, J. W. Suk, J. R. Potts and R. S. Ruoff, *Advanced Materials*, 2010, **22**, 3906-3924.
12. S. Park and R. S. Ruoff, *Nature Nanotechnology*, 2009, **4**, 217-224.
13. Y. Zhang, Y. W. Tan, H. L. Stormer and P. Kim, *Nature*, 2005, **438**, 201-204.
14. A. A. Balandin, S. Ghosh, W. Bao, I. Calizo, D. Teweldebrhan, F. Miao and C. N. Lau, *Nano Letters*, 2008, **8**, 902-907.
15. A. Peigney, C. Laurent, E. Flahaut, R. R. Bacsa and A. Rousset, *Carbon*, 2001, **39**, 507-514.
16. C. Lee, X. Wei, J. W. Kysar and J. Hone, *Science*, 2008, **321**, 385-388.
17. V. Berry, *Carbon*, 2013, **62**, 1-10.
18. S. Bae, H. Kim, Y. Lee, X. Xu, J.-S. Park, Y. Zheng, J. Balakrishnan, T. Lei, H. Ri Kim, Y. I. Song, Y.-J. Kim, K. S. Kim, B. Ozyilmaz, J.-H. Ahn, B. H. Hong and S. Iijima, *Nature Nanotechnology*, 2010, **5**, 574-578.

19. R. R. Nair, P. Blake, A. N. Grigorenko, K. S. Novoselov, T. J. Booth, T. Stauber, N. M. R. Peres and A. K. Geim, *Science*, 2008, **320**, 1308.
20. K. S. Novoselov, V. I. Fal'ko, L. Colombo, P. R. Gellert, M. G. Schwab and K. Kim, *Nature*, 2012, **490**, 192-200.
21. E. P. Randviir, D. A. C. Brownson and C. E. Banks, *Materials Today*, 2014, **17**, 426-432.
22. J. Yang, P. Hu and G. Yu, *APL Materials*, 2019, **7**, 020901.
23. The University of Manchester, Graphene - Applications, <https://www.graphene.manchester.ac.uk/learn/applications/> retrieved on August 10<sup>th</sup> 2021.
24. B. C. Brodie, *Ann. Chim. Phys.*, 1860, **59**, 466.
25. L. Staudenmaier, *Berichte der deutschen chemischen Gesellschaft*, 1898, **31**, 1481-1487.
26. W. S. Hummers Jr and R. E. Offeman, *Journal of the American Chemical Society*, 1958, **80**, 1339.
27. J. I. Paredes, S. Villar-Rodil, A. Martínez-Alonso and J. M. D. Tascón, *Langmuir*, 2008, **24**, 10560-10564.
28. I. V. Pavlidis, M. Patila, U. T. Bornscheuer, D. Gournis and H. Stamatis, *Trends in Biotechnology*, 2014, **32**, 312-320.
29. K. Spyrou, G. Potsi, E. K. Diamanti, X. Ke, E. Serestatidou, I. I. Verginadis, A. P. Velalopoulou, A. M. Evangelou, Y. Deligiannakis, G. Van Tendeloo, D. Gournis and P. Rudolf, *Advanced Functional Materials*, 2014, **24**, 5841-5850.
30. K. Spyrou, L. Kang, E. K. Diamanti, R. Y. Gengler, D. Gournis, M. Prato and P. Rudolf, *Carbon*, 2013, **61**, 313-320.
31. G. K. Dimitrakakis, E. Tylisanakis and G. E. Froudakis, *Nano Letters*, 2008, **8**, 3166-3170.
32. K. Duan, L. Li, Y. Hu and X. Wang, *Scientific Reports*, 2017, **7**, 14012.
33. L. y. V. I. Voronkov M.G., *Polyhedral oligosilsesquioxanes and their homo derivatives*, Springer, Berlin, Heidelberg, 1982.
34. Y. Matsuo, S. Ueda, K. Konishi, J. P. Marco-Lozar, D. Lozano-Castelló and D. Cazorla-Amorós, *International Journal of Hydrogen Energy*, 2012, **37**, 10702-10708.
35. C. E. Flores-Chaparro, C. J. Castilho, I. Külaots, R. H. Hurt and J. R. Rangel-Mendez, *Journal of Environmental Management*, 2020, **259**, 110044.
36. R. Fu, Z. Li, Y. Liang, F. Li, F. Xu and D. Wu, *New Carbon Materials*, 2011, **26**, 171-179.

37. J. Wang and S. Kaskel, *Journal of Materials Chemistry*, 2012, **22**, 23710-23725.
38. M. C. Mittelmeijer-Hazeleger and J. M. Martín-Martínez, *Carbon*, 1992, **30**, 695-709.
39. A. Ahmadpour and D. D. Do, *Carbon*, 1996, **34**, 471-479.
40. Z. Zhang, Z. P. Cano, D. Luo, H. Dou, A. Yu and Z. Chen, *Journal of Materials Chemistry A*, 2019, **7**, 20985-21003.
41. W. Zhang, R.-r. Cheng, H.-h. Bi, Y.-h. Lu, L.-b. Ma and X.-j. He, *New Carbon Materials*, 2021, **36**, 69-81.
42. A.-H. Lu, G.-P. Hao, Q. Sun, X.-Q. Zhang and W.-C. Li, *Macromolecular Chemistry and Physics*, 2012, **213**, 1107-1131.
43. G.-P. Hao, G. Mondin, Z. Zheng, T. Biemelt, S. Klosz, R. Schubel, A. Eychmüller and S. Kaskel, *Angewandte Chemie International Edition*, 2015, **54**, 1941-1945.
44. D. Giasafaki, G. Charalambopoulou, C. Tampaxis, K. Dimos, D. Gournis, A. Stubos and T. Steriotis, *Carbon*, 2016, **98**, 1-14.
45. L. Estevez, R. Dua, N. Bhandari, A. Ramanujapuram, P. Wang and E. P. Giannelis, *Energy & Environmental Science*, 2013, **6**, 1785-1790.
46. R. Sahore, L. P. Estevez, A. Ramanujapuram, F. J. DiSalvo and E. P. Giannelis, *Journal of Power Sources*, 2015, **297**, 188-194.
47. A. Stein, Z. Wang and M. A. Fierke, *Advanced Materials*, 2009, **21**, 265-293.
48. F. Rodríguez-Reinoso and A. Sepúlveda-Escribano, in *Handbook of Surfaces and Interfaces of Materials*, ed. H. S. Nalwa, Academic Press, Burlington, 2001, pp. 309-355.
49. L. Estevez, D. Barpaga, J. Zheng, S. Sabale, R. L. Patel, J.-G. Zhang, B. P. McGrail and R. K. Motkuri, *Industrial & Engineering Chemistry Research*, 2018, **57**, 1262-1268.
50. A. G. Georgiadis, N. D. Charisiou and M. A. Goula, *Catalysts*, 2020, **10**, 521.
51. E. García-Bordejé, A. Monzón, M. J. Lázaro and R. Moliner, *Catalysis Today*, 2005, **102-103**, 177-182.
52. J. L. Figueiredo, *Journal of Materials Chemistry A*, 2013, **1**, 9351-9364.
53. H. Liu, X. Liu, S. Mu, S. Wang, S. Wang, L. Li and E. P. Giannelis, *Catalysis Science & Technology*, 2017, **7**, 1965-1970.
54. I. Matos, M. Bernardo and I. Fonseca, *Catalysis Today*, 2017, **285**, 194-203.

## Chapter 2: Characterization techniques

*This chapter describes the key experimental methods used to characterize the porous carbon materials presented in this dissertation. If a specific measurement was not performed by the candidate, this is specified herein as well.*

## 2.1. X-Ray Diffraction

X-ray diffraction (XRD) is a non-destructive analysis method based on the X-Ray photons scattering from a crystalline sample; it provides information about the crystalline phases and structure, interlayer distance and the size of the coherently diffracting domains. The XRD pattern is unique for each crystalline compound hence collecting diffraction data enables the identification of an unknown compound or phase.

The powder X-ray diffraction (XRD) patterns of the pillared graphene oxide described in Chapter 3 and of the carbon cuboid samples labelled PCC and PCC-Cu in Chapter 5, were collected on a D8 Advance Bruker diffractometer with a Cu  $K\alpha$  X-ray source (wavelength 1.5418 Å) and a secondary beam graphite monochromator. The patterns were recorded in a  $2\theta$  range from 2 to 40°, in steps of 0.02° and with a counting time of 2.00 s per step. The measurements were performed by Dr. Christina Papachristodoulou (University of Ioannina, Greece).

The diffraction spectra of the silsesquioxane-pillared graphene oxide samples described in Chapters 4 and of the carbon cuboid sample labelled PCC-unleached described in Chapter 5 were collected on a D8 Advance Bruker diffractometer with a monochromatic Cu  $K\alpha$  X-ray source (wavelength 1.5418 Å); a 1 mm divergent slit and a 3 mm antiscattering slit were used. The  $2\theta$  scans were performed from 2 to 80° with a step size of 0.02° and a counting time of 1.00 s per step.

The XRD measurements that were recorded before and after the H<sub>2</sub>S adsorption measurements reported in Chapter 5, were performed on a Panalytical X'Pert PRO powder diffractometer. About 30 mg of the selected sample was first placed on a zero-background holder and the measurements were conducted using Cu- $K\alpha$  radiation ( $\lambda = 1.5406$  Å). The diffraction patterns were collected over the  $2\theta$  range of 10° to 80° with a step size of 0.02° and the time per step of 1.3 s. The measurements were performed by Dr. Georgia Basina (Khalifa University, United Arab Emirates).

## 2.2. Fourier Transform Infrared Spectroscopy

Infrared Spectroscopy is a widely used tool in chemistry for qualitative and quantitative identification of substances. When an infrared beam passes

through the sample, part of the radiation is absorbed, and part transmitted. Each compound absorbs, reflects, and transmits IR radiation at different frequencies resulting in a unique signal, which represents the molecular ‘fingerprint’ of the sample. The vibrational characteristics of the molecules are used for the identification of functional groups and bonds present in the structure.

Fourier transform infrared (FTIR) spectra reported in Chapters 3 and 4 were measured in the range 400–4000  $\text{cm}^{-1}$  with a Shimadzu FT-IR 8400 spectrometer equipped with a deuterated triglycine sulfate (DTGS) detector. Each spectrum was the average of 64 scans collected at 2  $\text{cm}^{-1}$  resolution. Samples were in the form of KBr pellets containing ca. 2 wt% sample.

### **2.3. Surface Area and Porosity Measurements**

The morphological characteristics of porous solids and fine powders can be studied by means of gas adsorption measurements. An inert gas (usually nitrogen) is physisorbed at low temperature and the quantity of adsorbate on the material’s surface is measured over a wide range of relative pressures resulting in an adsorption isotherm. The physisorption isotherms can be grouped in 8 categories after the updated classification recommended by the International Union of Pure and Applied Chemistry (IUPAC) in 2015 (Figure 2.1).<sup>1</sup>

Each category is indicative of the type of porosity of the adsorbent: I(a): ultramicropores, I(b): supermicropores, II & III: non porous heterogeneous planar surfaces, IV(a): large mesopores, IV(b): narrow mesopores, V: mesopores and micropores, and VI: non porous homogeneous surfaces.<sup>1</sup>

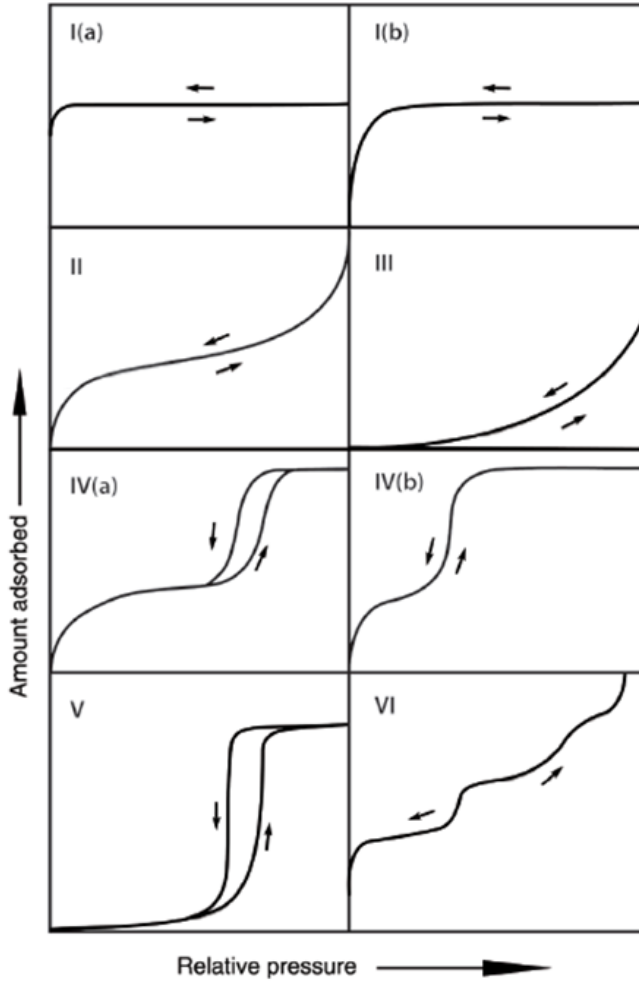


**Figure 2.1.** Classification of physisorption isotherms<sup>1</sup>

Information can be extracted about the geometrical structure of the pores from the shape of the hysteresis loop formed on the adsorption-desorption isotherms; this hysteresis loop is associated with capillary condensation. The main types of hysteresis loops are summarized in Figure 2.2.



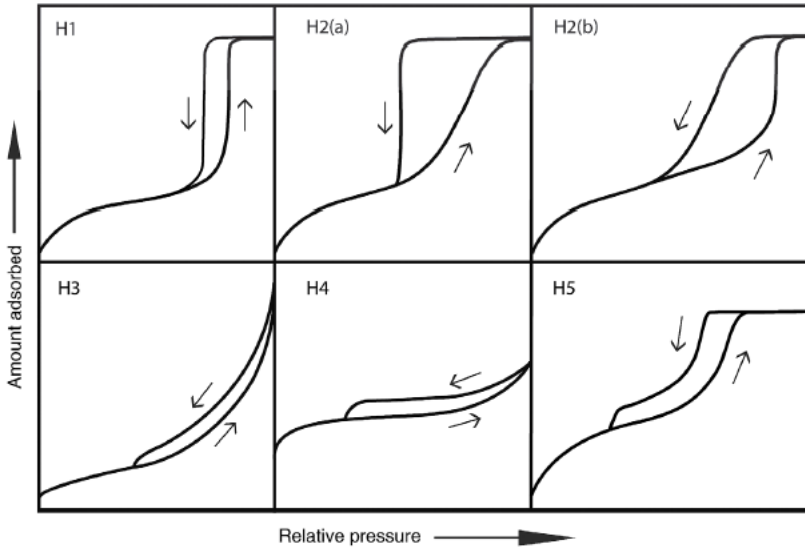


**Figure 2.2.** Classification of hysteresis loops<sup>1</sup>

Each type of loop is related with specific pore structures. In summary, H1 is observed for cylindrical pores, loops H2(a) & H2(b) for the so-called ‘ink bottle’ pores, which consist of a larger volume connected by a narrow neck to the next pore; H3 results for a disordered pore structure, usually aggregates of lamellar particles or networks consisting of not fully filled macropores; H4 is found if both micro- and mesopores are present, and H5 when there are open as well as restricted pores.<sup>1</sup>

The specific surface area, pore volume and pore size distribution can be extracted from the adsorption measurements. The most widely used procedure for evaluating the specific surface area is the Brunauer-Emmett-Teller (BET) method<sup>2</sup>, which is an extension of the Langmuir theory for monolayer formation, and makes use of the following equation:

$$\frac{p}{V(p^0 - p)} = \frac{1}{V_m C} + \frac{C - 1}{V_m C} \left(\frac{p}{p^0}\right)$$

where  $V$  is the volume adsorbed,  $V_m$  is the volume of a monolayer,  $p$  the equilibrium pressure,  $p^0$  the saturation pressure and  $C$  is a constant related to the enthalpy of adsorption in the first adsorbed layer (BET constant).

The nitrogen adsorption-desorption isotherms for the pillared graphene oxide described in Chapter 3 and the porous carbon cuboids presented in Chapter 5, were measured at 77 K on a Sorptomatic 1990 Thermo Finnigan porosimeter. Specific surface area values were determined by the Brunauer–Emmett–Teller (BET) method. The measurements reported in Chapter 5 were performed by Dr. Vasilis Kostas (University of Ioannina, Greece).

Low-pressure nitrogen sorption measurements for the silsesquioxane-pillared graphene oxide samples of Chapter 4 were carried out using an Autosorb 1-MP instrument from Quantachrome equipped with multiple pressure transducers for highly accurate analyses and an oil-free vacuum system. Ultra-high purity N<sub>2</sub> gas (99.999 %) was used for the adsorption measurements. Prior to the measurement, each sample was transferred to a 9 mm quartz cell and activated under dynamic vacuum at 100 °C for 20 h (until the output rate was less than 2 mTorr/min) to remove all volatile species. After activation, the sample was weighed to obtain the precise mass of the solids and the cell was transferred to the analysis port of the gas sorption instrument. The measurements were performed by Dr. Giasemi K. Angeli (University of Crete, Greece).

The nitrogen adsorption-desorption isotherms for all the hierarchical porous carbon samples described in Chapter 6 were recorded on a Micromeritics ASAP2420 apparatus at 77 K before processing to the activation step. The specific surface area was evaluated with the BET method. The samples were degassed under reduced pressure at 120 °C for 15 h prior to the measurements.

The nitrogen adsorption-desorption isotherms for the carbon cuboid sample labelled PCC-unleached of Chapter 5, and the activated hierarchical porous carbon samples of Chapter 6, were recorded at 77 K on a Autosorb iQ gas sorption system from Quantachrome Instruments. The samples were degassed under high vacuum for respectively 10 h at 100 °C (PCC-unleached) and 120 °C (activated hierarchical porous carbon) before performing the measurements. The measurements were performed by Dr. Konstantinos Spyrou (University of Ioannina, Greece) and the analysis by myself.

## 2.4. X-Ray Photoelectron Spectroscopy

Based on the photoelectric effect, X-ray photoelectron spectroscopy (XPS) is a surface-sensitive quantitative spectroscopic technique that is applied to acquire useful information about the surface elemental composition (up to a depth of ~10 nm), as well as the chemical environment and electronic state of each element present.<sup>3</sup> The material is irradiated with an X-ray beam and the kinetic energy and number of the electrons emitted are analysed in order to acquire the spectra.

XPS analysis in Chapters 3, 4 and 5 was performed using a Surface Science SSX-100 ESCA instrument with a monochromatic Al K $\alpha$  X-ray source ( $h\nu = 1486.6$  eV). The pressure in the measurement chamber was maintained at  $1 \times 10^{-9}$  mbar during data acquisition. The electron take-off angle with respect to the surface normal was  $37^\circ$ . The XPS data were acquired by using a spot size of  $1000 \mu\text{m}$  in diameter and the energy resolution was 1.3 eV for both the survey spectra and the detailed spectra of the core level regions. All XPS spectra were analysed using the least-squares curve-fitting program Winspec (developed at LISE laboratory of the University of Namur, Belgium). Deconvolution of the spectra included a Shirley baseline<sup>4</sup> subtraction and fitting with a minimum number of peaks consistent with the chemical structure of the sample, taking into account the experimental resolution. The profile of the peaks was taken as a convolution of Gaussian and Lorentzian functions. All binding energies derived from deconvolution are reported  $\pm 0.1$  eV. For the spectra reported in Chapter 3 the binding energies are referenced to the C1s photoemission peak centred at a binding energy of 284.8 eV.<sup>5</sup> The uncertainty in the peak intensity determination is 2 % for all core levels reported. For the analysis I was helped by Dr. Oreste de Luca (University of Groningen, the Netherlands). For the spectra of the silsesquioxane-pillared graphene oxide samples shown in Chapter 4 the Au4f<sub>7/2</sub> core level was used as a reference binding energy.<sup>5</sup> For the measurements, evaporated polycrystalline 150 nm thick gold films supported on mica (grade V-1, TED PELLA), prepared by sublimation of 99.99% gold (Schöne Edelmetaal B.V.) as detailed in Mendoza *et al.*<sup>6</sup> were used as substrates where freshly prepared samples were drop casted. All the data were normalized to the number of scans and corrected for the sensitivity factor of the spectrometer. The analysis was performed by Dr. Konstantinos Spyrou (University of Ioannina, Greece).

XPS measurements on the porous carbon cuboids detailed in Chapter 5 were performed under ultrahigh vacuum conditions with a base pressure of  $5 \times 10^{-10}$  mbar in a SPECS GmbH instrument equipped with a monochromatic Mg K $\alpha$  source ( $h\nu = 1253.6$  eV) and a Phoibos-100 hemispherical analyser. Samples were suspended in water, drop casted on Si wafers, and after they were dry, they were left in high vacuum overnight to outgas, before being transferred to the main chamber for XPS measurement. The energy resolution was set to 1.18 eV, and the photoelectron take-off angle was  $45^\circ$  with respect to the surface normal. Recorded spectra were the average of three scans with the energy step set to 0.05 eV and a dwell time of 1 s. All binding energies were referenced to the C1s core level at 285.0 eV. Spectral analysis included a Shirley background subtraction and peak deconvolution employing mixed Gaussian–Lorentzian functions in a least-squares curve-fitting program WinSpec. The analysis was performed by Dr. Konstantinos Spyrou (University of Ioannina, Greece).

## 2.5. Thermal Analysis

Thermal analysis techniques reveal the phase transitions of a sample, which are almost always accompanied by a mass loss, as a function of temperature. They can provide qualitative and quantitative information regarding the thermal stability, decomposition, as well as the exothermic and endothermic character of the phase transitions taking place.

Thermogravimetric (TGA) and differential thermal (DTA) analyses for Chapters 3 and 5 were performed using a Perkin Elmer Pyris Diamond TG/DTA. Samples of approximately 5 mg were heated in air from 25 to 850 °C, at a rate of 5 °C/min.

Thermogravimetric analysis (TGA) for Chapters 4 and 5 was performed with a TA-Instruments Discovery TGA 5500. Samples of approximately 5 mg were heated in air from 25 °C to 850 °C, at a rate of 5 °C/min. The measurements were performed by Jur van Dijken (University of Groningen, the Netherlands).

## 2.6. Scanning Electron Microscopy

Scanning electron microscopy (SEM) is a method for obtaining detailed imaging of the morphology of a surface at high magnification. A finely focused beam of electrons is used to probe the surface of the solid sample and the backscattered and secondary electrons are detected. Asperities on the surface modulate the intensity of the signal being emitted from the scanned area and the intensity variations recorded while scanning over the surface are used to construct the image. Since the impinging electrons can also interact inelastically and the excited atoms decay emitting X-rays typical of the specific element, most SEM setups are equipped with X-ray detectors, which allow elemental analysis and mapping, in addition to revealing the surface morphology. All samples analysed by SEM must be conductive to avoid charge build-up; insulating samples are coated with a thin metallic film before analysis.

The SEM micrographs of the graphene based heterostructures described in Chapter 3 were collected using a JEOL JSM-7401F field emission scanning electron microscope (FE-SEM). A low acceleration voltage was applied (~2 kV), and the working distance was set to 3 mm. A powder sample was mounted onto the round brass substrate using double-coated conductive carbon tape. The measurements were performed by Lamprini G. Boutsika (National Centre for Scientific Research “Demokritos”, Greece).

SEM analyses on the silsesquioxane-pillared graphene oxide samples described in Chapter 4 were carried out using a JEOL JSM-6390LV microscope equipped with an Oxford Instruments detector for energy dispersive X-ray spectroscopy (EDS). The measurements were performed by Konstantinos G. Froudas (University of Crete, Greece).

SEM images of the porous carbon cuboids depicted in Chapter 5 were recorded using a JEOL instrument (JSM-6510LV with a LaB<sub>6</sub> filament) equipped with an EDS detector (Oxford Instruments, x-act) operating at an accelerating voltage of 20 kV and using high vacuum ( $10^{-5}$  bar). All samples were in the form of a powder; they were placed on a double-sided carbon tape to be stabilized and were measured without coating.

The SEM images of the carbon cuboid samples labelled PCC-unleached, before and after the H<sub>2</sub>S adsorption measurements reported in Chapter 5,

were obtained on a Quanta 250 FEG-FEI microscope, using a Schottky field emission gun as the electron source, with a spatial resolution of ~1 nm at 5-10 kV. Elemental analysis and phase mapping were also conducted using this microscope, equipped with an Apollo silicon drift detector, integrated with the EDAX Genesis software. The measurements were performed by Dr. Georgia Basina (Khalifa University, United Arab Emirates).

The SEM images of PCC-unleached reported in Chapter 5, were recorded using a Zeiss Gemini 500 Scanning Electron Microscope at the Cornell Centre for Materials Research. The measurements were performed in Dr. Emmanuel P. Giannelis group (Cornell University, United States of America).

The SEM measurements on the hierarchical porous carbons described in Chapter 6, were performed with a FEI Philips FEG-XL30s microscope by Dr. Liqiang Lu (University of Groningen, the Netherlands).

## **2.7. CO<sub>2</sub> adsorption measurements**

The evaluation of the graphene-based materials synthesized in Chapters 3 and 4 as carbon dioxide sorbents was performed by monitoring their ability of capturing CO<sub>2</sub>.

CO<sub>2</sub> adsorption isotherms at 0, 10 and 20 °C reported in Chapter 3 were measured on an Intelligent Gravimetric Analyser (IGA–Hiden Ltd.). Before exposure to CO<sub>2</sub> the samples were outgassed overnight in 250 °C under high vacuum (10<sup>-8</sup> mbar) until the mass was observed to remain constant. The measurements were performed by Dr. Andreas Sapalidis (National Centre for Scientific Research “Demokritos”, Greece).

Low-pressure carbon dioxide sorption measurements on the silsesquioxane-pillared graphene oxide samples described in Chapter 4 were carried out using an Autosorb 1-MP instrument from Quantachrome equipped with multiple pressure transducers for highly accurate analyses and an oil-free vacuum system. Ultra-high purity CO<sub>2</sub> gas (99.999%) was used for the adsorption measurements. Prior to the measurement, each sample was transferred to a 9 mm quartz cell and activated under dynamic vacuum at 100 °C for 20 h (until the output rate was less than 2 mTorr/min) to remove all volatile species. After activation, the sample was weighed to

obtain the precise mass of the solids and the cell was transferred to the analysis port of the gas sorption instrument. The measurements were performed by Dr. Giasemi K. Angeli (University of Crete, Greece).

## **2.8. Anion exchange chromatography**

To determine the sugar (monomer) composition in the biomass derived samples of Chapter 6, High-performance anion exchange chromatography (HPAEC) was performed on a Dionex Ultimate 6000 system (Thermo Scientific, Sunnyvale, CA, USA) equipped with a CarboPac PA-1 column (2 mm x 250 mm ID) in combination with a CarboPac PA-1 guard column (2 mm x 50 mm ID) and PAD detection. The system was controlled using Chromeleon 7.2.9 software (Thermo Scientific, Sunnyvale, CA, USA). The samples were freeze dried and milled (powder) prior to the analysis. The dry samples were dissolved in MilliQ water (concentrated liquid sugar beet root wastewater: 9.2 mg/mL, and molasses: 38 mg/mL), centrifuged and diluted 6-40x and injected on the Dionex HPAEC system on the Oligomer method, which is described as follows. Elution of oligomers (0.3 mL min<sup>-1</sup>) was performed with a multi-step-gradient using the following eluents: A: 0.1M NaOH and B: 1M NaOAc in 0.1M NaOH. After 12 min equilibration with 100 % A a linear gradient over 35 min up to 38 % B was performed, followed by 8 min wash with 100 % B. Quantification was performed based on the pure fructose/sucrose and glucose standards. The measurements were performed by Dr. Edita Jurak (University of Groningen, the Netherlands).

## References

1. M. Thommes, K. Kaneko, A. V. Neimark, J. P. Olivier, F. Rodriguez-Reinoso, J. Rouquerol and K. S. W. Sing, *Pure and Applied Chemistry*, 2015, **87**, 1051-1069.
2. S. Brunauer, P. H. Emmett and E. Teller, *Journal of the American Chemical Society*, 1938, **60**, 309-319.
3. D. Briggs and M. P. Seah, *Practical Surface Analysis - Auger and X-ray Photoelectron Spectroscopy*, John Wiley, Chichester, U.K., 1990.
4. D. A. Shirley, *Physical Review B*, 1972, **5**, 4709-4714.
5. J. F. Moulder, W. F. Stickle and P. E. Sobol, *Handbook of X-ray photoelectron spectroscopy : a reference book of standard spectra for identification and interpretation of XPS data*, Physical Electronics, Inc., Eden Prairie, Minn., 1995.
6. S. M. Mendoza, Doctoral Thesis, University of Groningen, 2007.



## Chapter 3: New Porous Heterostructures Based on Organo-Modified Graphene Oxide for CO<sub>2</sub> capture

A facile and rapid synthetic procedure to create highly porous heterostructures with tailored properties through the silylation of organically modified graphene oxide is reported in this chapter. Three silica precursors with various structural characteristics (comprising alkyl or phenyl groups) were employed to create high-yield silica networks as pillars between the organo-modified graphene oxide layers. The removal of organic molecules through the thermal decomposition generates porous heterostructures with very high surface areas ( $\geq 500 \text{ m}^2/\text{g}$ ), which are very attractive for potential use in diverse applications such as catalysis, absorption and as fillers in polymer nanocomposites. The final hybrid products were characterized by X-ray diffraction, Fourier transform infrared and X-ray photoelectron spectroscopies, thermogravimetric analysis, scanning electron microscopy and porosity measurements. As proof of principle, the porous heterostructure with the maximum surface area was chosen for investigating its CO<sub>2</sub> adsorption properties.

---

*Published as:*

*New Porous Heterostructures Based on Organo-Modified Graphene Oxide for CO<sub>2</sub> Capture, Eleni Thomou, Evmorfia K. Diamanti, Apostolos Enotiadis, Konstantinos Spyrou, Efstratia Mitsari, Lamprini G. Boutsika, Andreas Sapalidis, Estela Moretón Alfonsín, Oreste De Luca, Dimitrios Gournis and Petra Rudolf, Frontiers in Chemistry, Vol. 8, Article 564838, 2020*

### 3.1. Introduction

The dramatic effects of global warming (sea level rise, wildfires, flooding, extreme weather conditions) and the constant degradation of our planet are among the most important and challenging issues the modern world is facing. Approximately 35 billion metric tons of CO<sub>2</sub> are emitted globally each year<sup>1</sup> and with the already existing technology only an insignificant fraction of these emissions is currently prevented from contributing to the greenhouse gas effect. Instead of being considered a detrimental waste product, carbon dioxide can become a precious and perfectly sustainable source material, which, once captured, can be utilized in a plethora of commercial processes such as enhanced oil recovery, chemical or biological conversion, food industry, mineral carbonation *etc.*<sup>1</sup> Therefore the development of low cost, efficient, easily applied, reusable and environmentally friendly materials capable of capturing and storing greenhouse gases, and more specifically CO<sub>2</sub>, which constitutes a major factor in global warming, is more urgent than ever before.

Adsorption that involves binding of carbon dioxide onto the surface of a solid sorbent, is one of the most promising CO<sub>2</sub> separation technologies that are currently being developed and used.<sup>2</sup> A wide range of sorbents has been proposed, from activated carbon, to zeolites, alumina, or MOFs—just to name a few<sup>3</sup> and among the materials that have been studied for this purpose is also graphene oxide<sup>4-7</sup>. Graphene-based materials hold a prominent position as they combine a series of significant advances such as excellent physicochemical properties, high specific surface areas, low adsorption energy, high selectivity and light weight<sup>8</sup>. Graphene oxide (GO), a layered structure produced by the treatment of graphite with strong oxidizing agents and characterized by a high concentration of diverse oxygen containing functional groups, which make it hydrophilic, has been identified as an excellent host matrix for diverse functional molecular structures. Organic molecules, inorganic pillars or metal ions can be accommodated in its interlayer space to design porous hybrid materials for energy<sup>9</sup>, environmental<sup>10</sup> and sorption<sup>11</sup> applications. An essential step for realizing such nanostructures was the modification/intercalation of graphene oxide with primary aliphatic chains in order to create an organophilic GO derivative that can be readily dispersed in polar organic solvents<sup>12</sup>.

Large specific surface area and high selectivity are two of the most important characteristics a material should have in order to be considered a suitable candidate for CO<sub>2</sub> adsorption applications.<sup>2</sup> Saha and Kienbaum showed that higher selectivity for CO<sub>2</sub> over other gases can be achieved by introducing selected functionalities and heteroatoms (nitrogen, oxygen, sulfur) to the sorbent's surface.<sup>13</sup> However, it is quite challenging to meet the high specific surface area criteria when employing GO for the development of sorbents since the big disadvantage of layered materials like GO is their lack of permanent porosity: a normal layered material can for example swell upon hydration, but collapses again after dehydration. Hence, in order to overcome this obstacle, taking advantage of intercalation chemistry, permanent pillars have to be introduced between the layers in order to create a robust 3-D network of adjacent graphene sheets with nanopores of the right size and surface properties to accommodate CO<sub>2</sub>.

Pillaring of 2-D layered materials allows for a fine control of the structural characteristics of the resulting micro- and nanoporous composites<sup>14</sup> and assures structural stability, permanent pore sizes and high surface areas. Such rational interlayer design has opened new prospects for applications in areas as diverse as the nanocomposites themselves<sup>15-17</sup>, namely catalysis<sup>18, 19</sup>, metal uptake<sup>20</sup>, sensors<sup>21</sup>, environmental remediation<sup>22</sup>, supercapacitors<sup>23-25</sup> and lithium-ion batteries<sup>26</sup>.

In cases where an improved structural stability was crucial, graphene oxide sheets were kept apart via the creation of metal oxide networks in the interlayer space.<sup>27</sup> Many studies have been published regarding the pillaring of graphene-based materials based on the incorporation of different silicon sources mainly by the sol-gel method. Organosilanes are silicon sources that have already been used successfully for the synthesis of periodic mesoporous organosilicas (PMOs) in the form of thin films<sup>28, 29</sup> and fibers<sup>30</sup>, as well as materials with other morphologies depending on the choice of precursor and the experimental conditions<sup>31-33</sup>. Matsuo's group has studied extensively the synthetic conditions for pillared GO with various silylating reagents such as 3-amino-propylethoxysilanes or alkyl trichlorosilane with various alkyl lengths.<sup>34, 35</sup> A pyrolysis step is required for these hybrids to obtain large surface areas and controlled pore sizes, both essential characteristics to extend their use to applications in the fields of hydrogen storage<sup>36</sup>, catalysts<sup>37, 38</sup>, electrodes<sup>39</sup> and sensors<sup>10</sup>.

Matsuo *et al.* have shown that the BET surface area of porous graphene heterostructures can be increased up to 756 m<sup>2</sup>/g after insertion of two different organosilanes between graphene layers in a two-step process.<sup>40</sup> The same group also showed that repeating silylation process of graphene oxide with trichlorosilane affects the density of the siliceous pillars, and allows to tailor the BET surface area between 77 and 723 m<sup>2</sup>/g.<sup>41</sup>

In the work described in this chapter, a new effective and efficient silylation process is proposed for the development of high surface area materials, which is considerably faster than the ones reported in the literature so far<sup>37, 40</sup>. The silylation was performed on an organically modified GO derivative employing three distinct silica precursors with different structural characteristics and chosen to develop silica networks within the interlayer space of the organo-modified GO. The final products were fully characterized with a combination of techniques and the degree of silylation of each reagent was evaluated. The one bridged with a phenyl group showed the maximum amount of silica content in the final heterostructure. Subsequent pyrolysis was found to create the desired porous structure raising the samples' specific surface area up to 550 m<sup>2</sup>/g. For this hybrid the potential as sorbent of CO<sub>2</sub> was briefly explored.

## 3.2. Experimental Section

### 3.2.1. Materials

Graphite (purum, powder ≤ 0.2mm), Nitric acid (65 % HNO<sub>3</sub>) and Potassium chlorate (KClO<sub>3</sub>, 98+ %) were purchased from Fluka Inc. Dodecylamine (DA, ≥ 99 %), 1,4-bis(triethoxysilyl)-benzene (BTB 99 %), tetraethylorthosilicate (TEOS 98+ %) and (3-aminopropyl)triethoxysilane (APTEOS ≥ 98 %) were acquired from Sigma-Aldrich, and sulfuric acid (H<sub>2</sub>SO<sub>4</sub>, 95–97 %), n-butanol and sodium hydroxide (NaOH) were obtained from Merck. All reagents were of analytical grade and used without further purification. Distilled deionized water was used for all the experiments.

### 3.2.2. Graphene Oxide Synthesis

Graphene oxide, denoted as GO in the following, was synthesized using a modified Staudenmaier's method<sup>42-44</sup>. In a typical synthesis, 10 g of powdered graphite was added to a mixture of 400 mL of 95–97 % H<sub>2</sub>SO<sub>4</sub>

and 200 mL of 65 %  $\text{HNO}_3$ , while cooling in an ice–water bath in order to counteract the heat released during the very exothermic chemical reaction. 200 g of powdered  $\text{KClO}_3$  was added to the mixture in small portions under continuous stirring and cooling. The reaction was quenched after 18 h by pouring the mixture into distilled water and the oxidation product was washed until the pH reached an almost neutral value ( $\sim 6.0$ ), and finally air-dried at room temperature after being spread on a glass plate.

### 3.2.3. Organo-Modified Graphene Oxide

1.5 g of dodecylamine were dissolved in 50 mL of ethanol and the solution was added slowly to an aqueous GO suspension (beforehand 0.1M NaOH was added to adjust the pH value to  $\sim 7.5$ ) under vigorous stirring (dodecylamine/GO 3:1 w/w). The mixture was stirred for 24 h, centrifuged, washed three times with ethanol/water: 1/1, and air-dried after being spread on a glass plate. The organo-modified GO is denoted as org-GO.

### 3.2.4. Silica-GO Heterostructures

Before silylation, GO was dried a second time under vacuum at room temperature overnight. 100 mg of org-GO were dispersed in n-butanol (5 mL), sonicated for 30 min and left under stirring overnight. The silica precursor (APTEOS, BTB or TEOS; chemical structures shown in Figure 3.1) was slowly added to the org-GO dispersion under stirring for 2 h before adding the water (containing a drop of hydrochloric acid) while keeping constant the molar ratio silica precursor/ $\text{H}_2\text{O}$ /n-butanol: 1/4/54. The sol-gel reactions were performed at 50 °C while stirring, and the obtained gel was placed in the oven at 50 °C overnight. The silica–GO organo-heterostructures are denoted as GO-BTB, GO-APTEOS and GO-TEOS, depending on which of the three organosilica precursors was employed. The final porous structures were collected after calcination in air at 370 °C for 120 min. The calcinated samples are denoted as G-BTB, G-APTEOS, and G-TEOS.

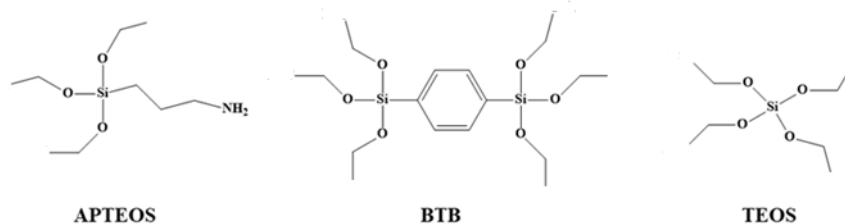


**Figure 3.1.** Chemical structures of the silica precursors used (APTEOS, BTB and TEOS)

### 3.3. Results and Discussion

The XRD patterns of the parent materials and of the final hybrids after the sol-gel modification are shown in Figure 3.2.

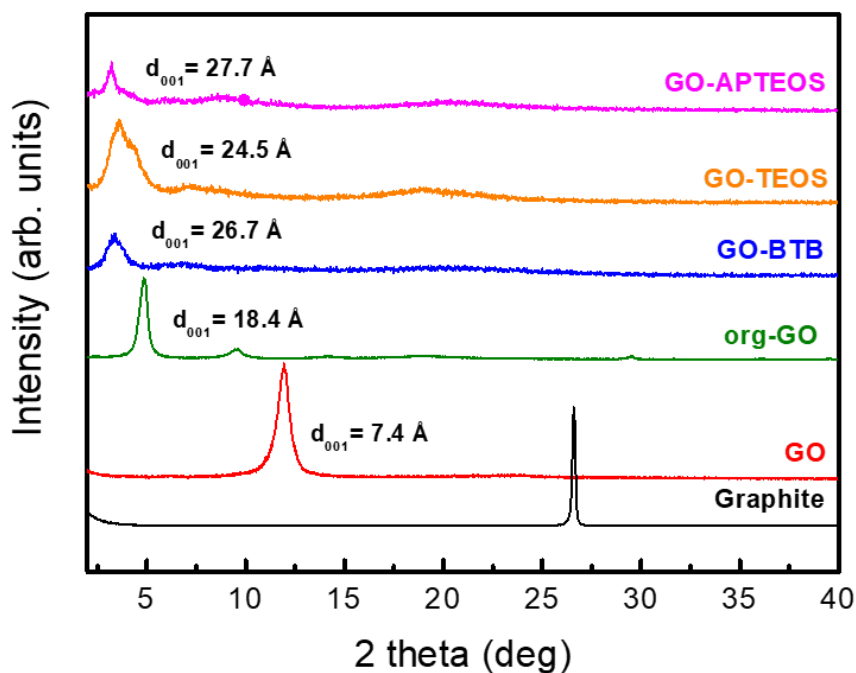


**Figure 3.2.** XRD patterns of pristine graphite, graphene oxide, organo-modified GO (org-GO), and heterostructures prepared by silylation with the three different organosilane precursors: BTB, TEOS, and APTEOS (GO-BTB, GO-TEOS, GO-APTEOS)

The XRD pattern of pristine graphite shows the characteristic peak corresponding to the 002 reflection of graphite at  $26.6^\circ$ , which translates into a basal spacing of  $3.3 \text{ \AA}$ . This peak disappeared after the oxidation process, when the 001 reflection peak is found at  $12.0^\circ$ , corresponding to a basal spacing of  $7.3 \text{ \AA}$ , characteristic of layered GO<sup>9</sup>. In fact, due to its hydrophilicity, GO exhibits one-dimensional swelling and can exhibit basal spacings between  $6.1$  and  $11 \text{ \AA}$ , depending on the amount of water adsorbed<sup>45</sup>.

After exposure of GO to dodecylamine the 001 reflection moved to even lower angles, attesting to an increase of the  $d_{001}$  spacing of GO and hence to the successful insertion of the guest molecules in the interlayer galleries. More specifically, the basal spacing,  $d_{001}$ , of the org-GO shifts to  $18.4 \text{ \AA}$  corresponding to an interlayer separation of  $\Delta = 18.4 - 6.1 = 12.3 \text{ \AA}$ , where  $6.1 \text{ \AA}$  is the thickness of the GO monolayer<sup>45</sup>. Through the organo-modification, the interlayer space of the GO becomes more accessible and readily modifiable with the silica precursors.

After the sol-gel reaction with silica alkoxides, the 001 reflection of the final hybrid materials is shifted to lower angles than for org-GO, confirming the successful expansion of the interlayer space and suggesting the formation of a silica network for each precursor. When org-GO was treated with the TEOS (GO-TEOS), the  $d$  spacing was calculated to amount to  $\sim 24.5 \text{ \AA}$  and even larger  $d$  values ( $26$ – $27 \text{ \AA}$ ) were achieved for APTEOS and BTB. The diffraction peak in this case is broader as a result of a distribution of different conformations. These larger values may be attributed to steric effects from the amino-terminated alkyl chains or phenylene ring anchored/bridged by silane centres of APTEOS and BTB, respectively.

Figure 3.3 displays the XRD patterns of the silica-GO heterostructures obtained after calcination of GO-BTB, GO-TEOS and GO-APTEOS at  $370^\circ\text{C}$ . For all hybrid heterostructures, the 001 reflection at lower angles ( $2$ – $10^\circ$ ) is not clearly identifiable but very broad features are observed. This indicates that the graphene layers have lost their ability to stack and proves that the silica-GO heterostructures are in an exfoliated form upon heating<sup>46</sup>.

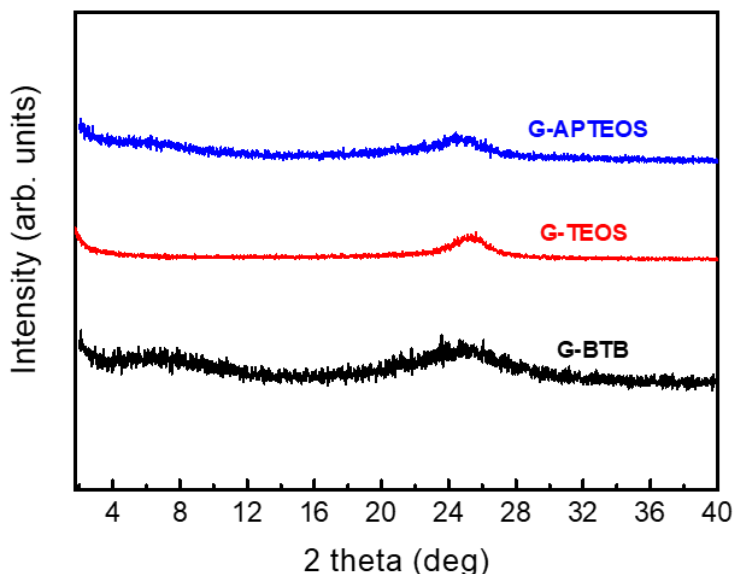


**Figure 3.3.** XRD patterns of the heterostructures obtained after calcination of GO-APTEOS, GO-TEOS and GO-BTB at 370 °C to yield G-APTEOS, G-TEOS and G-BTB.

FTIR and XPS spectroscopies can provide additional information on the elemental composition and the type of chemical bonds present in the final hybrid heterostructures. Figure 3.4 compares the FTIR spectra of GO-BTB before and after (G-BTB) the calcination treatment with those of graphite, pristine graphene oxide (GO) and organo-modified graphene oxide (org-GO). Compared to that of GO, the spectrum of org-GO shows two additional bands at 2847 and 2919  $\text{cm}^{-1}$  associated with the asymmetric and symmetric stretching vibrations of  $\text{CH}_2$  groups as well as a band at 1450  $\text{cm}^{-1}$  due to the vibrations of the N-H bond of the amino group. These spectral signatures clearly serve as evidence for the presence of dodecylamine in org-GO and thereby testify to the success of the organo-modification. The spectra of the heterostructure obtained by reaction with the silica precursor BTB exhibit a set of new peaks before (GO-BTB) and after calcination (G-BTB), which can be attributed to vibrations of the silicate matrix: the peaks at 520, 1065 and 1151  $\text{cm}^{-1}$  are due to Si-O-Si vibrations, while the ones at 690 and 950  $\text{cm}^{-1}$  are assigned to the vibrations of O-Si-O. Similar spectral signatures were also found for the



other heterostructures (GO-APTEOS, GO-TEOS, and G-APTEOS, G-TEOS, see Figure 3.5) confirming the presence of silica networks in all three heterostructures before and after calcination. For the BTB precursor, two new peaks at  $1396$  and  $3059\text{ cm}^{-1}$  corresponding to the vibrations of the double bond  $\text{C}=\text{C}$  and  $\text{C}-\text{H}$  of the phenyl rings appear in the GO-BTB spectrum. The characteristic bands of the intercalated dodecylamine identified in the spectrum of org-GO ( $2847$ ,  $2919$  and  $1483\text{ cm}^{-1}$ ) are absent from the spectrum of G-BTB, pointing to the successful removal of the surfactant molecules and hence give a first hint that a porous heterostructure consisting of silica and reduced graphene oxide building blocks developed during calcination.

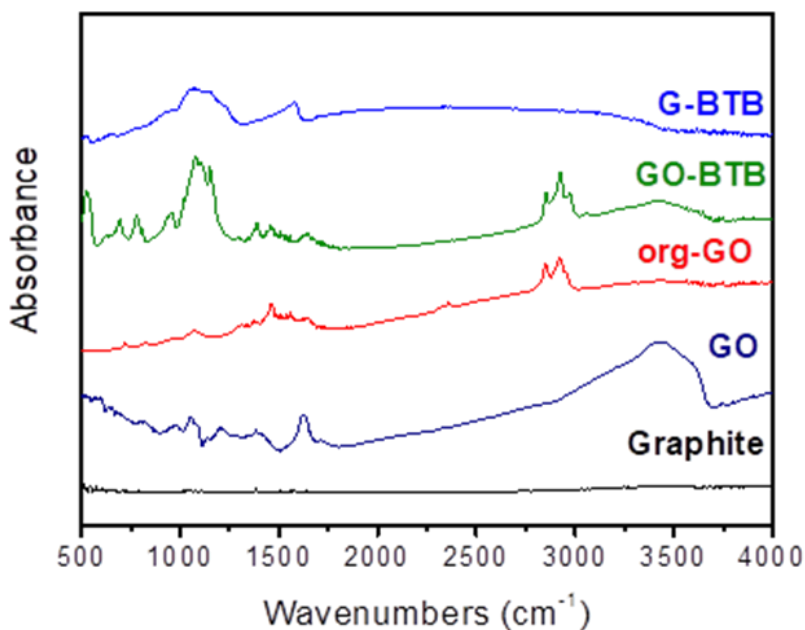


**Figure 3.4.** FTIR spectra of the GO-BTB heterostructure before and after (G-BTB) calcination; the spectra of graphite, pristine graphene oxide (GO) and graphene oxide intercalated with dodecylamine (org-GO) are plotted for comparison.

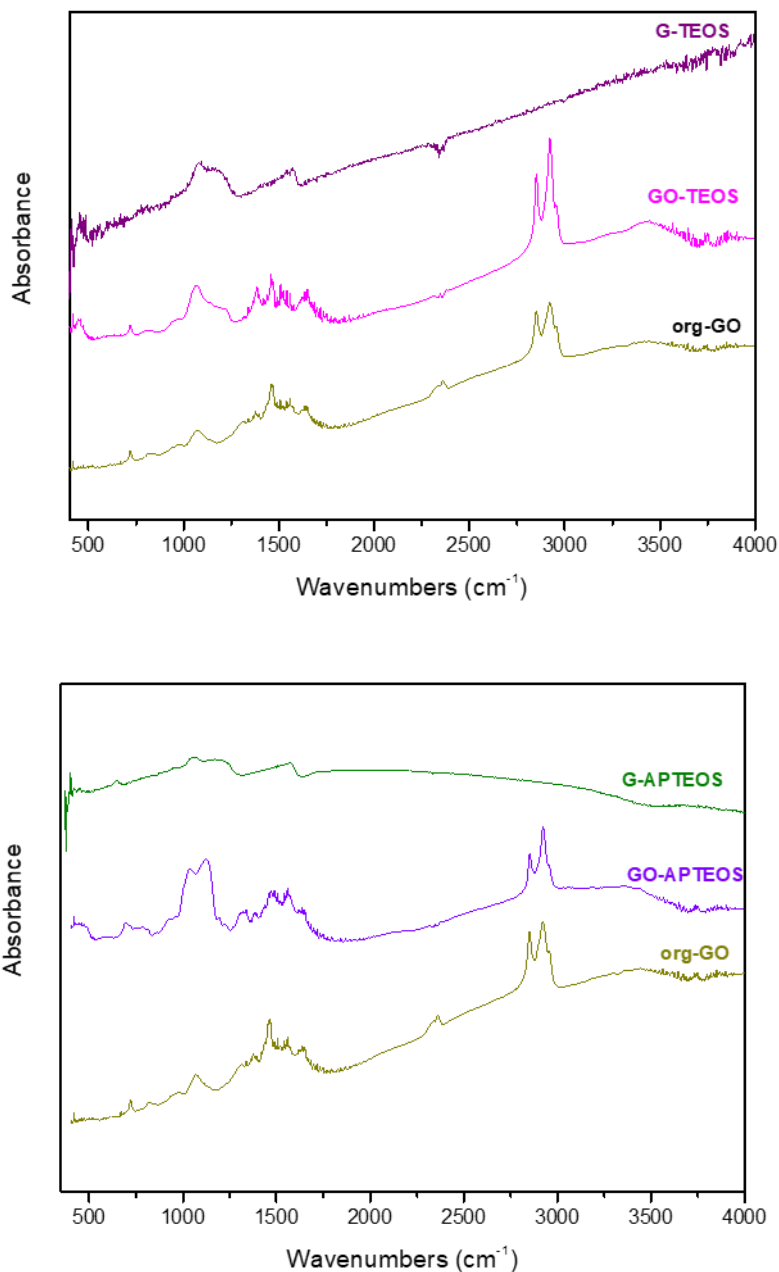


**Figure 3.5.** FTIR spectra of graphene oxide intercalated with dodecylamine (org-GO) silylated with tetraethylorthosilicate (GO-TEOS - top panel) and (3-aminopropyl)triethoxysilane (GO-APTEOS - bottom panel) and subsequently calcinated (G-TEOS – top panel, G-APTEOS – bottom panel)

The relative amount of silicon oxide in the three porous structures can be deduced by TGA; Figure 3.6 presents the results for all three heterostructures. The initial, relatively small weight loss up to about 250 °C is due to the removal of the adsorbed water and of hydroxy, epoxy and carboxyl groups present in the graphene oxide layers<sup>12</sup>. When the temperature increases to 450 °C, combustion of dodecylamine takes place<sup>47</sup>, while in the temperature range between 500 and 700 °C, the mass loss attests to the combustion of the graphene layers<sup>48</sup> as well as to the dehydroxylation of the silica networks<sup>49</sup>. The residual mass of 8 % for GO-TEOS, 30 % for GO-APTEOS and 40 % for GO-BTB, corresponds to silicon oxide in each case. These percentages can be explained by the chemical structure of each silica precursor: for APTEOS and BTB alkoxides a larger amount of silica precursor was activated/reacted to give GO-APTEOS and GO-BTB than for the modification with TEOS, which does not have any functional group favouring bonding.

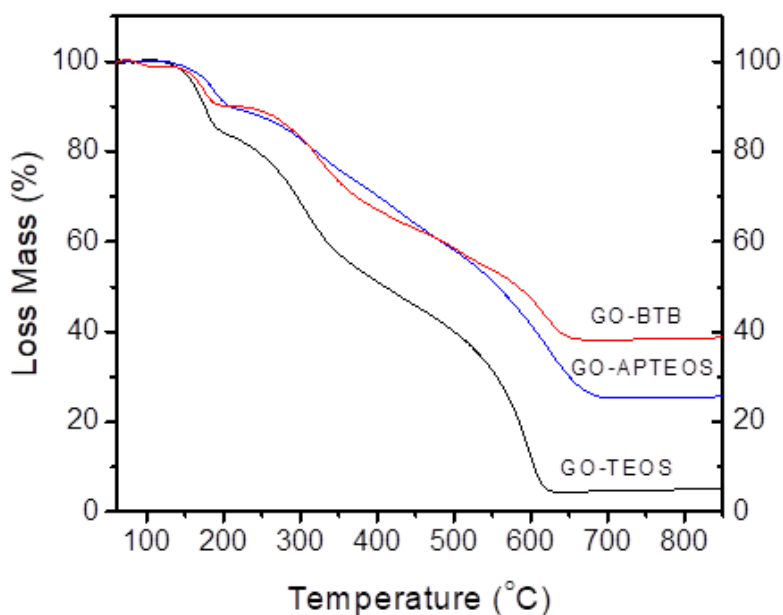


**Figure 3.6.** TGA curves of heterostructures prepared by silylation of organo-modified graphene oxide with 1,4-Bis(triethoxysilyl)-benzene (GO-BTB), with (3-aminopropyl)triethoxysilane (GO-APTEOS) and with tetraethylorthosilicate (GO-TEOS).

To determine the surface area of the heterostructures after calcination (G-BTB, G-APTEOS and G-TEOS), we monitored N<sub>2</sub> adsorption and desorption at 77 K. Figure 3.7 shows the isotherms obtained, all characterized by an H4 hysteresis loop (based on IUPAC classification)<sup>50, 51</sup>, with a shape typical of slit-shaped pores<sup>52, 53</sup>. At low relative pressures ( $P/P_0 < 0.01$ ), the G-BTB heterostructure shows the highest N<sub>2</sub> adsorption, which indicates that a significant amount of micropores is accessible after the creation of the silica network. For this system the BET surface area was calculated to be 576 m<sup>2</sup>/g, or more than twice that of G-APTEOS (227 m<sup>2</sup>/g) and more than 20 times that of G-TEOS (27 m<sup>2</sup>/g). Note that for all three heterostructures the final increase of the N<sub>2</sub> uptake at relative pressures above 0.95 is attributed to adsorption on the external surface and/or the surface of macropores.

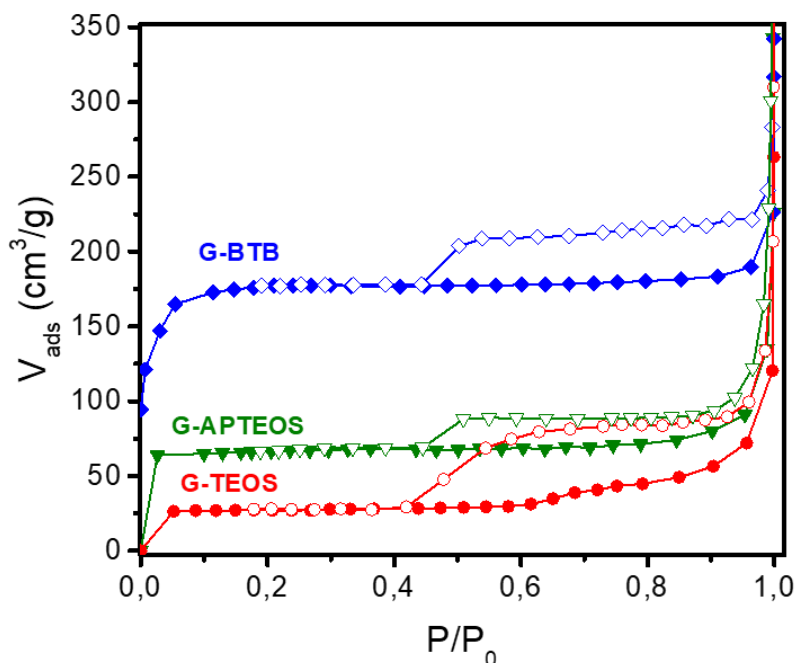


**Figure 3.7.** N<sub>2</sub> adsorption (full symbols)-desorption (empty symbols) isotherms at 77 K of heterostructures prepared by silylation of organo-modified graphene oxide with either 1,4-Bis(triethoxysilyl)-benzene, or with (3-aminopropyl)triethoxysilane, or with tetraethylorthosilicate, and calcinated to give G-BTB, G-APTEOS and G-TEOS.

Hence, we followed all modification steps leading to the G-BTB sample by X-ray photoelectron spectroscopy. The XPS survey scan of the G-BTB is shown in Figure 3.8(a) (top panel). All the expected elements are observed and there is no indication of presence of any kind of contaminant. C and O are the main constituents of the sample, while the Au signature is ascribed to the gold surface where the sample was deposited. The C:Si ratio amounts to  $6.8 \pm 0.6$ , which is comparable with the C:Si ratio before the calcination step, and confirms the presence of BTB molecules in the GO/dodecylamine matrix. The C1s spectrum of org-GO in Figure 3.8(b) shows an asymmetrical peak, which requires four components to obtain a good fit; the main component at a binding energy of 284.8 eV (marked in blue in Figure 3.8(b)) can be ascribed to C-C/C=C species, while the other peaks located at 286.0, 287.2 and 288.7 eV can be assigned to C-O/C-N (yellow), C=O/C-O-C (green), COOH (light red) bonds, respectively<sup>54, 55</sup>. The same four components also contribute to the C1s line in the cases of GO-BTB (see Figure 3.8(c)) and of G-BTB (see Figure 3.8(d)). All percentages indicating the relative amounts of carbon atoms involved in each type of bond as deduced from the XPS measurements for org-GO, GO-BTB and G-BTB are shown in Table 3.1. The O1s core levels of all the samples are shown in Figure 3.9. The corresponding Si2p lines of GO-BTB and G-BTB in Figures 7(f, g) are centred at 102.5 eV, a binding energy typical of Si-O/Si-O-C species<sup>56</sup>. As expected, no Si signal is found for org-GO (Figure 3.8(e)). In addition, the Si2s core level spectrum was also acquired to corroborate the presence of only one chemical species of silicon in both samples (see Figure 3.10). The Si-O-C component is difficult to identify in the C1s peak because of the strong C-C/C=C and C-O/C-N signals<sup>57</sup>.

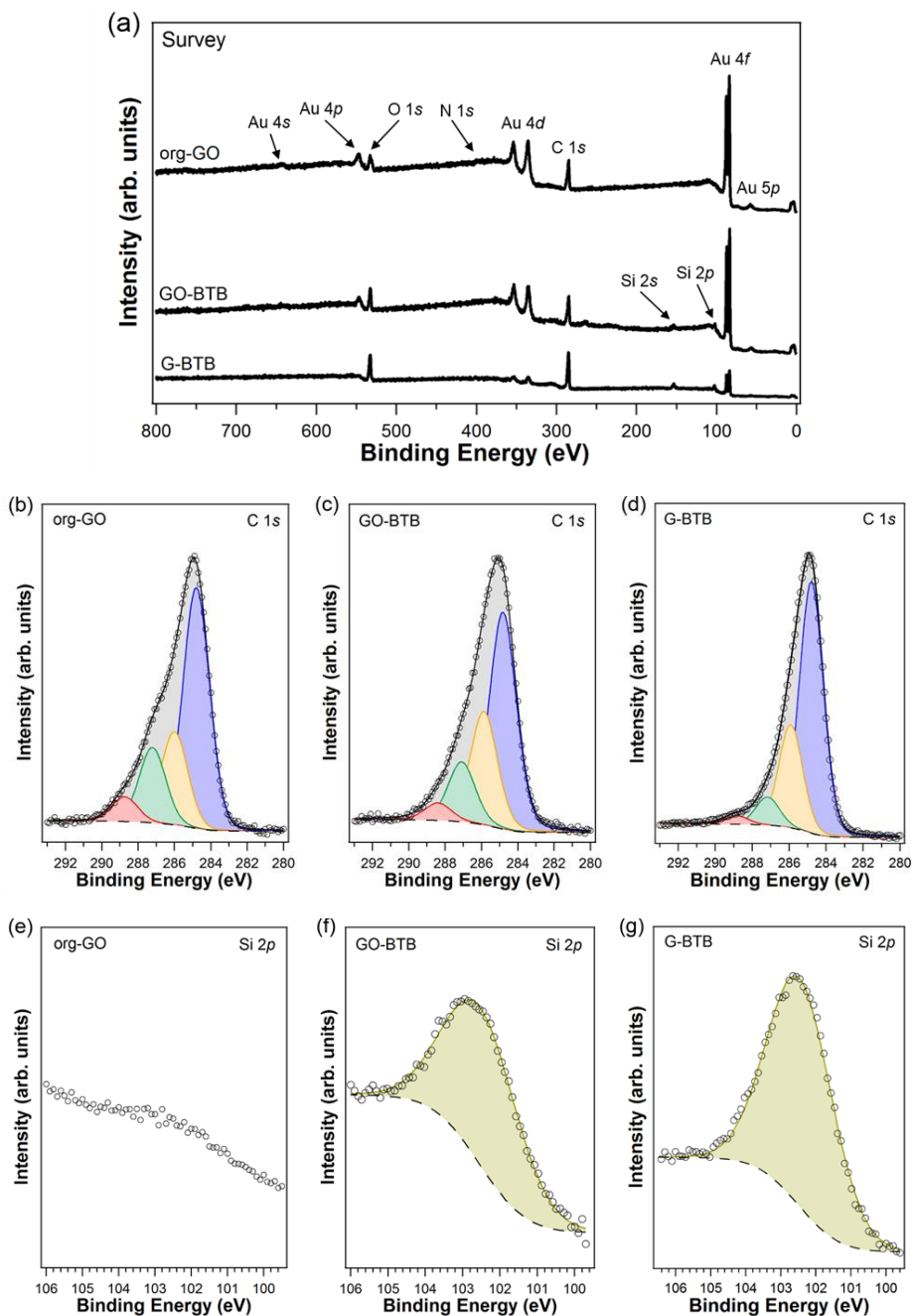


**Figure 3.8.** Survey scan (top panel (a)), C1s (b-d) and Si2p (e-g) XPS spectra of graphene oxide intercalated with dodecylamine before (org-GO), after silylation with 1,4-Bis(triethoxysilyl)-benzene (GO-BTB) and after subsequent calcination (G-BTB) (dots) and corresponding fits (full lines); for the differently coloured peaks see text.

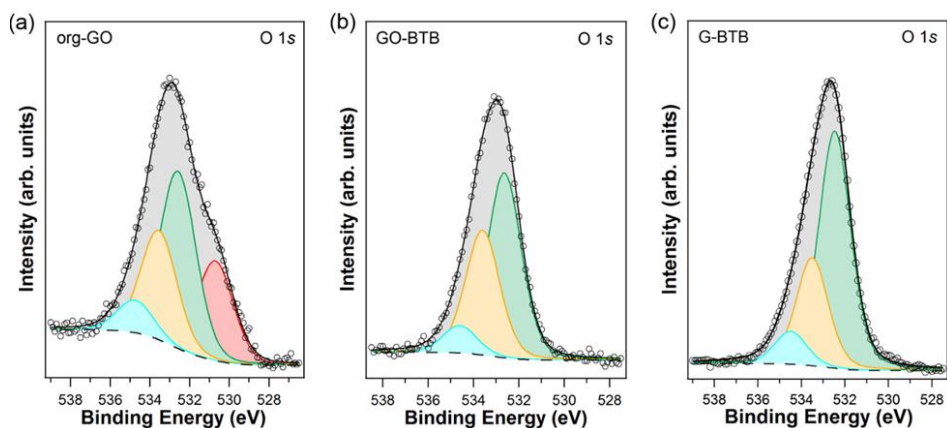


**Figure 3.9.** XPS spectra of the O1s core level region of graphene oxide intercalated with dodecylamine (a) before (org-GO) and (b) after silylation with 1,4-Bis(triethoxysilyl)-benzene (GO-BTB) and (c) after subsequent calcination (G-BTB). The red component is assigned to COO chemical species while the green and yellow components are ascribed to C=O/Si-O-C/C-Si-O and C-O respectively. Finally, the light blue peak is attributed to adsorbed water.<sup>58</sup>

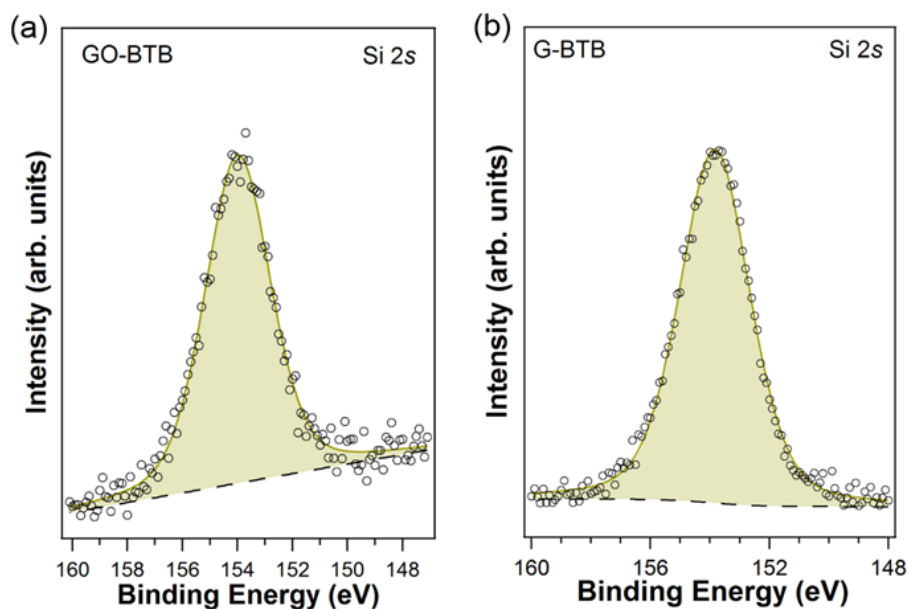


**Figure 3.10.** XPS spectra of the Si2s core level region of (a) GO-BTB and (b) G-BTB samples.

The presence of the other two precursors employed in the sol-gel synthesis, which lead to GO-TEOS and GO-APTEOS is also confirmed by X-Ray photoelectron spectroscopy. The C1s and N1s XPS spectra are depicted in Figure 3.11. The C1s photoemission spectra of GO-TEOS (Figure 3.11(a)) and GO-APTEOS (Figure 3.11(b)) are similar to GO-BTB before calcination, discussed above and shown again for comparison (Figure 3.11(c)).

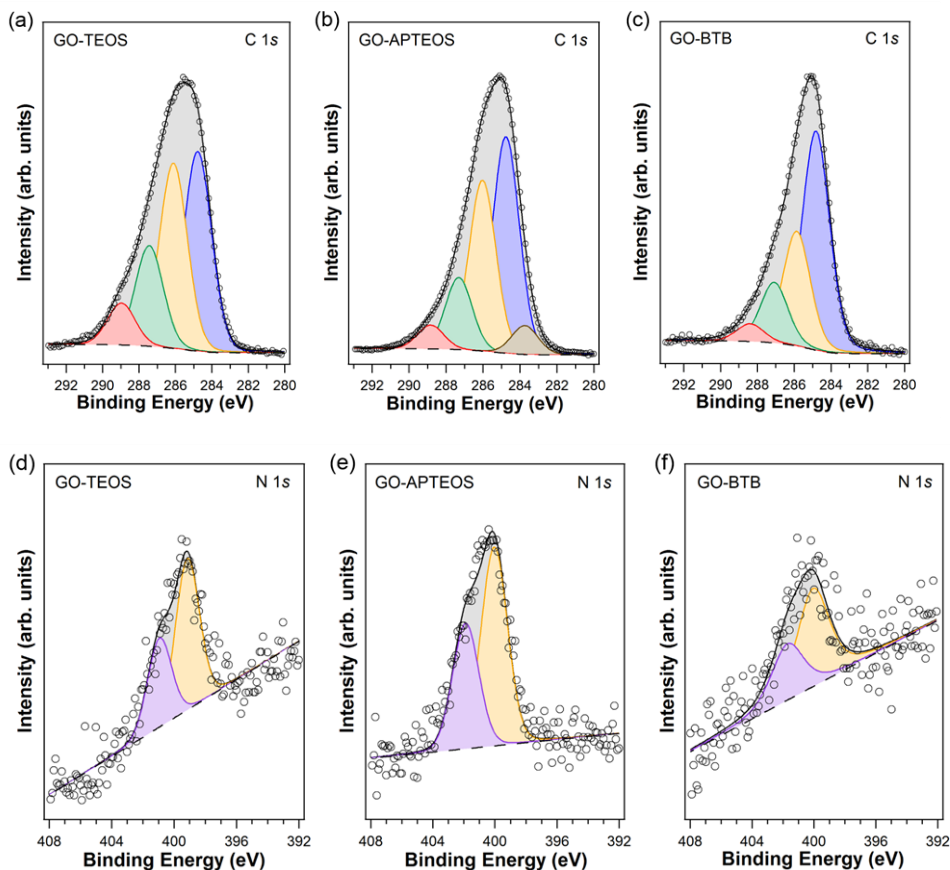


**Figure 3.11.** XPS spectra of the C1s (a-c) and N1s (d-f) core level regions of heterostructures prepared by silylation of organo-modified graphene oxide with 1,4-Bis(triethoxysilyl)-benzene (GO-BTB), with (3-aminopropyl)triethoxysilane (GO-APTEOS) and with tetraethylorthosilicate (GO-TEOS) (dots) and corresponding fits (full lines); for the differently coloured peaks see text.



Table 3.1 summarizes the results of the fits in terms of binding energies, attribution of the various components and relative contribution to the total C1s intensity. Since XPS is a quantitative technique, these percentages indicate the relative amounts of carbon atoms involved in each type of bond. The presence of nitrogen from the intercalated dodecylamine for GO-TEOS, GO-APTEOS and GO-BTB is confirmed by the N1s photoemission lines, shown in Figures 3.11(d–f); note that its position in binding energy at approximately 400.0 eV (yellow in Figure 3.11) indicates that there is no C-N-C bond, which would give rise to a spectral signature at lower binding energies, but that the amines prefer to bind electrostatically with the oxygen groups of the graphene oxide<sup>59</sup>. The peak at higher binding energies for all hybrid materials (lilac coloured in Figure 3.11) arises from protonated amines that may interact as well with the oxygen functional groups of GO (C-OH and C(O)O). In the case of GO-APTEOS there is also the contribution from the amine end groups of APTEOS, which do not participate in the sol-gel reaction.

**Table 3.1.** Binding energies and percentages indicating how much the component contributes to the total C1s intensity; these percentages indicate the relative amounts of carbon atoms involved in each type of bond as deduced from the XPS measurements.

<b>Carbon Species</b>	<b>B.E. (eV)</b>	<b>Sample name and %</b>	<b>Sample name and %</b>	<b>Sample name and %</b>
C-Si	283.8	-	-	<b>GO-APTEOS</b> 5.6
C-C/C=C	284.8	<b>org-GO</b> 55.5 <b>GO-BTB</b> 53.2 <b>G-BTB</b> 70.4	<b>GO-TEOS</b> 40.7	<b>GO-APTEOS</b> 40.3
C-O/C-N	285.9 - 286.2	<b>org-GO</b> 21.5 <b>GO-BTB</b> 27.8	<b>GO-TEOS</b> 30.5	<b>GO-APTEOS</b> 35.4
C-O	285.9	<b>G-BTB</b> 21.2	-	-
C=O/C-O-C	287.1 – 287.4	<b>org-GO</b> 17.3 <b>GO-BTB</b> 14.7 <b>G-BTB</b> 6.3	<b>GO-TEOS</b> 21	<b>GO-APTEOS</b> 14
COOH	288.4 – 288.9	<b>org-GO</b> 5.7 <b>GO-BTB</b> 4.3 <b>G-BTB</b> 2.1	<b>GO-TEOS</b> 7.8	<b>GO-APTEOS</b> 4.7

From the areas of C1s and Si2p lines in the XPS spectra, we calculated the C to Si ratio for all three heterostructures, taking into account the sensitivity factors for each element. GO-BTB (C:Si=6.8±0.5) contains a higher amount of Si than GO-APTEOS (C:Si=65.3±0.9), and GO-TEOS (C:Si=101.4±4.1) ranks lowest in Si content, in agreement with the TGA results discussed above.

Representative scanning electron micrographs of G-BTB are shown in Figure 3.12. Both SEM images (a) and (b) reveal the layered nature of the porous hybrid heterostructure and confirm the high degree of exfoliation of the GO after silylation and calcination.

The CO<sub>2</sub> capture performance of G-BTB was studied at three different temperatures (0, 10, and 20 °C) and for different pressures. The results are presented in Figure 3.13. From these data one deduces CO<sub>2</sub> adsorption capacities of 3.5 mmol/g at 5 bar and of 4.5 mmol/g at 17 bar and 0 °C. At higher temperatures the capacity is slightly lower, which is probably because the kinetic energy of the CO<sub>2</sub> gas molecules is higher and hence the molecules desorb more easily (lower sticking coefficient). Such high values agree with the high BET surface area and the presence of microporosity. Furthermore, the CO<sub>2</sub> adsorption capacity is comparable with that of other graphene based porous materials with higher surface areas, measured under the same conditions<sup>60</sup>. This implies that there is potential for achieving even higher values with further structural optimization.

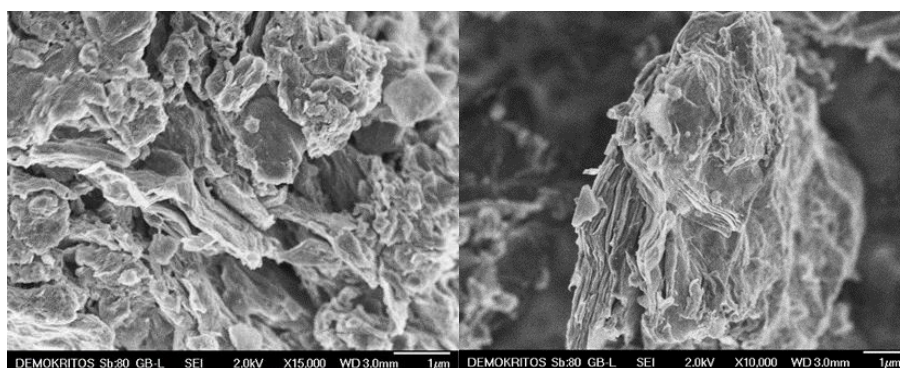


**Figure 3.12.** SEM images of the heterostructure prepared by silylation of organo-modified graphene oxide with 1,4-Bis(triethoxysilyl)-benzene, and calcinated to give G-BTB. The scalebar corresponds to 1 μm

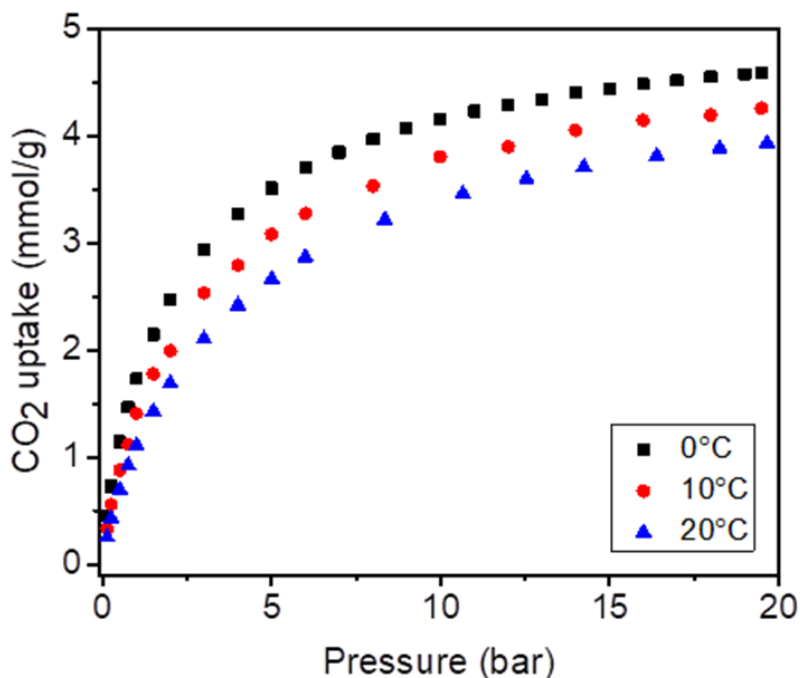


**Figure 3.13.** CO<sub>2</sub> adsorption at 0, 10 and 20 °C on the heterostructure, prepared by silylation of organo-modified graphene oxide with 1,4-Bis(triethoxysilyl)-benzene, and calcinated to give G-BTB.

Thus, G-BTB appears to be a very interesting candidate as CO<sub>2</sub> storage material, which combines the properties of graphene with the very high porosity of silica resulting from the sol-gel procedure.

### 3.4. Conclusions

Graphene-based porous heterostructures were produced by combining organo-modified graphene oxide with three different organo-silica precursors through sol-gel reactions. After one step silylation, the interlayer space increased for all the heterostructures compared to organo-modified GO and was maximum for 1,4-Bis(triethoxysilyl)-benzene due to steric effects. FTIR and XPS spectroscopies gave evidence for the reduction of graphene oxide to graphene after calcination of the heterostructures and confirmed the presence of silica oxide. Thermogravimetric analysis allowed to evaluate the degree of silylation

for each silica precursor, and to identify 1,4- Bis(triethoxysilyl)-benzene (with the bridged phenyl group) as the one giving the highest yield. Thermal treatment is necessary to obtain highly porous materials with sponge-like structures, characterized by a BET surface area of 550 m<sup>2</sup>/g in the case of G-BTB. The latter heterostructure was found to have a high CO<sub>2</sub> adsorption capacity of 3.5 mmol/g at 5 bar and 0 °C, which is promising for further consideration as CO<sub>2</sub> storage material.

## References

1. E. National Academies of Sciences and Medicine, *Gaseous Carbon Waste Streams Utilization: Status and Research Needs*, The National Academies Press, Washington, DC, 2019.
2. D. Y. C. Leung, G. Caramanna and M. M. Maroto-Valer, *Renewable and Sustainable Energy Reviews*, 2014, **39**, 426-443.
3. X. Shi, H. Xiao, H. Azarabadi, J. Song, X. Wu, X. Chen and K. S. Lackner, *Angewandte Chemie International Edition*, 2020, **59**, 6984-7006.
4. T. C. dos Santos and C. M. Ronconi, *Journal of CO<sub>2</sub> Utilization*, 2017, **20**, 292-300.
5. A. Huang and B. Feng, *International Journal of Hydrogen Energy*, 2018, **43**, 2224-2231.
6. J. Pokhrel, N. Bhorla, S. Anastasiou, T. Tsoufis, D. Gournis, G. Romanos and G. N. Karanikolos, *Microporous and Mesoporous Materials*, 2018, **267**, 53-67.
7. S. Shrivastava, S. Thomas, C. B. Sobhan and G. P. Peterson, *International Journal of Refrigeration*, 2018, **96**, 179-190.
8. K. S. Novoselov, V. I. Fal'ko, L. Colombo, P. R. Gellert, M. G. Schwab and K. Kim, *Nature*, 2012, **490**, 192-200.
9. A. Enotiadis, K. Angjeli, N. Baldino, I. Nicotera and D. Gournis, *Small*, 2012, **8**, 3338-3349.
10. K. Duan, L. Li, Y. Hu and X. Wang, *Scientific Reports*, 2017, **7**, 14012.
11. A. Pedrielli, S. Taioli, G. Garberoglio and N. M. Pugno, *Microporous and Mesoporous Materials*, 2018, **257**, 222-231.
12. A. B. Bourlinos, D. Gournis, D. Petridis, T. Szabo, A. Szeri and I. Dekany, *Langmuir*, 2003, **19**, 6050-6055.
13. D. Saha and M. J. Kienbaum, *Microporous and Mesoporous Materials*, 2019, **287**, 29-55.
14. K. Ohtsuka, *Chemistry of Materials*, 1997, **9**, 2039-2050.
15. I. Nicotera, A. Enotiadis, K. Angjeli, L. Coppola, G. A. Ranieri and D. Gournis, *Journal of Physical Chemistry B*, 2011, **115**, 9087-9097.
16. A. Enotiadis, K. Litina, D. Gournis, S. Rangou, A. Avgeropoulos, P. Xidas and K. Triantafyllidis, *Journal of Physical Chemistry B*, 2013, **117**, 907-915.
17. P. A. Zapata, C. Belver, R. Quijada, P. Aranda and E. Ruiz-Hitzky, *Applied Catalysis A: General*, 2013, **453**, 142-150.

18. J. T. Klopogge, L. V. Duong and R. L. Frost, *Environmental Geology*, 2005, **47**, 967-981.
19. A. Gil, S. A. Korili and M. A. Vicente, *Catalysis Reviews*, 2008, **50**, 153-221.
20. G. Balomenou, P. Stathi, A. Enotiadis, D. Gournis and Y. Deligiannakis, *Journal of Colloid and Interface Science*, 2008, **325**, 74-83.
21. I. K. Tonlé, T. Diaco, E. Ngameni and C. Detellier, *Chemistry of Materials*, 2007, **19**, 6629-6636.
22. G. Zhao, L. Jiang, Y. He, J. Li, H. Dong, X. Wang and W. Hu, *Advanced Materials*, 2011, **23**, 3959-3963.
23. J. Yan, J. Liu, Z. Fan, T. Wei and L. Zhang, *Carbon*, 2012, **50**, 2179-2188.
24. Q. Ke and J. Wang, *Journal of Materiomics*, 2016, **2**, 37-54.
25. H. Banda, S. Périé, B. Daffos, P.-L. Taberna, L. Dubois, O. Crosnier, P. Simon, D. Lee, G. De Paëpe and F. Duclairoir, *ACS Nano*, 2019, **13**, 1443-1453.
26. X. Hu, D.-P. Wang, X.-H. Xia, Y.-X. Chen, H.-B. Liu and Z.-Q. Gu, *Journal of Nanoscience and Nanotechnology*, 2019, **19**, 7269-7277.
27. Y. Matsuo, T. Tabata, T. Fukunaga, T. Fukutsuka and Y. Sugie, *Carbon*, 2005, **43**, 2875-2882.
28. M. A. Wahab and C. He, *Langmuir*, 2009, **25**, 832-838.
29. M. A. Wahab, H. Hussain and C. He, *Langmuir*, 2009, **25**, 4743-4750.
30. M. A. Wahab, I. Imae, Y. Kawakami, I. Kim and C.-S. Ha, *Microporous and Mesoporous Materials*, 2006, **92**, 201-211.
31. M. A. Wahab, Kim, II and C.-S. Ha, *Microporous and Mesoporous Materials*, 2004, **69**, 19-27.
32. M. A. Wahab, I. Kim and C.-S. Ha, *Journal of Solid State Chemistry*, 2004, **177**, 3439-3447.
33. M. A. Wahab, I. Imae, Y. Kawakami and C.-S. Ha, *Chemistry of Materials*, 2005, **17**, 2165-2174.
34. Y. Matsuo, Y. Nishino, T. Fukutsuka and Y. Sugie, *Carbon*, 2007, **45**, 1384-1390.
35. Y. Matsuo, T. Komiya and Y. Sugie, *Carbon*, 2009, **47**, 2782-2788.
36. Y. Matsuo, S. Ueda, K. Konishi, J. P. Marco-Lozar, D. Lozano-Castelló and D. Cazorla-Amorós, *International Journal of Hydrogen Energy*, 2012, **37**, 10702-10708.
37. J. Maruyama, S. Akita, Y. Matsuo and Y. Muramatsu, *Carbon*, 2014, **66**, 327-333.

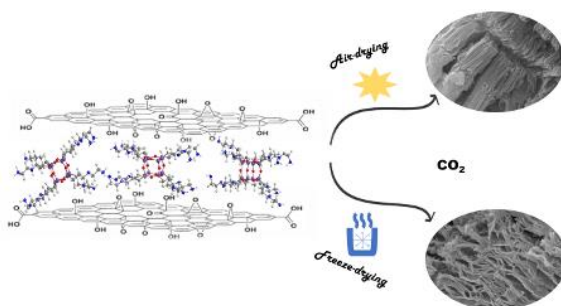
38. S. Rana, S. Maddila, K. Yalagala, S. Maddila and S. B. Jonnalagadda, *ChemistryOpen*, 2015, **4**, 703-707.
39. H. D. Yoo, Y. Park, J. H. Ryu and S. M. Oh, *Electrochimica Acta*, 2011, **56**, 9931-9936.
40. Y. Matsuo, T. Komiya and Y. Sugie, *Journal of Physics and Chemistry of Solids*, 2012, **73**, 1424-1427.
41. Y. Matsuo, A. Hayashida and K. Konishi, *Frontiers in Materials*, 2015, **2**.
42. L. Staudenmaier, *Ber. Deut. Chem. Ges.*, 1898, **31**, 1481.
43. R. Y. N. Gengler, A. Veligura, A. Enotiadis, E. K. Diamanti, D. Gournis, C. Jozsa, B. J. van Wees and P. Rudolf, *Small*, 2010, **6**, 35-39.
44. D. V. Stergiou, E. K. Diamanti, D. Gournis and M. I. Prodromidis, *Electrochemistry Communications*, 2010, **12**, 1307-1309.
45. I. Dekany, R. Kruger-Grasser and A. Weiss, *Colloid and Polymer Science*, 1998, **276**, 570-576.
46. C. Zhang, W. Lv, X. Xie, D. Tang, C. Liu and Q.-H. Yang, *Carbon*, 2013, **62**, 11-24.
47. F. Kooli, Y. Liu, K. Hbaieb and R. Al-Faze, *Microporous and Mesoporous Materials*, 2016, **226**, 482-492.
48. H.-K. Jeong, Y. P. Lee, M. H. Jin, E. S. Kim, J. J. Bae and Y. H. Lee, *Chemical Physics Letters*, 2009, **470**, 255-258.
49. S. Ek, A. Root, M. Peussa and L. Niinistö, *Thermochimica Acta*, 2001, **379**, 201-212.
50. K. S. W. Sing, D. H. Everett, R. A. W. Haul, L. Moscou, R. A. Pierotti, J. Rouquerol and T. Siemieniewska, *Pure and Applied Chemistry*, 1985, **57**, 603-619.
51. G. N. Kalantzopoulos, A. Enotiadis, E. Maccallini, M. Antoniou, K. Dimos, A. Policicchio, E. Klontzas, E. Tylianakis, V. Binas, P. N. Trikalitis, R. G. Agostino, D. Gournis and G. E. Froudakis, *International Journal of Hydrogen Energy*, 2014, **39**, 2104-2114.
52. S. Letaïef, M. A. Martín-Luengo, P. Aranda and E. Ruiz-Hitzky, *Advanced Functional Materials*, 2006, **16**, 401-409.
53. Z. Qian, G. Hu, S. Zhang and M. Yang, *Physica B: Condensed Matter*, 2008, **403**, 3231-3238.
54. K. Spyrou, M. Calvaresi, E. A. K. Diamanti, T. Tsoufis, D. Gournis, P. Rudolf and F. Zerbetto, *Advanced Functional Materials*, 2015, **25**, 263-269.
55. P. Stathi, D. Gournis, Y. Deligiannakis and P. Rudolf, *Langmuir*, 2015, **31**, 10508-10516.

56. A. Kaur, P. Chahal and T. Hogan, *IEEE Electron Device Letters*, 2016, **37**, 142-145.
57. A. Avila, I. Montero, L. Galán, J. M. Ripalda and R. Levy, *Journal of Applied Physics*, 2001, **89**, 212-216.
58. K. Haubner, J. Murawski, P. Olk, L. M. Eng, C. Ziegler, B. Adolphi and E. Jaehne, *ChemPhysChem*, 2010, **11**, 2131-2139.
59. F. Cecchet, M. Pilling, L. Hevesi, S. Schergna, J. K. Y. Wong, G. J. Clarkson, D. A. Leigh and P. Rudolf, *The Journal of Physical Chemistry B*, 2003, **107**, 10863-10872.
60. S. Chowdhury and R. Balasubramanian, *Industrial & Engineering Chemistry Research*, 2016, **55**, 7906-7916.



## Chapter 4: A diamino-functionalized silsesquioxane pillared graphene oxide for CO<sub>2</sub> capture

In the race for viable solutions that could slow down carbon emissions and help in meeting the climate change targets a lot of effort is being made towards the development of suitable CO<sub>2</sub> adsorbents with high surface area, tuneable pore size and surface functionalities that could enhance selective adsorption. In the study reported in this chapter, we explored the use of silsesquioxane pillared graphene oxide for CO<sub>2</sub> capture; we modified silsesquioxane loading and processing parameters in order to obtain pillared structures with nanopores of the tailored size and surface properties to maximize the CO<sub>2</sub> sorption capacity. Powder X-ray diffraction, X-ray photoelectron and Fourier transform infrared spectroscopies, thermogravimetric analysis, surface area measurements and CO<sub>2</sub> adsorption measurements were employed to characterize the materials and evaluate their performance. Through this optimisation process, materials with good CO<sub>2</sub> storage capacities of up to 1.7/1.5 mmol/g at 273 K/298 K in atmospheric pressure, were achieved.



---

*Published as:*

*A diamino-functionalized silsesquioxane pillared graphene oxide for CO<sub>2</sub> capture, Eleni Thomou, Viktoria Sakavitsi, Giasemi K. Angeli, Konstantinos Spyrou, Konstantinos G. Froudas, Evmorfia K. Diamanti, George E. Romanos, Georgios N. Karanikolos, Pantelis N. Trikalitis, Dimitrios Gournis and Petra Rudolf, RSC Advances, 11, 13743-13750, 2021*

## 4.1. Introduction

The level of atmospheric carbon dioxide emissions, one of the main contributors to global warming, has been increasing dramatically year after year, and despite the attempts towards the moderation and decrease of greenhouse gas production the situation seems irreversible. CO<sub>2</sub> is mainly generated from fossil fuel combustion and since there will be no substitute main energy source in the immediate future, the most promising plan of action is Carbon Capture, Utilization and Storage (CCUS).<sup>1</sup>

The capture process of CCUS is focused mainly on industries with high CO<sub>2</sub> emissions, such as power plants, refineries and oil production, while Enhanced Oil Recovery (EOR), although not of universal application, offers a unique financial incentive for capturing carbon: using waste CO<sub>2</sub> as a source material for producing hydrocarbons and at the same time preventing its harmful release into the atmosphere. In EOR CO<sub>2</sub> is injected in almost depleted oil fields in order to force out residual oil and natural gas. The problematic amine-based and ammonia solutions that have been broadly used until now for CO<sub>2</sub> capture, need to be replaced by sorbents that are low-cost, easy to scale up and that can be regenerated and reused at low energy cost.<sup>2,3</sup> It is well-known that carbon materials such as amorphous carbon, nanotubes, fibers and graphite can be used as sorbents/sieves,<sup>4-9</sup> catalytic substrates,<sup>10</sup> membranes,<sup>11</sup> *etc.* due to their low mass in combination with chemical inertness, thermal stability and mechanical properties.

Theoretically, defect-free isolated graphene sheets have a very high surface area (2630 m<sup>2</sup>/g),<sup>12</sup> in addition to being easily (chemically) modified and exhibiting superior mechanical and thermal stability. Graphene is also chemically inert and thus represents an ideal system for sorption and catalysis applications. If the full scientific and technological potential of graphene is to be achieved, lightweight, open 3D structures with high surface area, tuneable pore size and aromatic functionalities must be synthesized. However, the direct use of the unique surface properties of isolated graphene sheets is hampered by the underlying physical–chemical constraints, since due to their aromatic  $\pi$ -systems these structures are extremely prone to aggregation. It is thus clear that the only way to develop nanostructured materials based on graphene or its derivatives as building blocks, is to devise means to maintain the sheets

detached. This can be implemented by taking advantage of the concept of intercalation chemistry and the so-called pillaring method, which involves the insertion of suitable and robust organic and/or inorganic species as pillars between the layers. These methods have been successfully applied in other layered structures such as clays<sup>13</sup> and layered double hydroxides.<sup>14</sup> Pillaring of graphene sheets can provide the necessary structural stability and keep the single carbon layers at a controlled distance, so that a maximum active surface area is easily accessible to small molecules. In such a way, new micro- and meso-porous materials with larger pore sizes than traditional porous materials such as zeolites can be designed. In 2008, using a multiscale theoretical approach Dimitrakakis *et al.*<sup>15</sup> proposed a 3D nanostructure consisting of parallel graphene layers, connected by carbon nanotube (CNT) pillars. This system, consisting mainly of sp<sup>2</sup> hybridized carbon, shows superior structural stability, tuneable porosity and improved storage properties. CNT pillared graphene combines high surface area, narrow and tuneable pore size distributions with available aromatic functionalities arising from both the graphene layers and the CNTs. It is exactly this combination, which makes this class of materials most suitable candidates for the “Holy Grail” storage adsorbent for important gases such as H<sub>2</sub>.<sup>16</sup> Various organic and/or inorganic pillars between graphene layers can impart enhanced and/or diverse properties for gas separation or catalysis, while further “functionalization” can be carried out by the well-established carbon chemistry. Furthermore, by properly choosing the pillaring species, 3D porous structures can be conceived, which are superior to metal organic frameworks (MOFs)<sup>17</sup> in terms of stability at higher pressure and durability in normal environmental conditions.

A particularly promising approach is the intercalation of cubic silsesquioxanes as pillaring species in chemically oxidized graphene (graphene oxide, GO). Cubic siloxanes (silsesquioxanes) are synthesized from the hydrolytic condensation of the corresponding trifunctional organosilicon monomers, and offer the opportunity to realize materials with extremely well-defined dimensions and behaviour.<sup>18,19</sup> Cubic siloxanes of the type X<sub>8</sub>Si<sub>8</sub>O<sub>12</sub>, where X can be -(CH<sub>3</sub>)<sub>3</sub>NH<sub>2</sub>, or -(CH<sub>3</sub>)<sub>3</sub>NH(CH<sub>2</sub>)<sub>2</sub>NH<sub>2</sub>, have been successfully employed as precursor reagents for pillaring inorganic layered solids such as clays<sup>20-24</sup> or metal(IV)-H- phosphates.<sup>25</sup>

In the study reported here we focused on the synthesis and characterization of novel pillared materials where amino-functionalized cubic silsesquioxanes were intercalated among GO layers at different loadings. Silsesquioxanes assure the robustness of the 3-D network of adjacent graphene sheets, while the unreacted amine groups in the open space between the GO sheets warrant strong CO<sub>2</sub> adsorption.

## 4.2. Experimental Section

### 4.2.1. Materials

Graphite (purum, powder <0.1 mm) and N-[3-(trimethoxysilyl) propyl]-ethylenediamine (EDAPTEOS, 97%) were purchased from Sigma Aldrich, whereas potassium chlorate (KClO<sub>3</sub>, 99+%) was acquired from Alfa Aesar, sulfuric acid (H<sub>2</sub>SO<sub>4</sub>, 96 %) and ethanol (absolute for analysis) from Merck, and nitric acid (HNO<sub>3</sub>, 65 %) from Penta Chemicals Unlimited, and sodium hydroxide carbonate (NaHCO<sub>3</sub>, >99.7 %) from Riedel-de Haën. All reagents were of analytical grade and used without further purification. The water used in the experiments was distilled and deionized.

### 4.2.2. Graphene Oxide Synthesis

GO was produced through graphite powder oxidation using a modified Staudenmaier's method<sup>26, 27</sup> that leads to a higher amount of epoxy groups compared to carboxy and hydroxy groups, and thereby a starting material that favours reactions with amine ending moieties.<sup>28</sup> In a typical synthesis, 10 g of powdered graphite were added to a mixture of concentrated sulfuric acid (400 mL) and nitric acid (200 mL), while stirring and cooling in an ice-water bath in order to absorb the heat released during the very exothermic chemical reaction. Potassium chlorate powder (200 g) was added to the mixture in small portions, while stirring and cooling. The reaction was quenched after 18 h by pouring the mixture into distilled water and the oxidation product was washed until an almost neutral (~6) pH value was reached. The sample was then dried at room temperature by air-drying, where the sample was spread onto a glass plate and left to dry, as well as by freeze-drying (a laboratory freeze dryer BK-FD10 series by Biobase was used), where the sample was redispersed in 150 mL of H<sub>2</sub>O, frozen by contact with liquid nitrogen and the ice was subsequently removed by sublimation at low pressure.

### 4.2.3. Formation of the pillaring agent

The organosilane used in this study was N-[3-(trimethoxysilyl)propyl]-ethylenediamine (EDAPTEOS). The formation of the octameric oligosiloxanes (see Figure 4.1) from the hydrolytic polycondensation of the monomer occurs after dilution of EDAPTEOS in ethanol–water (v/v = 14/1) to give a solution of 0.45 M concentration.<sup>22-25, 29</sup>

### 4.2.4. Preparation of silsesquioxane pillared graphene oxide

A sample of 200 mg of GO was dispersed in 100 mL water by stirring for 24 h. The pH value of the dispersion was adjusted to slightly basic (~7.1) by adding a few drops of 0.1 M NaHCO<sub>3</sub> solution so that amines (–NH<sub>2</sub>) are not protonated and thus easily form covalent bonds. Subsequently, aliquots of the siloxane solution were added such that 1.5, 4.5 and 9 mmol loadings were achieved. Upon addition of the siloxane solution the GO solid swelled instantly and flocculation was noticed (see Figure 4.2(a)). After stirring for 24 h, the GO-organosilane aggregates were washed with water two times, separated by centrifugation and either air-dried (see Figure 4.2(b)), and freeze-dried (see Figure 4.2(c)) as described above. The samples are denoted PILGD<sub>x</sub>AD and PILGD<sub>x</sub>FD (where x is the loading).

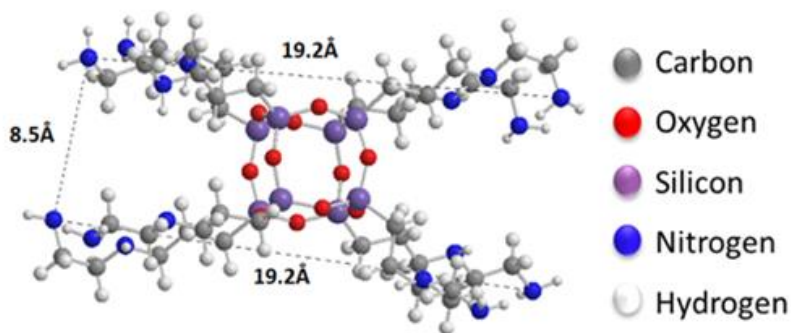


**Figure 4.1.** The cage-like structure of the siloxane

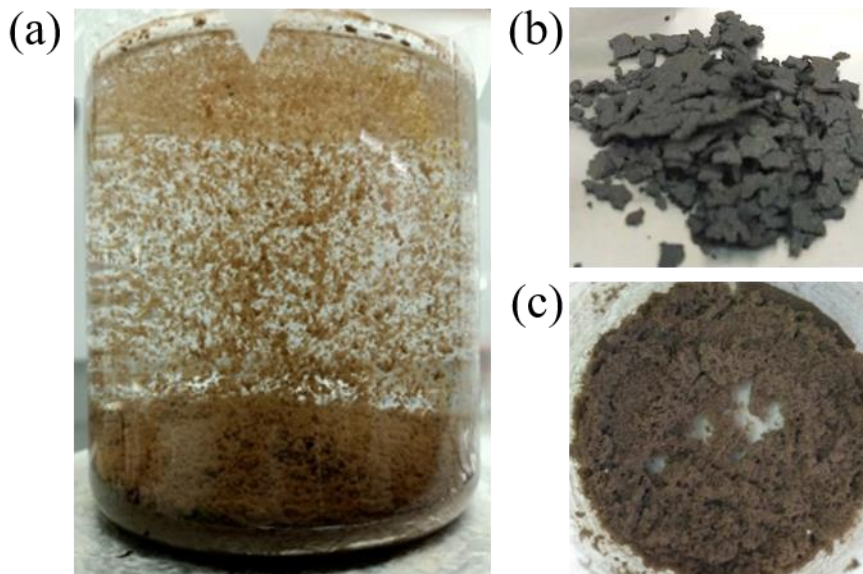


**Figure 4.2.** Photographs presenting the flocculation phenomenon (a), and silsesquioxane-pillared GO after air drying (b) and freeze drying (c)

### 4.3. Results and Discussion

Oxidizing graphite powder following the modified Staudenmaier's method,<sup>26</sup> produces exfoliated hydrophilic single layer flakes of graphene oxide (GO), which are perfectly dispersed in water. As detailed above, the pillaring solution was derived from controlled hydrolysis of N-[3-(trimethoxysilyl) propyl]-ethylenediamine (EDAPTEOS) and hydrolytic condensation of the silanes takes place smoothly in an ethanol-H<sub>2</sub>O solution, resulting in the creation of an octameric cubic structure.<sup>23,25</sup> The immediate flocculation observed when the ethanolic solution containing the pillaring agent was added to the GO suspension, hints to the insertion of cubic siloxanes between the GO layers through covalent bonding via the amide functionality of the organosilane molecules. Interaction of the primary aliphatic amines of the EDAPTEOS end groups with GO is expected to take place mainly via nucleophilic substitution reactions on the epoxy groups of GO.<sup>27, 30</sup>

The X-ray diffraction (XRD) patterns of the pristine graphite, GO and the PILGD samples are shown in Figure 4.3. Note that the sharp peak at 21.4° visible in most of the samples, originates from the silicon oxide used as a

substrate for the measurements. The pattern of pure graphite exhibits a peak at  $26.6^\circ$  corresponding to the basal spacing  $d_{002} = 3.34 \text{ \AA}$ , while for graphene oxide a 001 reflection<sup>30, 31</sup> appears at  $11.9^\circ$ , consistent with a basal spacing of  $d_{001} = 7.4 \text{ \AA}$ . Treatment of GO with the siloxane cubes leads to a shift of the peak to lower angles, which confirms an expansion of the interlayer space by the organofunctionalized silicon oxide cubes inserted as bonded pillars between GO sheets. In the case of the air-dried samples, two peaks are distinguished in the XRD patterns, one in the range of  $6.3\text{--}7.7^\circ$  and a second one at  $9.6^\circ$ . The existence of these two peaks is due to the different orientations of the cubes, facilitated by the flexibility of the aliphatic chains.<sup>32</sup> Applying the Bragg formula ( $n\lambda = 2d \sin\theta$ ), and bearing in mind that the thickness of a graphene oxide layer is  $6.1 \text{ \AA}$ ,<sup>33</sup> the interlayer distances giving rise to the two peaks are calculated to amount to 11.4, 14 and  $9.2 \text{ \AA}$ , respectively. Taking into account the intercalant's size as marked in Figure 4.1, one concludes that it has adopted a very slightly inclined orientation between the GO sheets. There is also a very broad feature centred around the peak position of pure GO, which indicates that not all layers are pillared and very small coherently diffraction domains of unfilled GO persist in between the pillared structure. On the other hand, in the case of the freeze-dried samples the peak positions cannot readily be discerned because the diffraction pattern shows very broad features, pointing to small coherently diffracting domains.

Thermogravimetric analysis (TGA) was performed on the air-dried silsesquioxane-pillared structures in order to determine the relative amount of silicon oxide for each loading; the results are presented in Figure 4.4. Heating up to  $250 \text{ }^\circ\text{C}$  an initial mass loss of  $\sim 24 \%$  is noticed, which is attributed to the removal of the adsorbed water and of the oxygen containing groups of the GO.<sup>30</sup> Increasing the temperature to  $350 \text{ }^\circ\text{C}$ , a second mass loss of  $\sim 12 \%$  is recorded, which can be assigned to the removal of the organic groups bonded to the siloxane cubes, and successively a third weight loss of approximately  $45 \%$  indicates combustion of the graphene layers. From the remaining weight after heating to  $850 \text{ }^\circ\text{C}$ , we calculated that the inorganic silicon oxide cubes correspond approximately to 10.8, 13.1 and  $14.2 \%$  of the total mass of the pillared material obtained with 1.5, 4.5 and  $9 \text{ mmol}$  loading respectively.

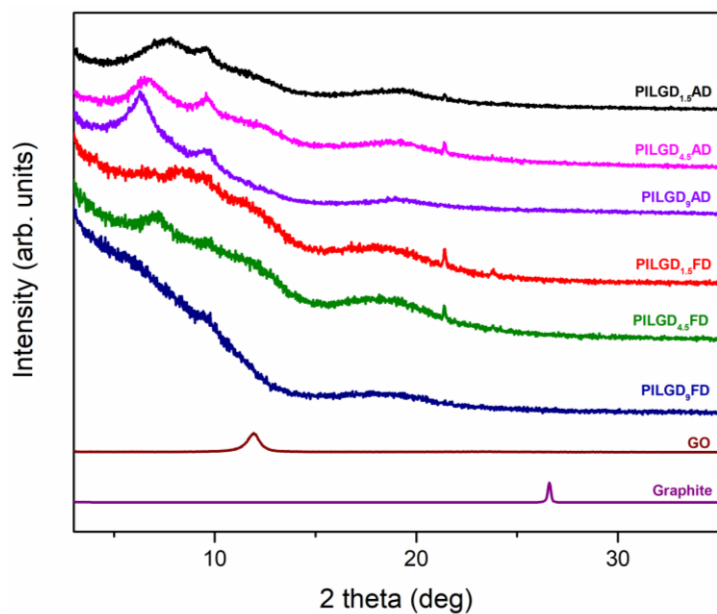


**Figure 4.3.** XRD patterns of pristine graphite, graphene oxide, and silsesquioxane- pillared graphene oxide prepared with different loadings and either air-dried or freeze-dried

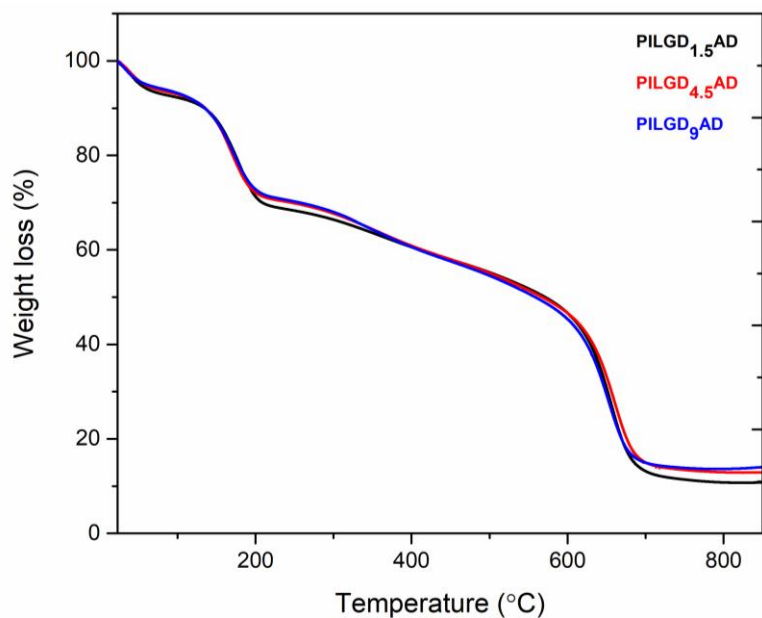


**Figure 4.4.** Thermogravimetric analysis curves of the three air-dried silsesquioxane-pillared graphene oxide structures



Note that the silicon oxide cubes' content does not scale with the loading because in the last step of the synthesis the samples were washed two times to remove the excess amount of cubes as well as the loosely bonded ones.

An additional characterisation tool, which can confirm the successful insertion of the silsesquioxane cubes between GO sheets, is Fourier transform infrared (FTIR) spectroscopy. As shown in Figure 4.5, while pure graphite is an IR inactive solid, graphene oxide exhibits all the IR features expected after oxidation, namely at  $3411\text{ cm}^{-1}$  the hydroxyl stretching vibrations of the C–OH groups, at  $1630\text{ cm}^{-1}$  the C=O stretching vibrations of the –COOH groups, at  $1069\text{ cm}^{-1}$  the C–O stretching vibrations, at  $1294\text{ cm}^{-1}$  the asymmetric stretching of C–O–C bridges in epoxy groups, and at  $1646\text{ cm}^{-1}$  the C=C stretching vibrations of the aromatic ring.<sup>34,35</sup> In the case of the pillared samples, extra peaks appear in the spectrum, which are attributed to the presence of the silsesquioxane cubes. In fact, the band at  $773\text{ cm}^{-1}$  is assigned to the stretching vibrations of O–Si–O bonds, and the ones at  $445$ ,  $596$ ,  $1067$  and  $1197\text{ cm}^{-1}$  are due to the Si–O–Si bending and stretching vibrations;<sup>32,36</sup> together these spectral features confirm the integrity of the silsesquioxane cubes.

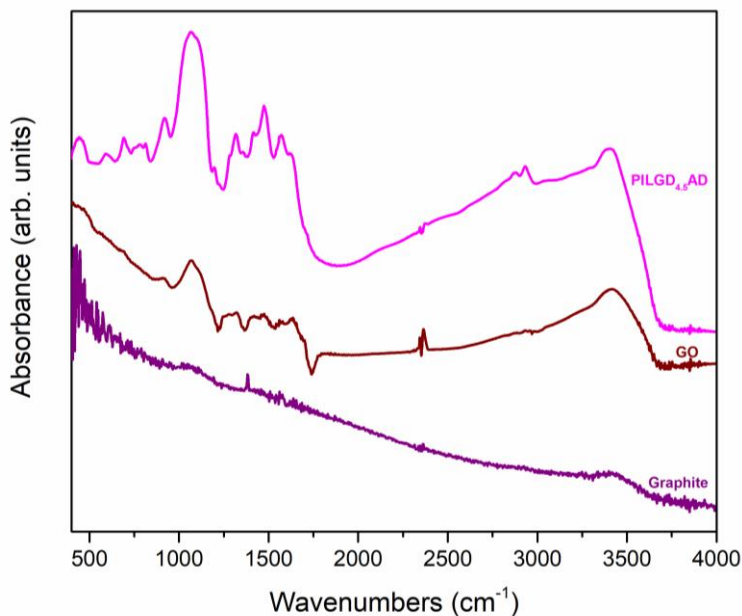


**Figure 4.5.** FTIR spectra of graphite, graphene oxide (GO) and of the air-dried silsesquioxane-pillared graphene oxide structure PILG<sub>4.5</sub>AD

The band at  $692\text{ cm}^{-1}$  is due to the C–H bending vibrations of the aliphatic chains of the silsesquioxane cubes<sup>32</sup> and the one at  $920\text{ cm}^{-1}$  stems from Si–O stretching vibrations.<sup>37</sup> The spectral fingerprints of C–N at  $1315\text{ cm}^{-1}$ , the asymmetric  $\text{N}^+\text{-CH}_3$  deformations<sup>22</sup> at  $1474\text{ cm}^{-1}$ , the  $\text{-NH}_3^+$  deformation<sup>23, 37</sup> at  $1570\text{ cm}^{-1}$  and the  $\text{NH}_2$  deformation at  $1627\text{ cm}^{-1}$  together testify to the integrity of the aliphatic chains of the cubes.<sup>23</sup> Finally, asymmetric and symmetric stretching vibrations of  $\text{-CH}_2\text{-}$  groups observed at  $2931$  and  $2874\text{ cm}^{-1}$  reveal the presence of organosilane molecules in the solid. Analogous spectra were obtained for all the other pillared samples (data not shown here).

X-ray photoelectron spectroscopy (XPS) was performed on the three air-dried silsesquioxane-pillared structures in order to verify the presence and integrity of the siloxane cubes in the interlayer space of GO and also to evaluate the quality of the graphene-based material in terms of chemical moieties present after intercalation. The detailed spectra of the  $\text{C}1s$  and  $\text{N}1s$  core level regions are shown in Figure 4.6.

Deconvolution of the  $\text{C}1s$  spectrum requires five components. The first and most prominent peak at a binding energy (BE) of  $\sim 284.2\text{ eV}$  is attributed to C–C/C=C bonds within the graphene oxide layers and contributes with respectively 41.4, 38.8 and 48.7% of the total  $\text{C}1s$  spectral intensity for  $\text{PILGD}_{1.5}\text{AD}$ ,  $\text{PILGD}_{4.5}\text{AD}$  and  $\text{PILGD}_9\text{AD}$ . The second one at a BE of  $\sim 285.4\text{ eV}$  is due to the C–O bonds of the GO lattice as well as from the C–N bonds of the cubes and makes up 24.7, 24.4 and 31.3 % of the  $\text{C}1s$  spectral intensity for the 3 loadings respectively, while the third component at a BE of  $\sim 286.9\text{ eV}$  originates from the epoxy groups and its lower intensity with respect to pure GO for all 3 loadings (17.7, 17.0 and 11.3 % of the total  $\text{C}1s$  spectral intensity) indicates the formation of covalent bonds.

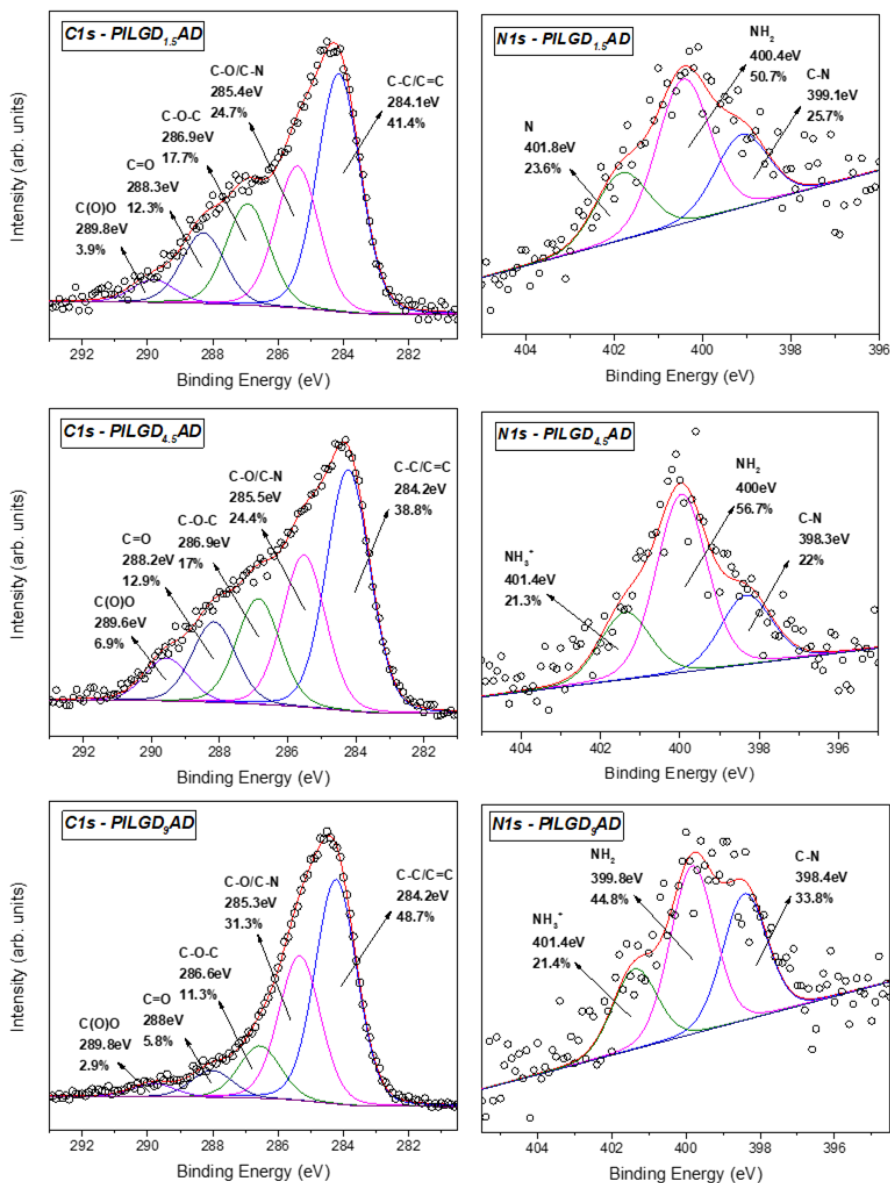


**Figure 4.6.** XPS spectra of the C1s (left panels) and N1s (right panels) core level regions of the silsesquioxane-pillared GO structures obtained with the three different loadings.

**Table 4.1.** Stoichiometry of the air-dried silsesquioxane-pillared GO structures as deduced from the XPS analysis

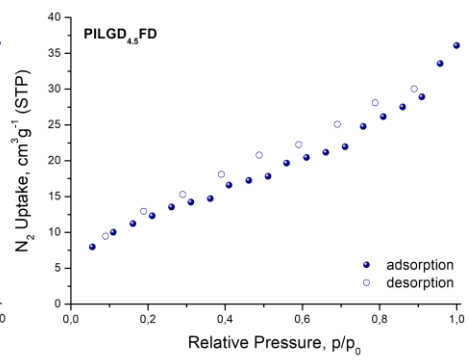
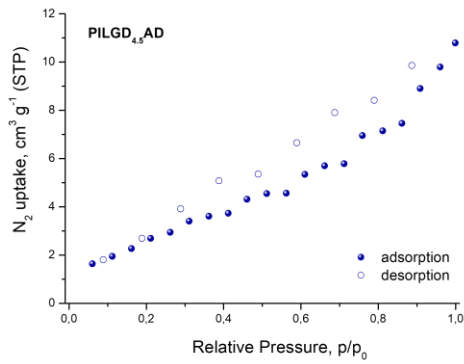
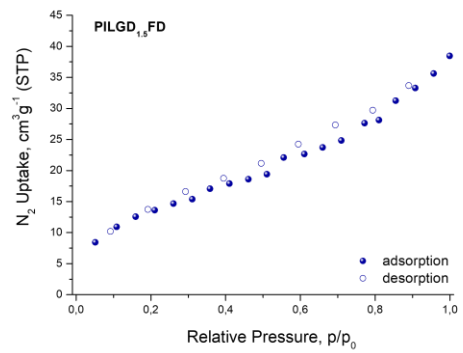
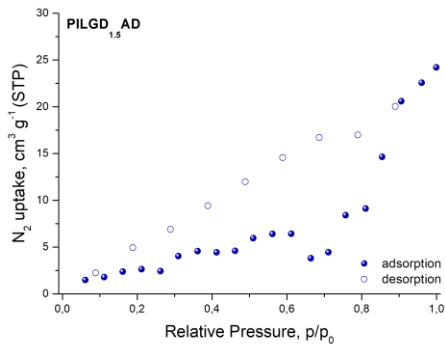
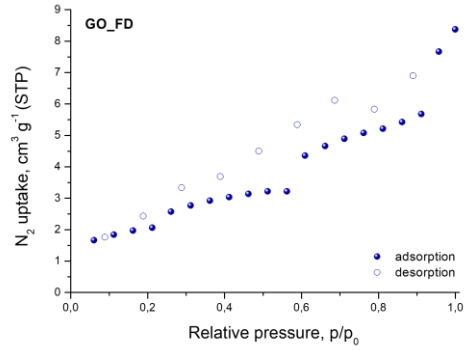
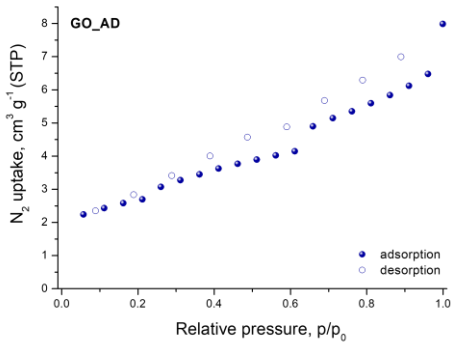
<i>Element</i>	<b>Atomic percentage %</b>		
	<b>PILGD<sub>1.5</sub>AD</b>	<b>PILGD<sub>4.5</sub>AD</b>	<b>PILGD<sub>9</sub>AD</b>
<b>C</b>	78.8	63.9	66.9
<b>O</b>	10.8	21.7	21.7
<b>N</b>	3.5	4.1	4.1
<b>Si</b>	6.9	10.3	7.3

Finally, the two components at BEs of ~288.2 and ~289.8 eV are attributed respectively to C=O bonds (relative intensity 12.3, 12.9 and 5.8 % for the three loadings) and to carboxylic groups present in the graphene oxide sheets (relative spectral intensities 3.9, 6.9 and 2.9 % for the three loadings).

Through the analysis of the XPS spectra of the N1s core level region additional insight on the type of interactions can be gained. The nitrogen spectrum requires three components for a good fit: the first one at a BE of ~398.4 eV is attributed to the covalent bonds formed between the amines and the epoxy groups (relative spectral intensities 25.7, 22 and 33.8 % for the three loadings); the second contribution at ~400 eV is due to amines of the precursor and amounts to respectively 50.7, 56.7 and 44.8 % of the total N1s intensity and the last one at a BE ~401.4 eV stems from protonated amines (relative spectral intensities 23.6, 21.3 and 21.4 % for the three loadings).

The atomic percentages of the elements present in the samples were calculated and are presented in Table 4.1. The silicon content agrees with the data of the thermal analysis of the samples.

The porous structure of the different silsesquioxane-pillared GO samples and of pure GO was studied by recording the N<sub>2</sub> adsorption–desorption isotherms at 77 K; the data are presented in Figure 4.7. The BET specific surface area, deduced from the adsorption data and reported in Table 4.2 for all samples, is significantly higher for the freeze-dried samples. In fact, for the latter it reaches more than 5 times larger values than those of the air-dried ones synthesized with the same silsesquioxane loading.



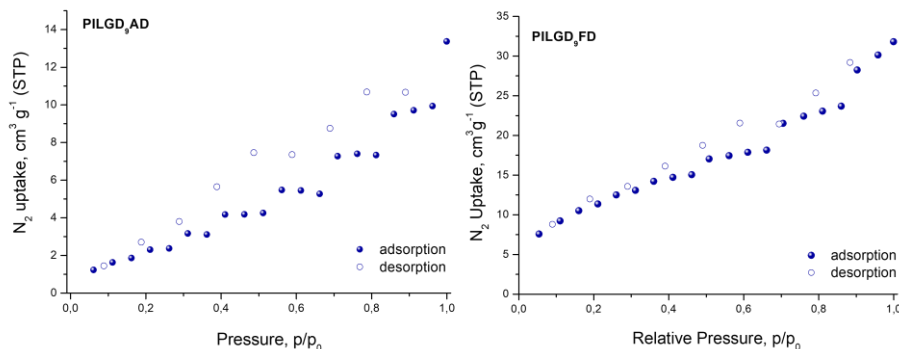


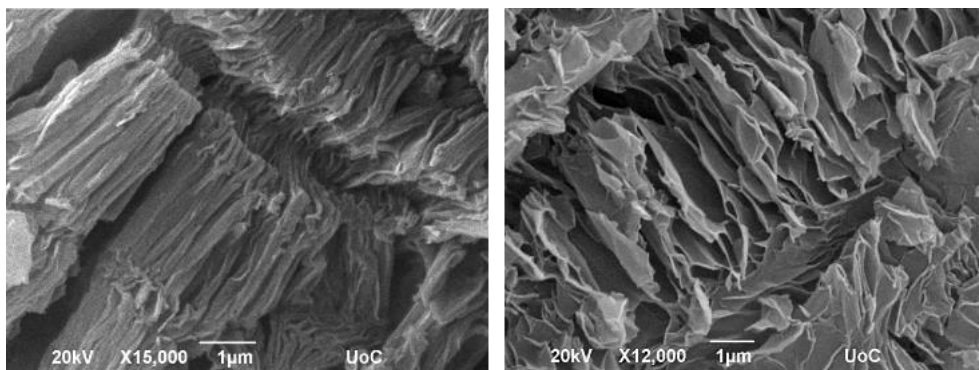
**Figure 4.7.** N<sub>2</sub> adsorption (full symbols)-desorption (empty symbols) isotherms at 77 K for graphene oxide (air dried and freeze-dried) and for all silsesquioxane-pillared GO structures prepared with different loadings and both ways of drying

**Table 4.2.** The values of the specific surface area of GO and silsesquioxane-pillared GO as deduced from N<sub>2</sub> adsorption measurements at 77 K

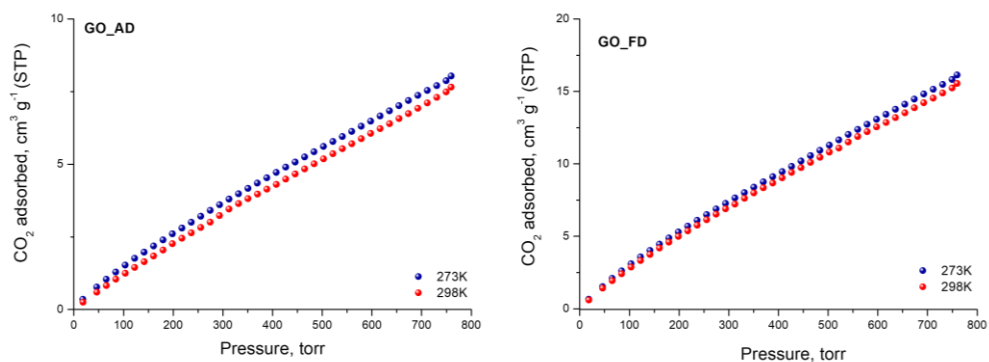
Sample	BET surface area (m <sup>2</sup> /g)	
	AD	FD
GO	9	7
PILGD <sub>1.5</sub>	10	50
PILGD <sub>4.5</sub>	9	46
PILGD <sub>9</sub>	8	42

The pillared structures were examined with SEM in order to spot the differences in the structures for the two different ways of drying; representative images of the PILGD<sub>4.5</sub>AD and PILGD<sub>4.5</sub>FD samples are shown in Figure 4.8. As expected, by simply air drying the samples in ambient conditions, we get compact stacks of graphene oxide layers since with the removal of water the structure shrinks and the layers are only kept apart by the silsesquioxane cubes (left image of Figure 4.7). On the other hand, when freeze-drying is employed, the ice crystals sublime, leaving behind pores in the structure. In the SEM image (Figure 4.8, right picture) one easily discerns a more foam-like macroscopic structure of the sample, very distinct from the one resulting from air-drying. This explains the increased specific surface area for the freeze-dried samples.

The CO<sub>2</sub> adsorption behaviour for all samples was investigated by recording the corresponding adsorption isotherms at 273 K and 298 K, up to 1 bar (see Figure 4.9).



**Figure 4.8.** Representative scanning electron microscopy images of the air-dried (PILGD<sub>4.5</sub>AD, left) and freeze-dried (PILGD<sub>4.5</sub>FD, right) silsesquioxane-pillared GO structures. The scalebar corresponds to 1 μm



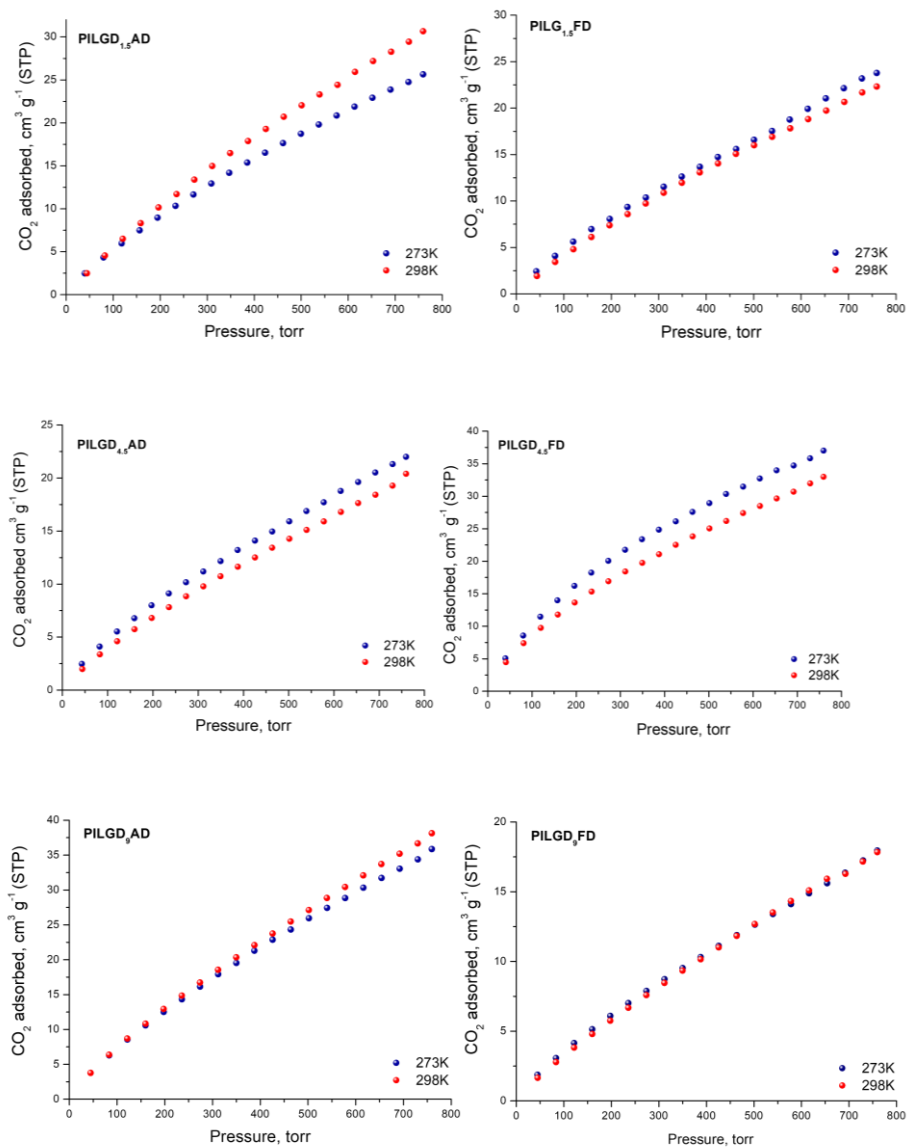


**Figure 4.9.** CO<sub>2</sub> adsorption (full symbols)-desorption (empty symbols) isotherms at 273 K and 298 K up to 1 bar for graphene oxide (air dried and freeze-dried) and for all silsesquioxane-pillared GO structures prepared with different loadings and both ways of drying



For the neat GO samples, although the uptake is relatively poor, the freeze-dried GO is able to capture twice as much CO<sub>2</sub> [16.1 cm<sup>3</sup>/g (0.72 mmol/g) and 15.3 cm<sup>3</sup>/g (0.68 mmol/g), at 273 K and 298 K respectively] as the air-dried one [8 cm<sup>3</sup>/g (0.36 mmol/g) and 7.7 cm<sup>3</sup>/g (0.34 mmol/g), at 273 K and 298 K respectively]. Interestingly, for the pillared freeze-dried samples, the CO<sub>2</sub> uptake at 1 bar as a function of surface coverage, does not follow Vegard's law, meaning that it does not monotonically increase with increasing loading. Instead, it shows a maximum value for the intermediate sample PILGD<sub>4.5</sub>FD, reaching 37 cm<sup>3</sup>/g (1.65 mmol/g) and 32.9 cm<sup>3</sup>/g (1.47 mmol/g), at 273 K and 298 K, respectively (Figure 4.10).

The gravimetric uptake is expected to increase with increasing available pore space and decrease with increasing density of the sample. One can anticipate that the insertion of silsesquioxane pillars improves porosity but also makes the material heavier. The lower CO<sub>2</sub> uptake of the high loading sample, PILGD<sub>9</sub>FD [17.9 cm<sup>3</sup>/g (0.80 mmol/g) at 273 K and 17.8 cm<sup>3</sup>/g (0.79 mmol/g) at 298 K] suggests that this sample is clogged due to an excess of silsesquioxane pillars. In other words, a high amount of pillars reduces the accessible pore space and increases the density of the material, reducing in this way the CO<sub>2</sub> gravimetric uptake. The high CO<sub>2</sub> uptake of PILGD<sub>4.5</sub>FD is also supported by the corresponding isosteric heat of adsorption,  $Q_{st}$ , calculated using the adsorption isotherms at 273 K and 298 K and applying the Clausius–Clapeyron equation. As shown in Figure 4.11, for PILGD<sub>4.5</sub>FD the  $Q_{st}$  at zero coverage is 5.7 kJ/mol; it slightly increases up to 7.4 kJ/mol with increasing loading and drops back to 5.4 kJ/mol at high loadings. This behaviour implies the presence of an energetically uniform adsorption environment that favours CO<sub>2</sub>–CO<sub>2</sub> interactions that contributes to high uptake, as has been observed in other porous materials, including MOFs.<sup>38</sup>

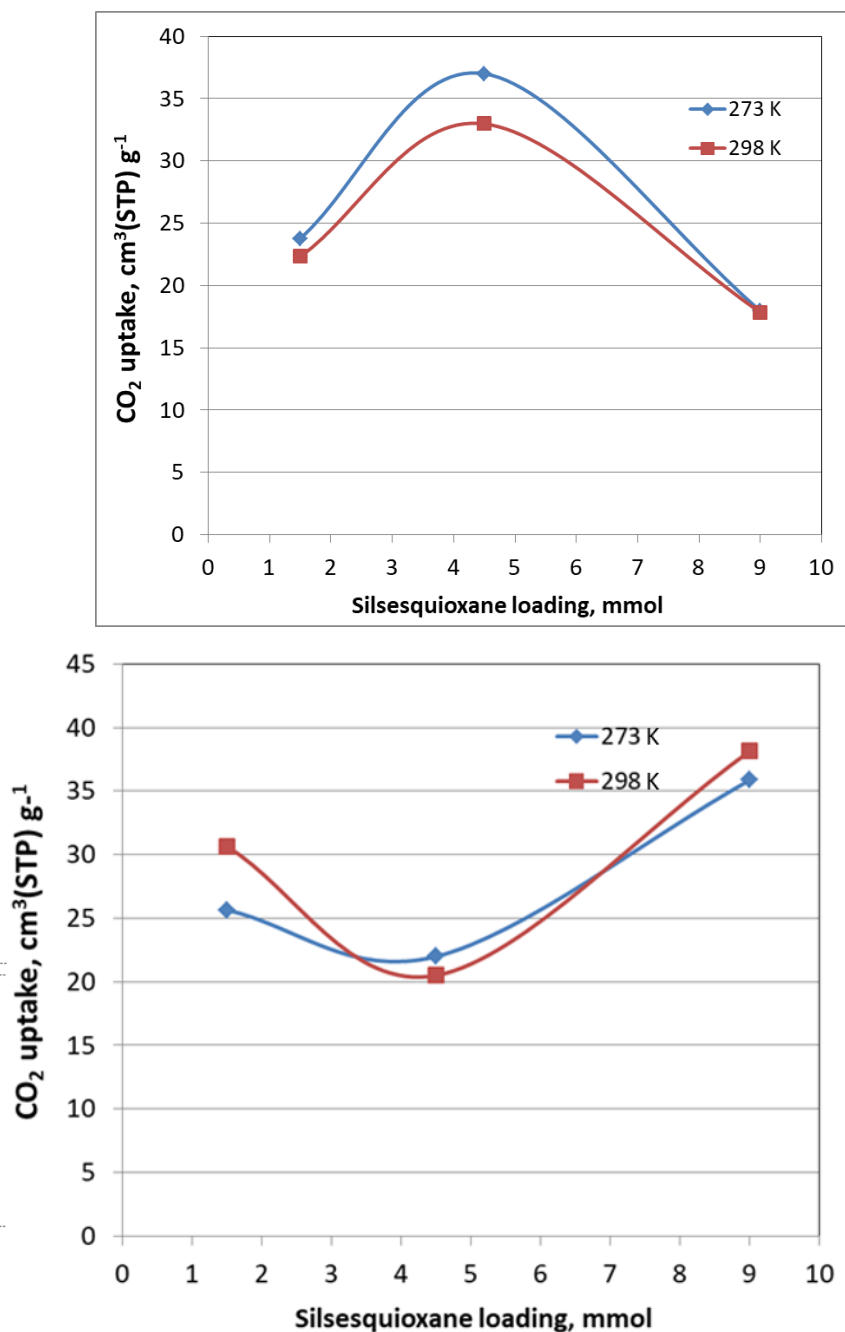


**Figure 4.10.** Gravimetric CO<sub>2</sub> uptake at 1 bar of the freeze-dried samples PILGD<sub>1.5</sub>FD, PILGD<sub>4.5</sub>FD and PILGD<sub>9</sub>FD as a function of silsesquioxane loading at the indicated temperatures (up) and the equivalent measurements for the air-dried samples (down)

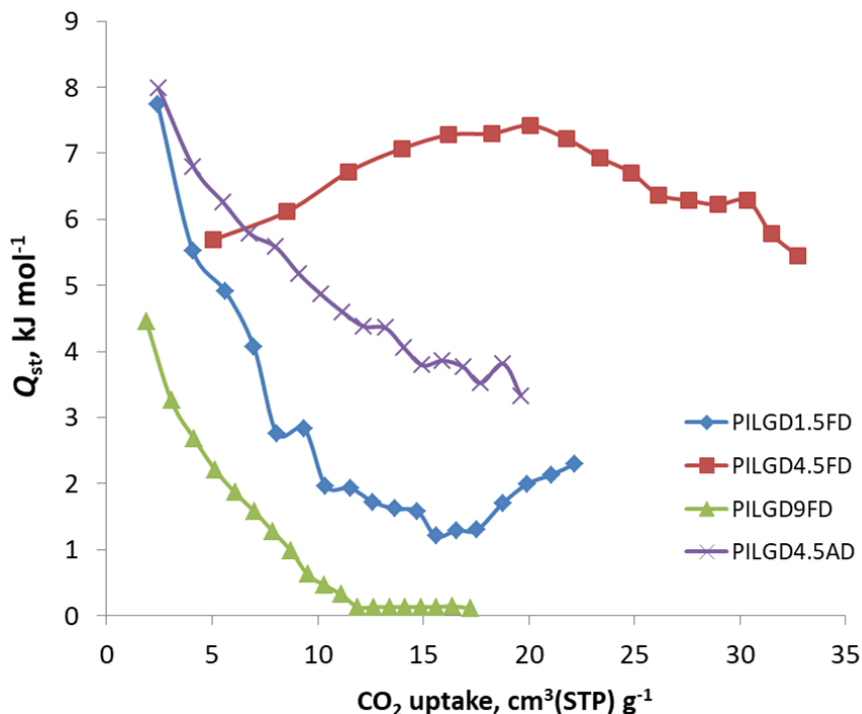


**Figure 4.11.** Isosteric heat of adsorption,  $Q_{st}$ , as a function of surface coverage, for the indicated solids

In contrast, the samples with lower and higher silsesquioxane content both show a rapid decrease of the  $Q_{st}$  values with increasing  $CO_2$  coverage, reaching 2.3 kJ/mol and 0.1 kJ/mol for PILGD<sub>1.5</sub>FD and PILGD<sub>9</sub>FD, respectively. Therefore, the average  $Q_{st}$  is significantly lower in both as compared to PILGD<sub>4.5</sub>FD, consistent with the higher  $CO_2$  uptake of the latter. Interestingly, the air-dried samples show a different  $CO_2$  adsorption behaviour, implying a different mechanism of  $CO_2$  sorption in these solids (see Figure 4.9). An uncommon result is that for PILGD<sub>1.5</sub>AD and PILGD<sub>9</sub>AD the  $CO_2$  uptake is higher at 298 K than at 273 K, suggesting that  $CO_2$  molecules have better access to the porous space in these solids when their kinetic energy is higher. This can be rationalized considering that these samples have a very compact structure as seen in the SEM images, and therefore a higher kinetic energy (higher temperature) is required for the  $CO_2$  molecules to be able to penetrate between the layers. The fact that PILGD<sub>4.5</sub>AD shows marginally higher  $CO_2$  uptake at 273 K compared to 298 K, could be associated with a less dense packing of the layers in this case, due to optimum silsesquioxane content. For

PILGD<sub>4.5</sub>AD, the calculated  $Q_{st}$  drops also fast as a function of surface coverage, reaching 3.3 kJ/mol at high CO<sub>2</sub> loading, consistent with the relatively low CO<sub>2</sub> uptake 22.0 cm<sup>3</sup>/g (0.98 mmol/g) at 273 K and 20.4 kJ/mol at 298 K.

#### 4.4. Conclusions

Diamino-functionalised silsesquioxane-pillared graphene oxide structures were synthesized with an easily upscalable protocol, by intercalating reactive silylating agents in the interlayer space between the carbon sheets. We showed that by simply opting for freeze-drying, the preferred drying technique in biology as well as in the pharmaceutical and food industries, the porosity can be significantly enhanced as compared to air-drying. The morphology change induced by freeze-drying can lead to an enhanced CO<sub>2</sub> adsorption capacity depending on the loading of the pillaring agent. The CO<sub>2</sub> storage capacity of the pillared structures that were developed is relatively high despite their low specific surface area – in general considered one of the key characteristics a highly efficient sorbent material. The pillared structure can compete easily with the performance at ambient conditions of other graphene-based materials possessing much higher specific surface areas ranging from 500 to 1000 m<sup>2</sup>/g.<sup>39</sup>

## References

1. M. Bui, C. S. Adjiman, A. Bardow, E. J. Anthony, A. Boston, S. Brown, P. S. Fennell, S. Fuss, A. Galindo, L. A. Hackett, J. P. Hallett, H. J. Herzog, G. Jackson, J. Kemper, S. Krevor, G. C. Maitland, M. Matuszewski, I. S. Metcalfe, C. Petit, G. Puxty, J. Reimer, D. M. Reiner, E. S. Rubin, S. A. Scott, N. Shah, B. Smit, J. P. M. Trusler, P. Webley, J. Wilcox and N. Mac Dowell, *Energy & Environmental Science*, 2018, **11**, 1062-1176.
2. A. M. Varghese and G. N. Karanikolos, *International Journal of Greenhouse Gas Control*, 2020, **96**, 103005.
3. X. Shi, H. Xiao, H. Azarabadi, J. Song, X. Wu, X. Chen and K. S. Lackner, *Angewandte Chemie International Edition*, 2020, **59**, 6984-7006.
4. S. Gupta and N.-H. Tai, *Journal of Materials Chemistry A*, 2016, **4**, 1550-1565.
5. A. M. Varghese, K. S. K. Reddy, S. Singh and G. N. Karanikolos, *Chemical Engineering Journal*, 2020, **386**, 124022.
6. W. Zhang, Y. Bao and A. Bao, *Journal of Environmental Chemical Engineering*, 2020, **8**, 103732.
7. Y. Wang, X. Hu, J. Hao, R. Ma, Q. Guo, H. Gao and H. Bai, *Industrial & Engineering Chemistry Research*, 2019, **58**, 13390-13400.
8. J. Shi, N. Yan, H. Cui, Y. Liu and Y. Weng, *Journal of Environmental Chemical Engineering*, 2017, **5**, 4605-4611.
9. Y. Liu, M. Xiang and L. Hong, *RSC Advances*, 2017, **7**, 6467-6473.
10. Y. Yang, K. Chiang and N. Burke, *Catalysis Today*, 2011, **178**, 197-205.
11. C. Li, J. Yang, L. Zhang, S. Li, Y. Yuan, X. Xiao, X. Fan and C. Song, *Environmental Chemistry Letters*, 2021, **19**, 1457-1475.
12. A. Peigney, C. Laurent, E. Flahaut, R. R. Bacsa and A. Rousset, *Carbon*, 2001, **39**, 507-514.
13. P. Cool and E. F. Vansant, in *Synthesis*, Springer Berlin Heidelberg, Berlin, Heidelberg, 1998, DOI: 10.1007/3-540-69615-6\_9, pp. 265-288.
14. A.-E. Stamate, O. D. Pavel, R. Zavoianu and I.-C. Marcu, *Catalysts*, 2020, **10**, 57.
15. G. K. Dimitrakakis, E. Tyljanakis and G. E. Froudakis, *Nano Letters*, 2008, **8**, 3166-3170.

16. K. Spyrou, D. Gournis and P. Rudolf, *Ecs Journal of Solid State Science and Technology*, 2013, **2**, M3160-M3169.
17. M. Dincă and J. R. Long, *Angewandte Chemie International Edition*, 2008, **47**, 6766-6779.
18. C. X. Zhang, F. Babonneau, C. Bonhomme, R. M. Laine, C. L. Soles, H. A. Hristov and A. F. Yee, *Journal of the American Chemical Society*, 1998, **120**, 8380-8391.
19. R. Tamaki, Y. Tanaka, M. Z. Asuncion, J. W. Choi and R. M. Laine, *Journal of the American Chemical Society*, 2001, **123**, 12416-12417.
20. L. M. Johnson and T. J. Pinnavaia, *Langmuir*, 1991, **7**, 2636-2641.
21. G. Fetter, D. Tichit, P. Massiani, R. Dutartre and F. Figueras, *Clays and Clay Minerals*, 1994, **42**, 161-169.
22. D. Petridis, D. Gournis and M. A. Karakassides, *Molecular Crystals and Liquid Crystals Science and Technology Section A: Molecular Crystals and Liquid Crystals*, 1998, **311**, 345-350.
23. A. Szabo, D. Gournis, M. A. Karakassides and D. Petridis, *Chemistry of Materials*, 1998, **10**, 639-645.
24. G. Balomenou, P. Stathi, A. Enotiadis, D. Gournis and Y. Deligiannakis, *Journal of Colloid and Interface Science*, 2008, **325**, 74-83.
25. J. Roziere, D. J. Jones and T. Cassagneau, *Journal of Materials Chemistry*, 1991, **1**, 1081-1082.
26. L. Staudenmaier, *Berichte der deutschen chemischen Gesellschaft*, 1898, **31**, 1481-1487.
27. R. Y. N. Gengler, A. Veligura, A. Enotiadis, E. K. Diamanti, D. Gournis, C. Jozsa, B. J. van Wees and P. Rudolf, *Small*, 2010, **6**, 35-39.
28. K. Spyrou, M. Calvaresi, E. A. K. Diamanti, T. Tsoufis, D. Gournis, P. Rudolf and F. Zerbetto, *Advanced Functional Materials*, 2015, **25**, 263-269.
29. T. Cassagneau, D. J. Jones and J. Roziere, *Journal of Physical Chemistry*, 1993, **97**, 8678-8680.
30. A. B. Bourlinos, D. Gournis, D. Petridis, T. Szabo, A. Szeri and I. Dekany, *Langmuir*, 2003, **19**, 6050-6055.
31. C. Nethravathi, B. Viswanath, C. Shivakumara, N. Mahadevaiah and M. Rajamathi, *Carbon*, 2008, **46**, 1773-1781.
32. G. Potsi, A. K. Ladavos, D. Petrakis, A. P. Douvalis, Y. Sanakis, M. S. Katsiotis, G. Papavassiliou, S. Alhassan, D. Gournis and P. Rudolf, *Journal of Colloid and Interface Science*, 2018, **510**, 395-406.

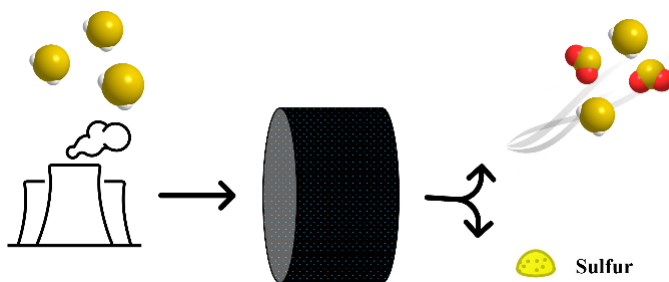
33. I. Dekany, R. Kruger-Grasser and A. Weiss, *Colloid and Polymer Science*, 1998, **276**, 570-576.
34. V. Țucureanu, A. Matei and A. M. Avram, *Critical Reviews in Analytical Chemistry*, 2016, **46**, 502-520.
35. A. Enotiadis, K. Angjeli, N. Baldino, I. Nicotera and D. Gournis, *Small*, 2012, **8**, 3338-3349.
36. R. Peña-Alonso, F. Rubio, J. Rubio and J. L. Oteo, *Journal of Materials Science*, 2007, **42**, 595-603.
37. S. Naviroj, S. R. Culler, J. L. Koenig and H. Ishida, *Journal of Colloid and Interface Science*, 1984, **97**, 308-317.
38. I. Spanopoulos, I. Bratsos, C. Tampaxis, D. Vourloumis, E. Klontzas, G. E. Froudakis, G. Charalambopoulou, T. A. Steriotis and P. N. Trikalitis, *Chem Commun (Camb)*, 2016, **52**, 10559-10562.
39. R. Ahmed, G. Liu, B. Yousaf, Q. Abbas, H. Ullah and M. U. Ali, *Journal of Cleaner Production*, 2020, **242**, 118409.





## Chapter 5: H<sub>2</sub>S removal by copper enriched and porous carbon cuboids

Hydrogen sulfide (H<sub>2</sub>S) removal by adsorption from gas streams is crucial to prevent the environmental and industrial damage it causes. Among the nanostructures considered excellent candidates as sorbents, porous carbon has been studied extensively over the last years. In this chapter we present a synthetic procedure for three high potential sorbents, namely a low-surface-area copper-rich structure, a highly porous carbon form without metal addition, and lastly the same porous carbon decorated with copper. The properties and performance as catalysts of these three sorbents were evaluated by powder X-ray diffraction, X-ray photoelectron spectroscopy, thermal analysis, scanning electron microscopy with energy dispersive X-ray analysis, surface area determination through N<sub>2</sub> adsorption and desorption, as well as by H<sub>2</sub>S adsorption measurements.



---

*The results of this Chapter have been submitted for publication as:*

*H<sub>2</sub>S removal by copper enriched porous carbon cuboids, E. Thomou, G. Basina, K. Spyrou, Y. Al Wahedi, P. Rudolf and D. Gournis*

## 5.1. Introduction

Hydrogen sulfide ( $H_2S$ ), is a hazardous, colourless, flammable gas, with a ‘rotten egg’ odour, that can be encountered either in the natural environment of gas/crude oil wells and hot springs, or as a by-product of industrial activities.<sup>1</sup> It has lethal effects on humans and animals and at the same time is the cause for extreme corrosion in industrial facilities.<sup>2</sup> A lot of effort has been put into developing technologies that can effectively remove  $H_2S$  and mitigate its negative effects; most of them fall under the following categories: absorption, adsorption, conversion, catalytic reactions, chemical oxidation, chemical scrubbing, incineration, and biological treatment.<sup>1-4</sup>

Adsorption is the most widely applied approach due to the good balance between cost and effectiveness,<sup>1</sup> and among the types of sorbents that have been studied for capturing  $H_2S$  (activated carbons, zeolites, polymers, metal oxides, *etc.*)<sup>5</sup>, porous carbons are particularly attractive due to their surface chemistry and large surface areas.<sup>3, 6, 7</sup> Furthermore, it has been proven that the desulfurization performance can be further improved when combining a porous matrix, that acts as support, with metal oxides.<sup>8-11</sup>

Inspiration for the work presented in this chapter came from a recently reported new member of the carbon family that combines porosity with the capability to accept functional groups on its surface, and has shown excellent performance in the capture of atmospheric water vapour.<sup>12</sup> This novel nanostructure is called porous carbon cuboids (PCCs) and combines a series of intriguing properties, such as light weight, unusual ultra-hydrophilic behaviour, great stability, surface heterogeneity, and a very high hierarchical porosity (estimated approximately 800-900  $m^2/gr$ ).<sup>12</sup> In contrast with graphene, which has to be subjected to oxidation in order to make it easily processible in solution, PCCs are highly hydrophilic as synthesized, because of the high number of functional groups on the surface. PCCs show a significant number of N:C and O:C active sites (Figure 5.1), which, in combination with the narrow micropore size distribution, constitute a very promising sorbent. Additionally they have the advantage of being functional up to 400 °C, making their use possible in higher temperature applications. The specific geometrical characteristics, hierarchical porosity, and surface chemistry identify PCCs as perfect hosts for metallic nanoparticles (NPs) that are homogeneously

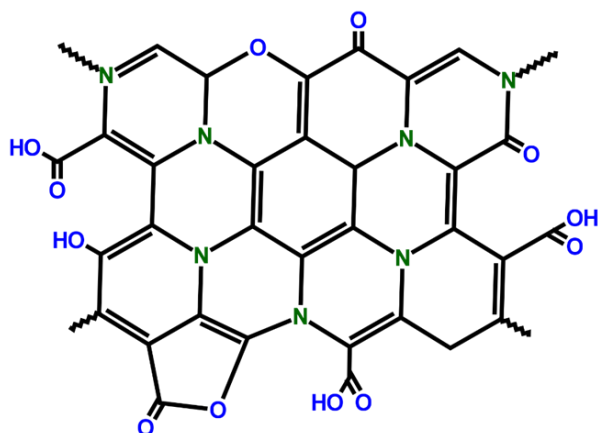


**Figure 5.1.** Structural Representation of Carbon Cuboids<sup>15</sup>

distributed on their surface as well as inside their pores. Immobilizing metal cations *via* functional groups avoids aggregation, which would compromise the outstanding properties of such nanoparticles.<sup>13, 14</sup> In fact, encapsulation of Cu and Ag NPs on the PCC scaffolds has already been confirmed as yielding promising antibacterial agents.<sup>15</sup>

To explore how the high surface area and the presence of copper oxide can be balanced and how they synergistically affect hydrogen sulfide removal, in the study reported in this chapter three different carbon nanostructures were synthesized and their performance evaluated with a H<sub>2</sub>S chemisorption experiment at 150 °C. Powder X-ray diffraction (XRD), X-ray photoelectron spectroscopy, thermal analysis, scanning electron microscopy (SEM) with energy dispersive X-ray analysis (EDX), as well as surface area determination through N<sub>2</sub> adsorption and desorption were used to characterize the novel sorbents.

## 5.2. Materials and methods

### 5.2.1. Materials

4,4' bipyridine (98%) was purchased from Alfa Aesar, ethanol (absolute, 99.9 %) was obtained by J.T. Baker, and Pluronic F127 and copper chloride dihydrate ( $\geq 99$  %) CuCl<sub>2</sub>·2H<sub>2</sub>O were acquired from Sigma-Aldrich. All reagents were of analytical grade and used without further purification. The water used in the experiments was distilled and deionized.

## 5.2.2. Materials synthesis

### 5.2.2.1. PCC synthesis

Two solutions were prepared. The first one consisted of 1 g of pluronic dissolved in 100 mL of 0.1 M 4,4'-bipyridine in water-ethanol (volume ratio of 1:17) and the second one was an aqueous solution of copper (II) chloride (900 mL, 5.6 mM  $\text{CuCl}_2 \cdot 2\text{H}_2\text{O}$ ). The first solution was then poured rapidly into the second one under vigorous stirring. The formed products were retrieved through centrifugation, washed three times with water, and air dried. The turquoise-coloured product was then pyrolyzed under argon flow (500 °C for 2 h, heating rate 1 °C/min) and the copper species were leached away (stirred in a 4M  $\text{HNO}_3$  aqueous solution for 24 h). The final black powder was washed with water until the pH value reached ~5.0 and air dried. This sample was denoted as *PCC*.<sup>12</sup> The intermediate product before the leaching step was denoted as *PCC-unleached*.

### 5.2.2.2. PCC-Cu synthesis

Metal-substituted porous carbon materials were synthesized using Cu. PCCs were dissolved in a metal salt aqueous solution (approximately 10 % w/w). The mixture was stirred for 1 h and then centrifuged. The precipitate was dissolved again in a new solution (1 h stirring), and the material was centrifuged again, washed with water, and air-dried. This sample is denoted as *PCC-Cu*.

### 5.2.3. H<sub>2</sub>S adsorption experiments

Hydrogen sulfide adsorption experiments were performed at atmospheric pressure in a fixed-bed U-shaped quartz reactor with 4 mm internal diameter. After sieving to sizes ranging between 125 µm and 250 µm, 200 mg of quartz particles were used to dilute 10 mg of the adsorbent and the mixture was transferred to the reactor, where it was sandwiched between two layers of quartz wool. After pre-treating the bed at 150 °C overnight using a stream of ultra-pure Ar (flow rate: 44 mL/min, 5.0 purity) to remove all water and residues, a feed gas comprised of 100 ppm  $\text{H}_2\text{S}$  in  $\text{N}_2$  having a flow rate of 40.5 mL/min was introduced (the setup for  $\text{H}_2\text{S}$  adsorption is shown in Figure 5.2). Effluents of the bed were analysed using a PerkinElmer Clarus 580 gas chromatograph equipped with Model Arnel 4025 PPC and Model Arnel 4016 PPC sulfur chemiluminescence

detector (see Figure 5.3). After breakthrough took place, the GC argon gas was passed through the system to flush out any remaining  $\text{H}_2\text{S}$ .



**Figure 5.2.**  $\text{H}_2\text{S}$  adsorption setup

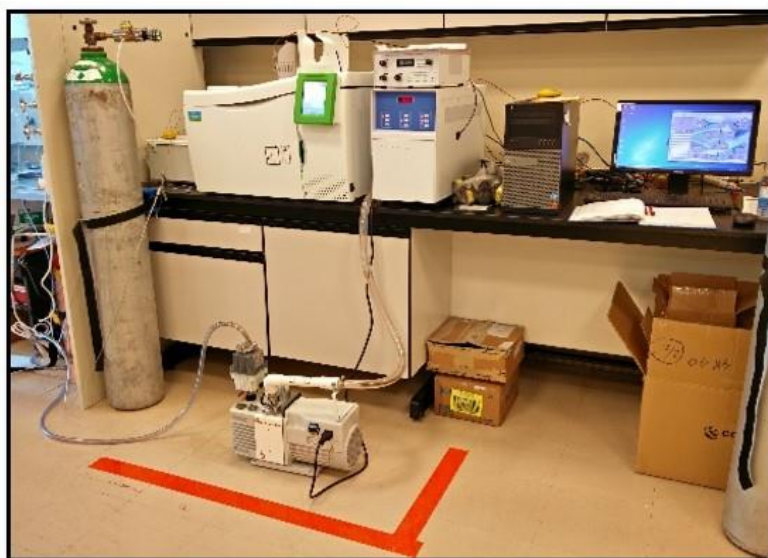


**Figure 5.3.** Gas chromatograph equipped with a sulfur chemiluminescence detector

### *Sulfur capacity determination*<sup>16, 17</sup>

The breakthrough time was determined as the time when the total concentration of sulfur gases ( $H_2S+SO_2$ ) at the outlet exceeded 5 ppm (and the experiment was stopped at 100 ppm of  $H_2S$  at the outlet).<sup>8</sup> The sulfur capacity (mmol/g) was calculated from the Equation (1), defined as the total  $H_2S$  moles adsorbed per mass of sorbent.

$$\text{Sulfur capacity} \left( \frac{\text{mmol}}{\text{g}} \right) = \frac{\text{Total moles adsorbed of } H_2S}{\text{Mass of sorbent (g)}} \times 10^{-3} \quad (1)$$

The total moles of  $H_2S$  adsorbed was estimated taking into consideration the amount of  $H_2S$  (mol/s) passing through the reactor and the breakthrough time as:

$$\text{Total moles adsorbed of } H_2S \text{ (mol)} \equiv \int_0^{t_{bt}} (\dot{n}_{in} - \dot{n}_{out}) dt \quad (2)$$

$$\dot{n} = \frac{xP\dot{V}}{RT} \quad (3)$$

where  $\dot{n}_{in}$  is  $H_2S$  molar rate in the bed effluent (mol/s),  $t_{bt}$  is the breakthrough time,  $x$  is  $H_2S$  mole fraction either in the feed gas or in the bed effluent,  $\dot{V}$  is the feed gas volumetric flow rate at standard conditions (L/s),  $P$  is Pressure (kPa),  $R$  universal gas constant ( $L \cdot kPa \cdot K^{-1} \cdot mol^{-1}$ ) and  $T$  is the temperature (K).

The sorbent utilization can be calculated as follows:

$$\text{Utilization} = \frac{\text{Sulfur capacity}}{12.571 \cdot Y_{CuO}} \quad (4)$$

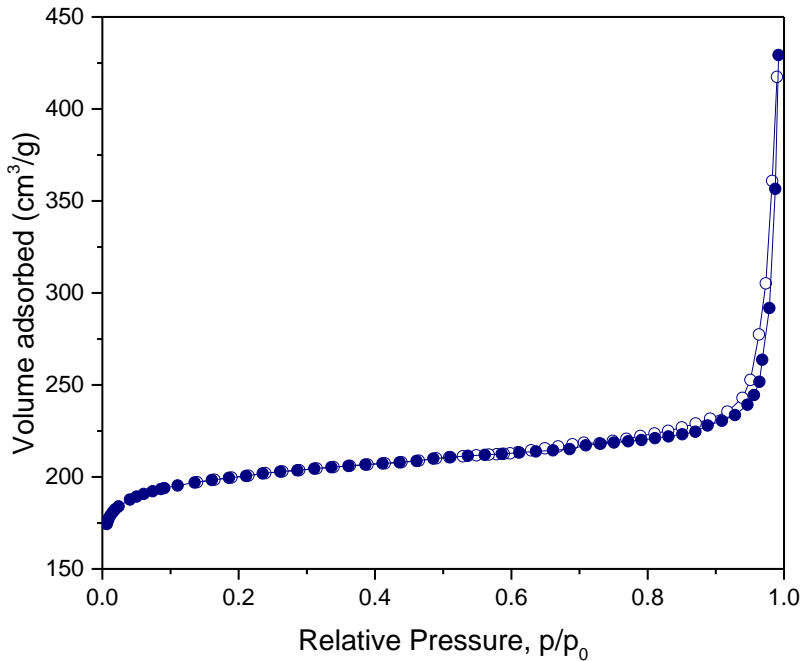
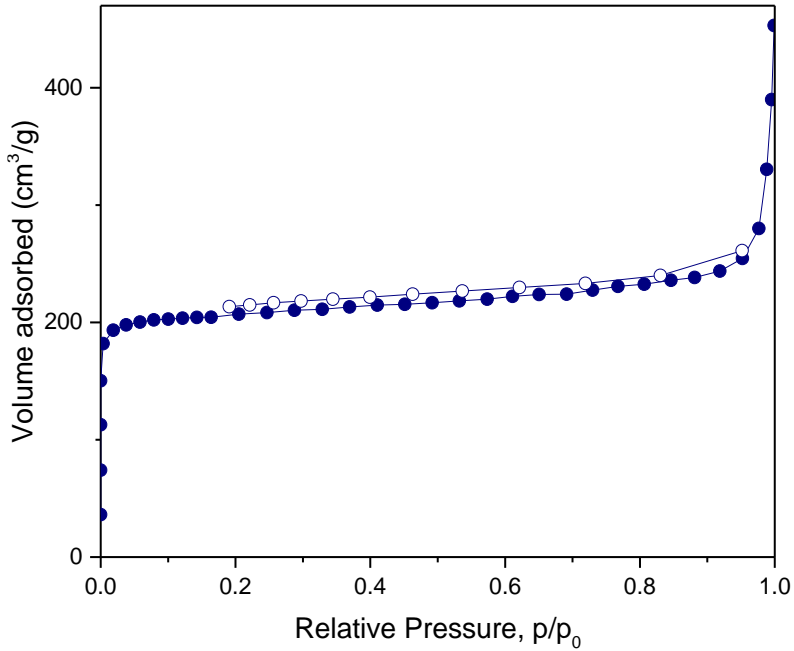
where: 12.571 is the maximum theoretical capacity of CuO in mmols of  $H_2S$  per gram CuO,  $Y_{CuO}$  is the mass fraction of CuO in the sample. The experiments were performed by Dr. Georgia Basina (Khalifa University, United Arab Emirates).

## **5.3. Results and discussion**

### **5.3.1. Structural and morphological characterization of the sorbents**

In order to verify that the synthesis of the porous carbon cuboids was successful and their properties the same as reported in literature<sup>12</sup>, we applied a series of characterization techniques as detailed in the following.

The pore characteristics of PCC, PCC-Cu, and PCC-unleached were investigated by nitrogen adsorption and desorption analysis. The corresponding isotherms are presented in Figure 5.4.



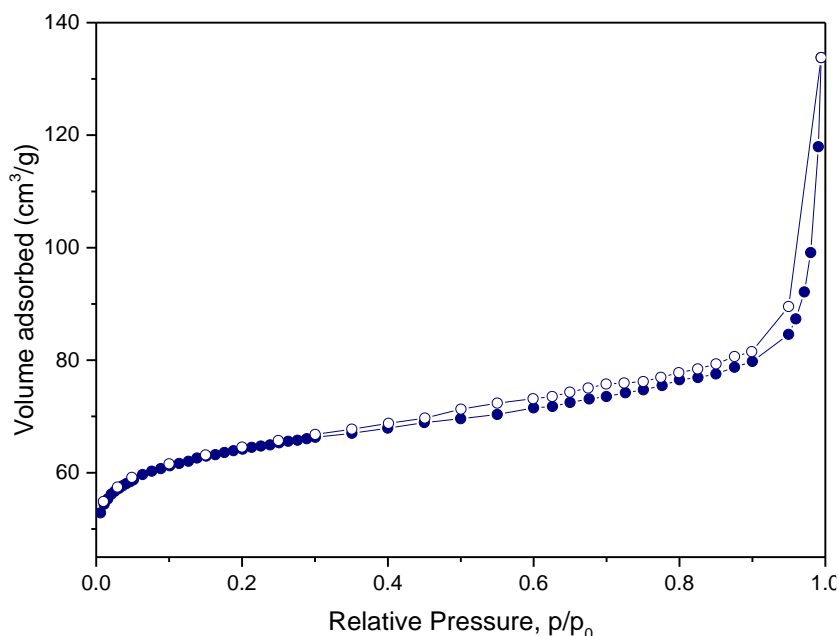
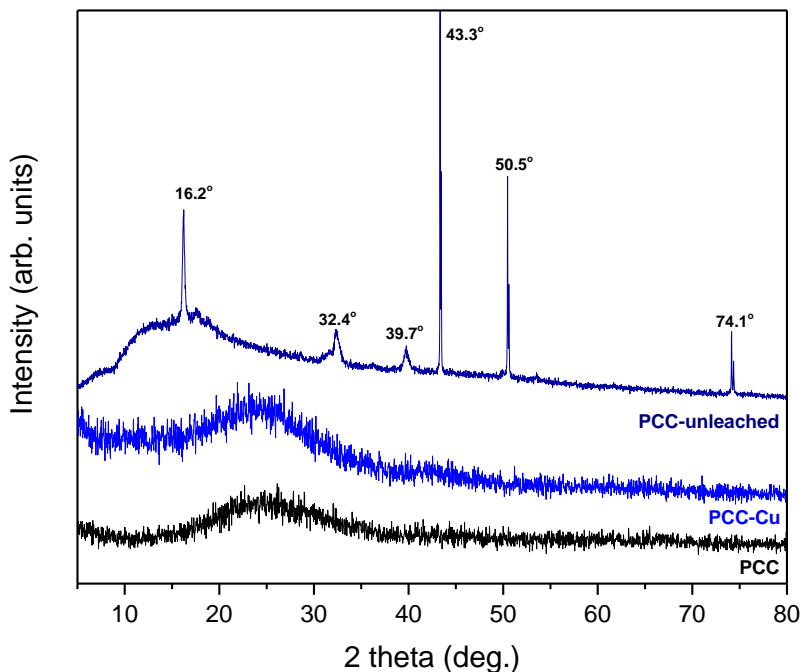


**Figure 5.4.** Nitrogen isotherms of PCC (top panel), PCC-Cu (middle panel) and PCC-unleached (bottom panel)

Analysing these isotherms with Brunner-Emmett-Teller theory, we found that the PCC shows a high apparent surface area of  $\sim 824 \text{ m}^2/\text{g}$ , which is in agreement with the first carbon cuboids reported<sup>12</sup> and with our earlier batches.<sup>15, 18</sup> After the addition of copper the apparent surface area of PCC-Cu is slightly lower than that of the pristine compound ( $\text{BET}_{\text{SA}} \sim 790 \text{ m}^2/\text{g}$ ). As expected, due to the high copper amount present in PCC-unleached the porosity is significantly lower with an apparent surface area of  $245 \text{ m}^2/\text{g}$ .

X-ray diffraction patterns of all three samples are shown in Figure 5.5. The patterns for PCC and PCC-Cu are similar, both exhibiting only one broad peak at  $\sim 25^\circ$  that is characteristic of an amorphous structure. The absence of sharp peaks in the case of PCC-Cu is attributed to the good distribution of the copper species as well as the fact that the broad carbon peak is superimposed to and probably covering the copper peaks. On the contrary, in the XRD pattern of the PCC-unleached six peaks appear at  $16.2^\circ$ ,  $32.4^\circ$ ,  $39.7^\circ$ ,  $43.3^\circ$ ,  $50.5^\circ$  and  $74.1^\circ$ , which, considering their FWHM (full width at half maximum) and shape, can be divided into groups that correspond to different crystal structures containing copper.

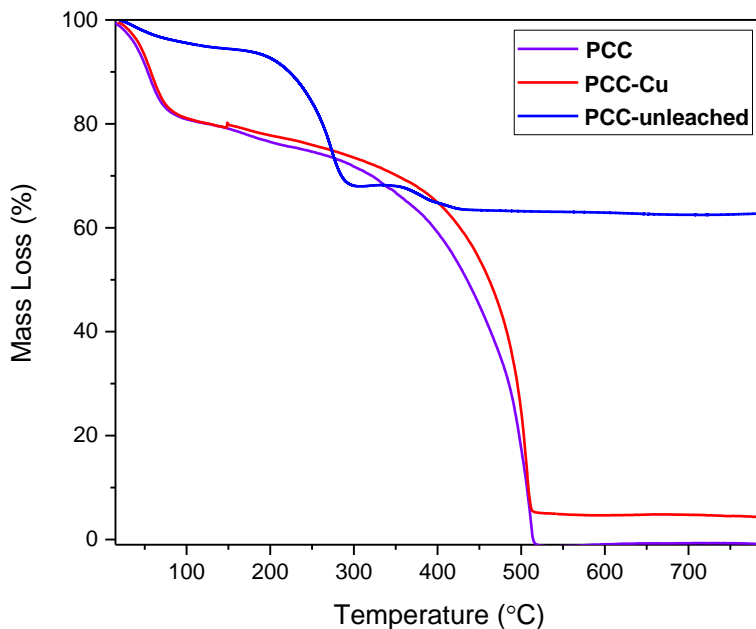




**Figure 5.5.** XRD patterns of the three carbon structures

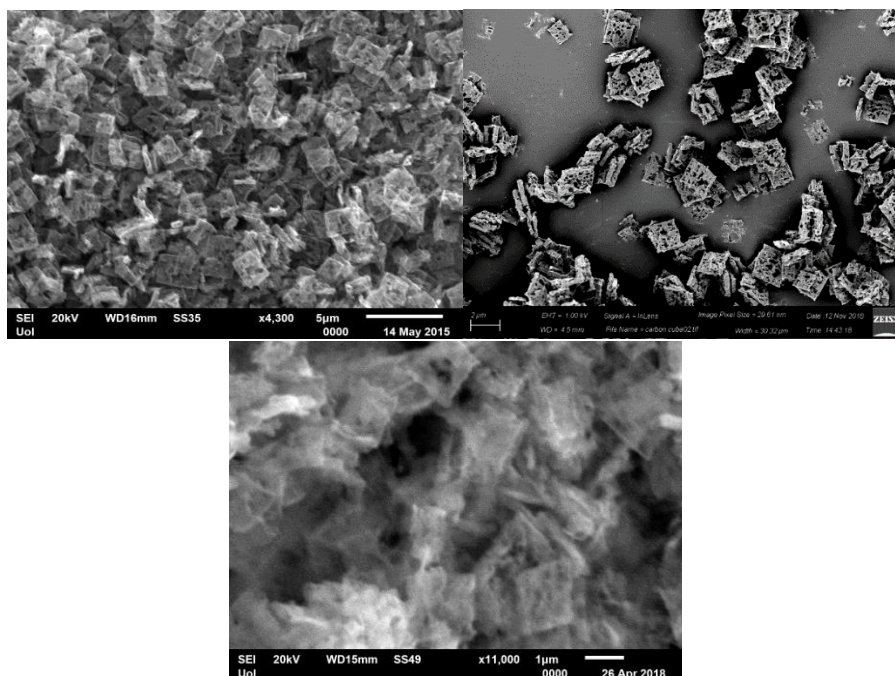
Three phases were identified: metallic Cu (sharp double peaks at  $43.3^\circ$ ,  $50.5^\circ$  and  $74.1^\circ$ )<sup>19</sup>, CuO ( $32.4^\circ$  and  $39.7^\circ$ )<sup>19</sup> and  $\text{CuCl}_2 \cdot 2\text{H}_2\text{O}$  ( $16.2^\circ$ , JCPDS no. 33-0451).

Thermogravimetric (TG) analysis was performed on pure carbon cuboids as shown in Figure 5.6. The TG curve testifies to the total absence of copper traces (within the detection limit) after the synthetic preparation of PCC. From the TG curves of PCC-Cu and PCC unleached, we calculated that the metal NPs embedded in the final nanostructure make up 4.5 wt.% of PCC-Cu, while for PCC unleached the metal remaining at the end of the heat treatment corresponds to 65 wt.%



**Figure 5.6.** Thermogravimetric (TG) analyses of PCC, PCC-Cu and PCC-unleached

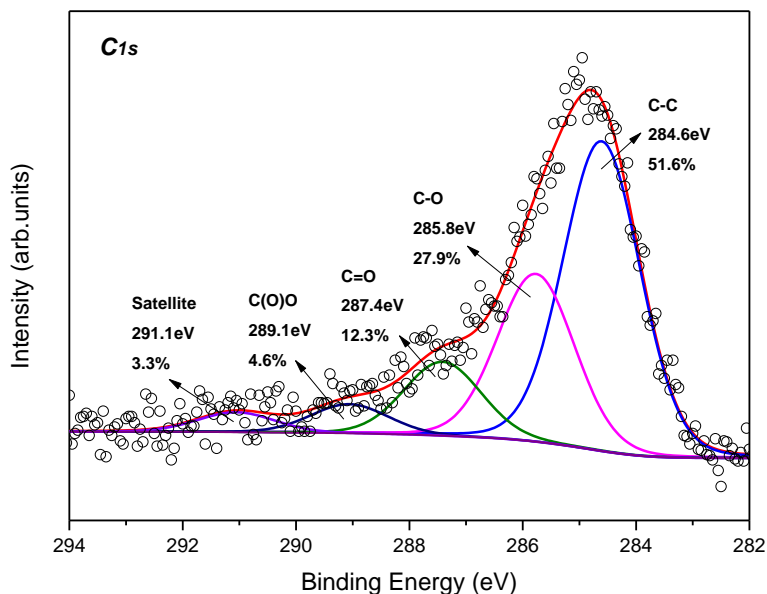
The morphology of the samples was characterized with SEM. The image in Figure 5.7(top left) shows the typical cubic structure of the PCCs, where randomly aggregated particles overlap with each other. One also notices that the surfaces of the particles are not smooth but show many macroporous holes, analogously to what has been observed in previous reports.<sup>12, 15</sup> As seen in Figure 5.7(top right), this distinctive shape of the nanomaterial is already formed before the leaching step, with the only difference being that much of the mass of PCC-unleached is made up by copper. For PCC-Cu, whose image is presented in Figure 5.7 – bottom, the morphology remained almost unaffected by the metal substitution.



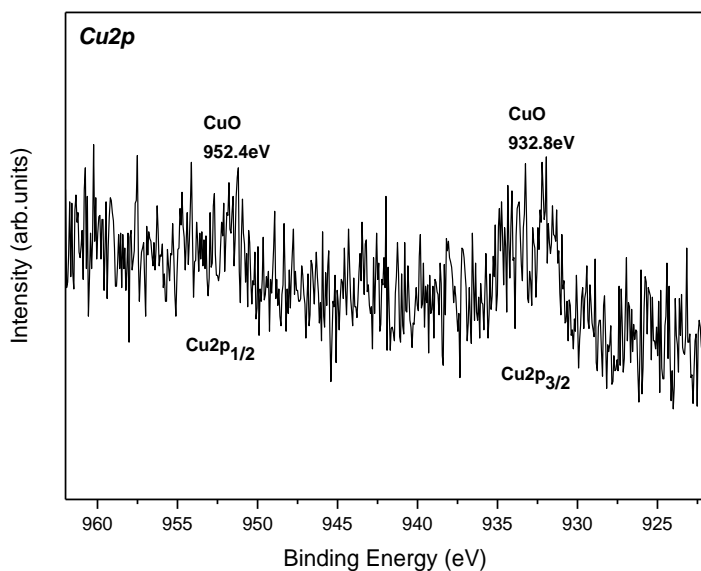
**Figure 5.7.** Scanning electron microscopy images of PCC (top left), PCC-unleached (top right) and PCC-Cu (bottom)

X-ray photoelectron spectroscopy (XPS) was applied to gain insight in the elemental composition, and chemical environment of the elements. Figure 5.8 shows the XPS spectrum of the C1s core level region of PCC; five contributions are necessary to obtain a good fit. The intense peak at a binding energy (BE) of 284.6 eV is due to C–C bonds and accounts for 51.6 % of the total C1s spectral intensity, whereas the contribution at 285.8 eV is attributed to C–O and C–N moieties, which represent 27.9 % of the total amount of carbon. The peaks at BEs of 287.4 and 289.1 eV are attributed to carbon double bond oxygen and carboxylic groups, respectively. Finally, the fifth peak, located at 291.1 eV, is a shake-up satellite, characteristic of the aromatic structures.<sup>20</sup>

In the case of PCC-Cu, the decoration with copper was confirmed by the detection of a Cu2p core level photoemission signal (see Figure 5.9). Unfortunately, the amount of copper is so small that the low intensity of the signal does not allow to extract more information than that the copper is in the form of oxides.

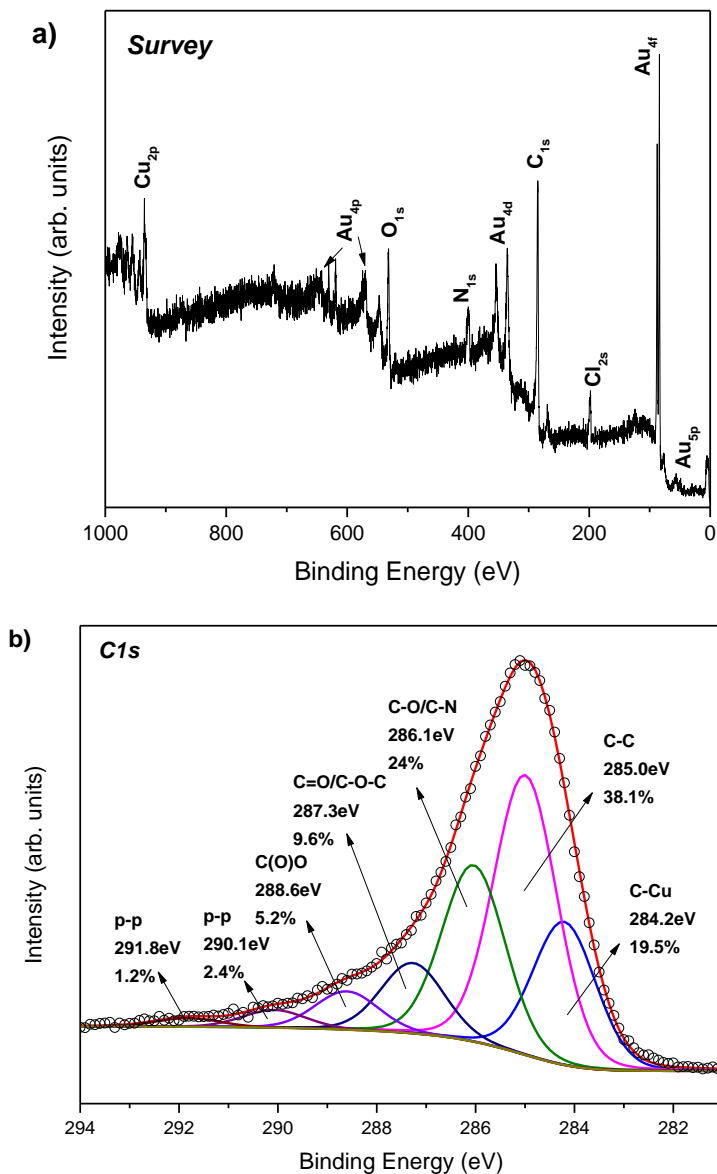


**Figure 5.8.** XPS spectrum of the C1s core level region of PCC. The fit is also shown and for each component the relative contribution to the total C1s spectral intensity is indicated.



**Figure 5.9.** XPS spectrum of the Cu2p core level region of PCC-Cu

Moving to the PCC-unleached, in the survey scan of PCC-unleached which is presented in Figure 5.10(a), we find the signature of expected elements, namely carbon, oxygen, nitrogen, chlorine and copper, and by analysing the detailed spectra of the various core level regions we can calculate the atomic composition as C 44.1 at%, O 32.4 at%, N 11.8 at%, Cl 7.5 at% and Cu 4.1 at%. The large Au4*f* signature and the other Au peaks arise from the Au/mica substrate on which the sample was deposited.



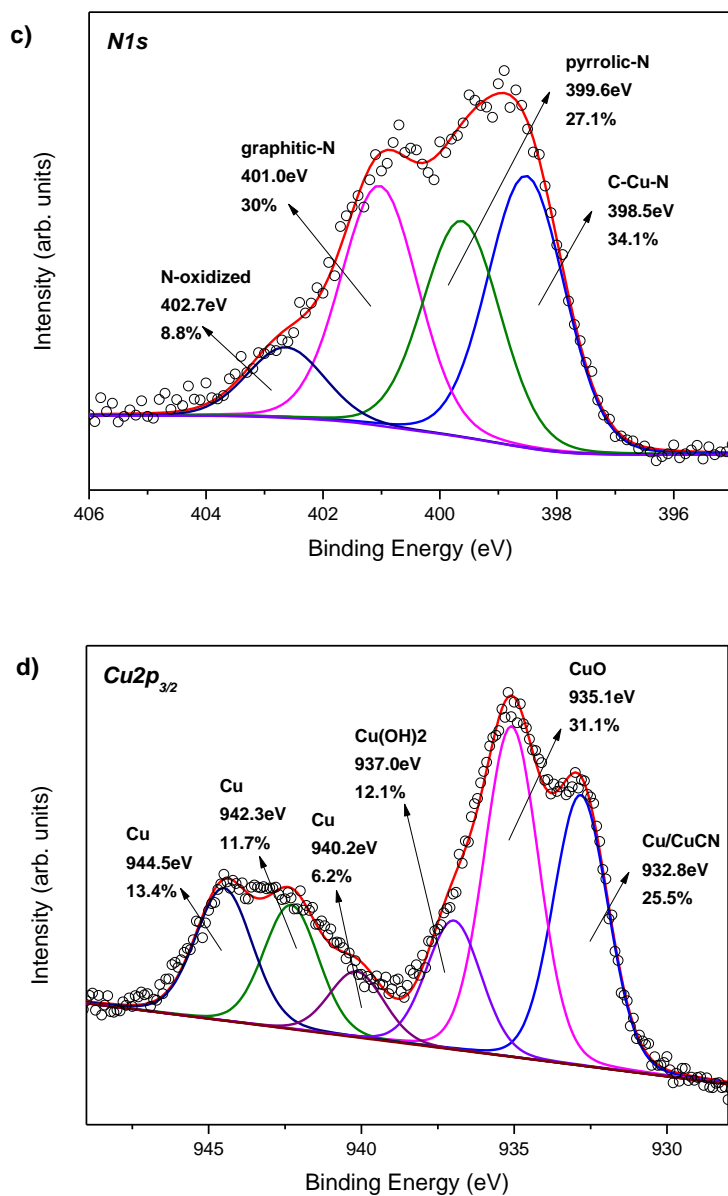


**Figure 5.10.** XPS spectra of PCC-unleached: (a) survey scan, detailed spectra of the (b) C1s, (c) N1s and (d) Cu2p core level regions. For the detailed spectra the fit is also shown and for each component the relative contribution to the total spectral intensity of the respective line is indicated.

The XPS spectrum of the C1s core level region, shown in Figure 5.10(b), requires seven contributions to obtain a good fit. The first peak at a BE of 284.2 eV derives from C-Cu bonds, the most intense peak at 285.0 eV is due to the C-C bond, whereas the one at 286.1 eV is attributed to the C-O and C-N bonds.<sup>20</sup> The peaks at 287.3 and 288.6 eV arise from the C=O/C-O-C and C(O)O bonds respectively, and the two peaks at 290.1 and 291.8 eV are shake-up satellite peaks due to final states where  $\pi$ - $\pi^*$  transitions of the aromatic rings occurred in the photoemission process together with the emission of the photoelectrons.

Figure 5.10(c) presents the spectrum of the N1s core level region, where four contributions can be identified; C-Cu-N bonds give rise to the peak at a BE of 398.5 eV,<sup>21</sup> pyrrolic-N is responsible for the contribution at 399.6 eV, while the signals at BEs of 401.0 and 402.7 eV are due to graphitic-N and N-oxidized, respectively.

Finally, in the XPS spectrum of the Cu2p<sub>3/2</sub> core level region in Figure 5.10(d), the peak at a BE of 932.8 eV is attributed to metallic copper as well as to Cu-C-N bonds,<sup>21</sup> the one at 935.1 eV is due to the CuO, and the one at 937.0 eV derives from the Cu(OH)<sub>2</sub>. Lastly, the contributions at BEs above 940.0 eV represent satellite features of copper<sup>2+</sup>.

The XPS spectra of PCC-unleached just discussed clearly support the existence of the coordination network connecting carbon, copper, and nitrogen atoms, at the basis of the formation of the carbon cuboids.

### 5.3.2. H<sub>2</sub>S removal study

Having studied the characteristics and properties of the synthesized materials, we proceeded to investigate the potential of these compounds for H<sub>2</sub>S removal with the experimental procedure explained in Section 5.2.3.

The breakthrough curves were collected for each sample at 150 °C and are depicted in Figure 5.11; a summary of the experimental values is presented in Table 5.1. We noted that H<sub>2</sub>S and SO<sub>2</sub> evolution start concurrently. The breakthrough time, BT, was calculated as the time when the total concentration of the two sulfur-containing gases exceeds 5 ppm at the outlet; the BT and the calculated H<sub>2</sub>S capacity at 5 % for each of the samples are shown in Table 5.1.

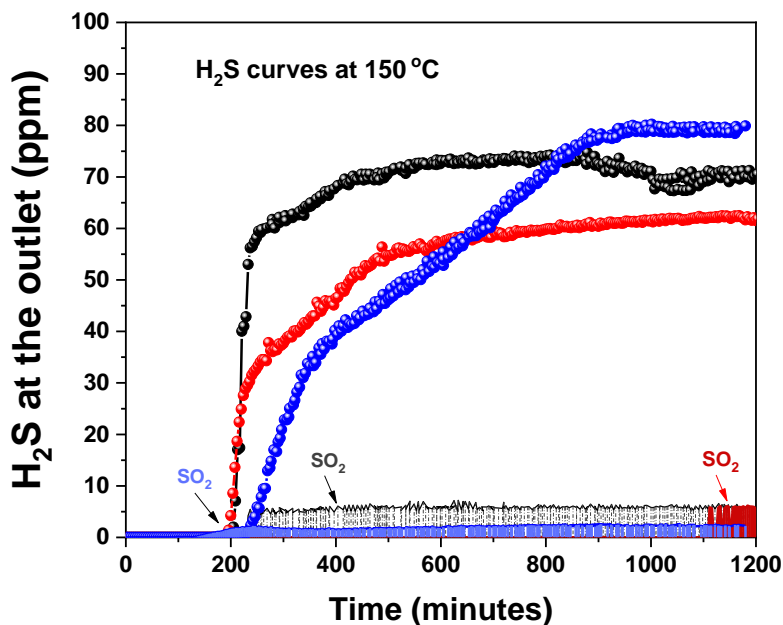


**Figure 5.11.** Breakthrough curves of H<sub>2</sub>S over PCC-unleached (blue) PCC (red) and PCC-Cu (black) after sulfidation at 150 °C. The SO<sub>2</sub> evolution for each sorbent is noted as well

**Table 5.1.** Experimental values from the sulfidation process

Parameter	PCC	PCC-Cu	PCC-unleached
BT (min)	202	207	247
Qv (ml/min)	40.42	40.01	40.24
Mass of Adsorbent (g)	0.01	0.01	0.01
H <sub>2</sub> S(ppm)	100	100	100
Molar Flow H <sub>2</sub> S (mols/s)	$2.75 \times 10^{-9}$	$2.72 \times 10^{-9}$	$2.73 \times 10^{-9}$
Total mols Adsorbed	$3.33 \times 10^{-5}$	$3.38 \times 10^{-5}$	$4.07 \times 10^{-5}$
Capacity in mmol/g	3.332	3.347	4.069



Conducting the sulfidation experiments on porous (PCC & PCC-Cu) and copper rich (PCC-unleached) materials, the expected behaviour is that of sorbents. When a sample acts as a sorbent, the recorded curve reaches at a certain point the 100 ppm, which marks the point where the material starts to saturate and stops to adsorb. On the other hand, in the case of a perfect catalyst there would be no breakthrough and all of the gas would be transformed into elemental sulfur.

Figure 5.12 shows a photograph of the reactor right after the experiment. It is easily discernible that a significant amount of elemental sulfur is concentrated on the walls of the reactor between the sample and the exit.

This indicates that sulfur is produced during the reaction and that the three carbon powders do not act only as sorbents but also as catalysts. As reported in Table 5.1, the sorption capability of all three compounds is significant: PCC and PCC-Cu both capture 3.3 mmol/g of hydrogen sulfide, and PCC-unleached 4.1 mmol/g (using a steady flow of  $\text{H}_2\text{S}$  the amount of moles adsorbed are recorded and the capacity is calculated as explained in Section 5.2.3).

For PCC and PCC-Cu, which both show a similar behaviour, the performance is credited to the porous matrix, since in the first one there is no copper content and in the latter one the amount of Cu is calculated to be below 5 wt.%. A factor that might contribute to the good adsorptive behaviour is the presence of nitrogen heteroatoms in the structure, which has been proven to give enhancing characteristics to adsorbents.<sup>1</sup>



**Figure 5.12.** Photograph of the reactor after the  $\text{H}_2\text{S}$  adsorption experiments: elemental sulfur is visible on the right near the exit

The accumulation of sulfur on all three porous carbon cuboids also decreases the active surface for adsorption and catalysis. With the evolution of the experiment, from a certain time onwards, H<sub>2</sub>S can therefore no longer be totally adsorbed/consumed and this leads to saturation.<sup>22</sup>

One notes that in none of the cases the Breakthrough curves are completely smooth, with the phenomenon being most evident in the case of PCC-Cu (Figure 5.11(c)), where bursts with an oscillating behaviour are seen. The reason for this behaviour is not clear but relevant literature reports that this behaviour is observed whenever elemental sulfur is produced and accumulated on the catalyst, and cannot be removed from the reactor.<sup>23</sup>

PCC-unleached was investigated a bit further because it has the highest sorption capacity despite its lower porosity, and presents a catalytic activity caused by the presence of copper in various chemical environments.

It is clear that at least two reactions take place; as a first step, hydrogen sulfide is adsorbed onto the carbon matrix, and secondly selective oxidation of the gas occurs and produces CuS and sulfur.

As mentioned in Section 5.3.1, copper in PCC-unleached is present in different forms: Cu-C-N bonds, metallic Cu, CuO and CuCl<sub>2</sub>·2H<sub>2</sub>O. After the H<sub>2</sub>S experiment, the structure of the adsorbent-catalyst was again assessed via X-Ray Diffraction and the data are shown in Figure 5.13 together with those of the initial PCC-unleached sample (remeasured right before the sulfidation process for better comparison).

After the sulfidation experiment, the powder XRD pattern displays all the characteristic peaks of CuS (JCPDS card number of Covellite 06-0464, shown in Figure 5.13 for comparison). This means that before the breakthrough time, when the adsorption is taking place, CuO is converted to CuS concurrently. Secondary reactions start to take place after the first three hours have passed, and as can be easily seen in Figure 5.11(a), SO<sub>2</sub> starts to be emitted. The concentration is low and SO<sub>2</sub> can be considered a by-product of the reactions that take place.

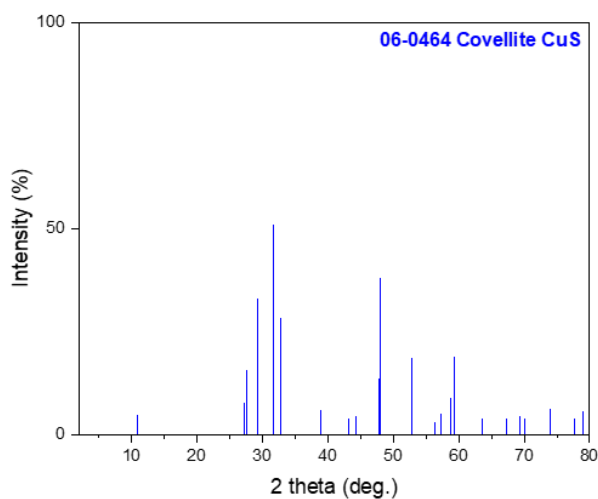
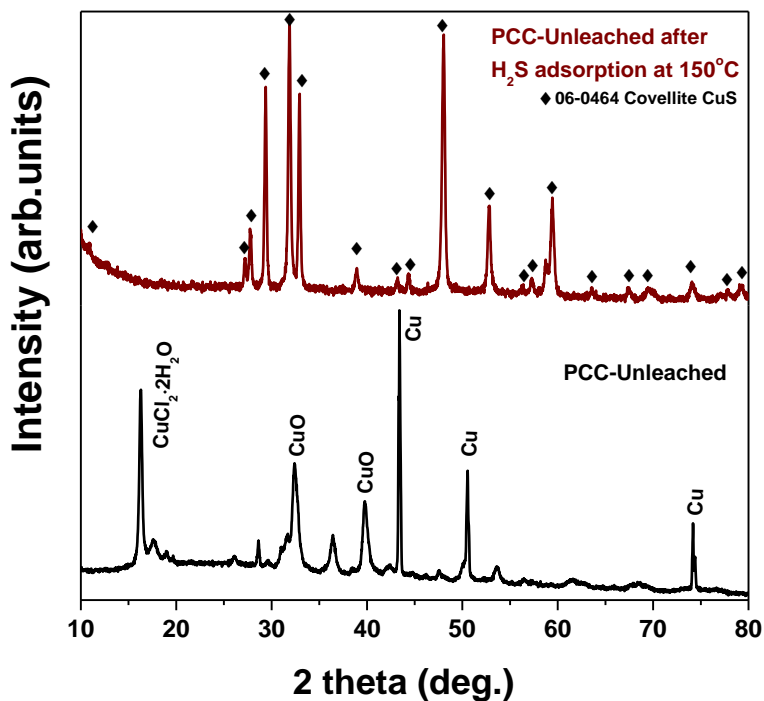


**Figure 5.13.** Powder XRD patterns of the PCC-unleached sample, before and after sulfidation at 150 °C. The XRD pattern of CuS (JCPDS card number of Covellite 06-0464), is shown for comparison.

To learn whether these chemical reactions changed the morphological characteristics of PCC-unleached, we collected SEM also after the

sulfidation experiment. As seen in Figure 5.14 no changes in the morphology of the sample can be identified (compare to Figure 5.7-top right panel). The EDX results and the elemental mapping (Table 5.2 and Figure 5.14 respectively) confirm that a large amount of sulfur is present and well distributed all over the sample and the mass. The SEM elemental mapping and analysis of the PCC-unleached sample before the sulfidation are shown for comparison in Figure 5.14(top panel), and in Table 5.2, respectively.

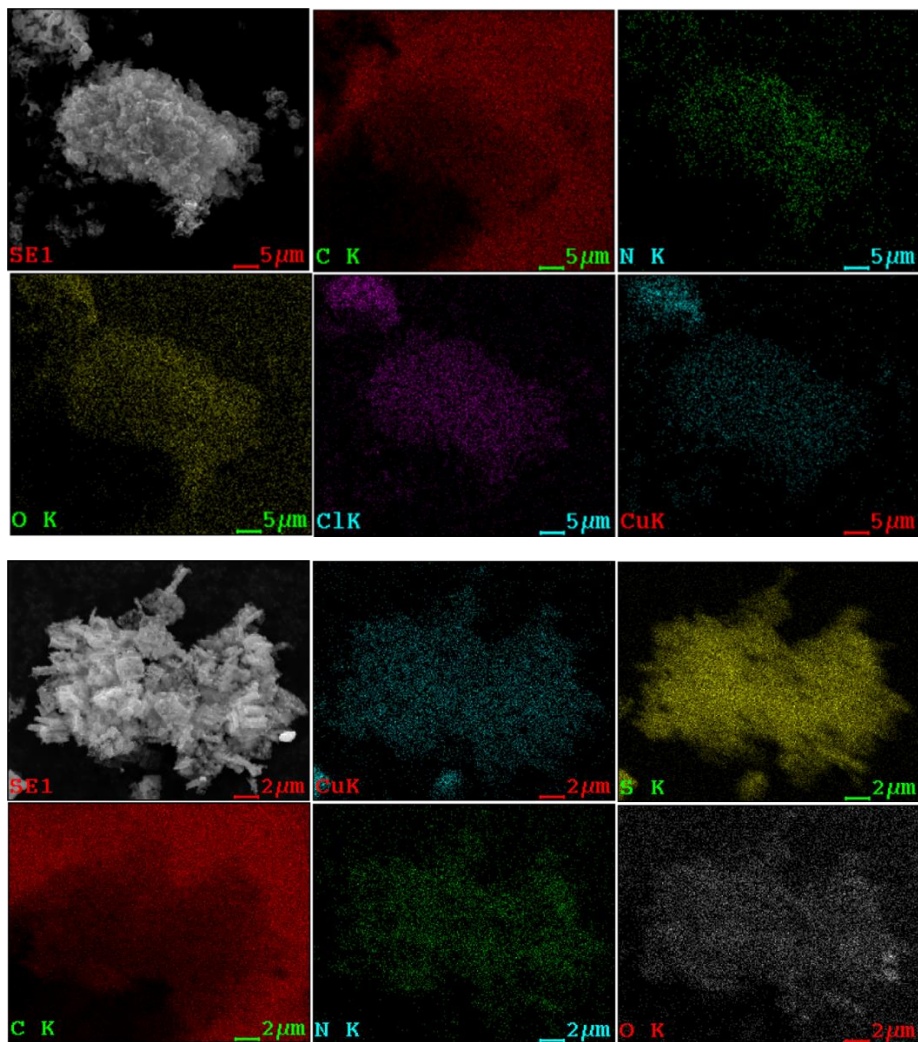


**Figure 5.14.** SEM and elemental mapping of the PCC-unleached before (top) and after (bottom) sulfidation

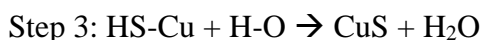
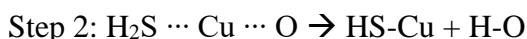
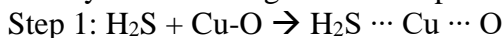
**Table 5.2.** EDX analysis of PCC-unleached before and after sulfidation

Element	Before		After	
	wt %	at %	wt %	at %
C	39.5	61.8	33.1	57.0
N	6.9	9.3	5.7	8.4
O	11.7	13.9	6.6	8.6
S	-	-	25.5	16.5
Cu	31.5	9.4	29.1	9.5
Cl	10.4	5.6	-	-

From the EDX analysis we calculated that the ratio of copper to sulfur atoms in the sample after sulfidation is almost 1:2, which justifies the presence of CuS as well as the emission of SO<sub>2</sub> and the production of elemental sulfur.

### 5.3.3. Possible reactions – proposed mechanism

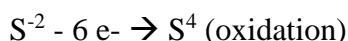
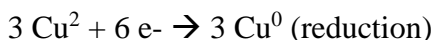
Based on experimental studies and theoretical calculations based on DFT,<sup>16, 24-27</sup> the reaction mechanism that leads to the conversion of H<sub>2</sub>S to CuS can be explained by the following reaction steps:



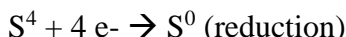
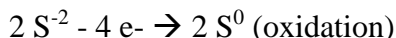
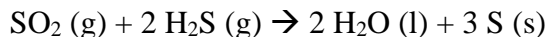
In parallel, a redox (oxidation-reduction) reaction like the one shown here could be taking place:



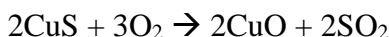
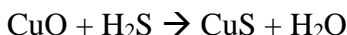
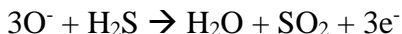
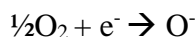
which would explain the emission of SO<sub>2</sub>. CuO is an oxidizing and H<sub>2</sub>S is a reducing agent:



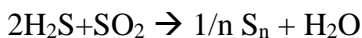
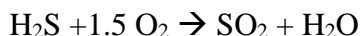
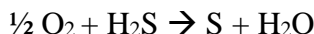
Sulfur dioxide could in turn react with hydrogen sulfide, to produce elemental sulfur through the following redox reaction ( $\text{H}_2\text{S}$  is a reducing agent,  $\text{SO}_2$  is an oxidizing agent):



In the case that a significant amount of oxygen was present during the experiment (possible leak or impurities in the  $\text{H}_2\text{S}$  gas from the provider), the reactions that take place when  $\text{CuO}$  is used for gas sensing applications<sup>28-30</sup> could also happen:



It has been proven that the presence of oxygen during hydrogen sulfide capture leads to the formation of elemental sulfur and sulfur dioxide, which can be enhanced by the presence of water and can improve the adsorption process especially in sorbents that contain copper.<sup>7, 31, 32</sup>



Hydrogen sulfide is partially oxidized to sulfur, and as the oxidation proceeds sulfur dioxide is also emitted, which is then consumed again by reacting with the gas to produce more sulfur.<sup>33</sup>

Finally, other copper species ( $\text{Cu}_2\text{O}$ ,  $\text{Cu}(\text{OH})_2$ ) present on the surface although not detected by XRD, might also have an important role and even be responsible for the sulfur production through their involvement in the reactions taking place.

## 5.4. Conclusions

Three porous carbon cuboids with different characteristics were synthesized through carbonization of the product of a coordination reaction and their potential as H<sub>2</sub>S sorbents was evaluated. The sorbents with the higher porosity showed lower sorption capacity and were also catalytically active. The copper-rich sample with the lowest surface area was proved to also function as a catalyst, with selective oxidation of hydrogen sulfide taking place. The latter was investigated a bit further and ideas about the potential mechanism behind the catalytic activity were put forward. Further improvement of the designed materials could lead in high performance catalysts suitable for H<sub>2</sub>S conversion.

## References

1. M. Khabazipour and M. Anbia, *Industrial & Engineering Chemistry Research*, 2019, **58**, 22133-22164.
2. A. D. Wiheeb, I. K. Shamsudin, M. A. Ahmad, M. N. Murat, J. Kim and M. R. Othman, *Reviews in Chemical Engineering*, 2013, **29**, 449-470.
3. A. G. Georgiadis, N. D. Charisiou and M. A. Goula, *Catalysts*, 2020, **10**, 521.
4. E. Üresin, H. İ. Saraç, A. Sarıoğlu, Ş. Ay and F. Akgün, *Process Safety and Environmental Protection*, 2015, **94**, 196-202.
5. M. S. Shah, M. Tsapatsis and J. I. Siepmann, *Chemical Reviews*, 2017, **117**, 9755-9803.
6. F. Rodríguez-Reinoso and A. Sepúlveda-Escribano, in *Handbook of Surfaces and Interfaces of Materials*, ed. H. S. Nalwa, Academic Press, Burlington, 2001, pp. 309-355.
7. H.-b. Fang, J.-t. Zhao, Y.-t. Fang, J.-j. Huang and Y. Wang, *Fuel*, 2013, **108**, 143-148.
8. B. Elyassi, Y. A. Wahedi, N. Rajabbeigi, P. Kumar, J. S. Jeong, X. Zhang, P. Kumar, V. V. Balasubramanian, M. S. Katsiotis, K. Andre Mkhoyan, N. Boukos, S. A. Hashimi and M. Tsapatsis, *Microporous and Mesoporous Materials*, 2014, **190**, 152-155.
9. L.-J. Wang, H.-L. Fan, J. Shangguan, E. Croiset, Z. Chen, H. Wang and J. Mi, *ACS Applied Materials & Interfaces*, 2014, **6**, 21167-21177.
10. O. Karvan and H. Atakül, *Fuel Processing Technology*, 2008, **89**, 908-915.
11. J. H. Yang, *Korean Journal of Chemical Engineering*, 2021, **38**, 674-691.
12. G.-P. Hao, G. Mondin, Z. Zheng, T. Biemelt, S. Klosz, R. Schubel, A. Eychmüller and S. Kaskel, *Angewandte Chemie International Edition*, 2015, **54**, 1941-1945.
13. J. Cui, Y. Yang, Y. Hu and F. Li, *J Colloid Interface Sci*, 2015, **455**, 117-124.
14. A. K. Karumuri, D. P. Oswal, H. A. Hostetler and S. M. Mukhopadhyay, *Nanotechnology*, 2016, **27**, 145603.
15. D. Karageorgou, E. Thomou, N. T. Vourvou, K.-M. Lyra, N. Chalmpes, A. Enotiadis, K. Spyrou, P. Katapodis, D. Gournis and H. Stamatis, *ACS Omega*, 2019, **4**, 4991-5001.
16. G. Basina, D. A. Gaber, S. A. Yafei, V. Tzitzios, S. A. Gaber, I. Ismail, B. V. Vaithilingam, K. Polychronopoulou, S. A. Hashimi



- and Y. A. Wahedi, *Chemical Engineering Journal*, 2020, **398**, 125585.
17. M. A. Haija, G. Basina, F. Banat and A. I. Ayes, *Materials Science-Poland*, 2019, **37**, 289-295.
  18. A. V. Chatzikonstantinou, E. Gkantzou, E. Thomou, N. Chalmpes, K.-M. Lyra, V. G. Kontogianni, K. Spyrou, M. Patila, D. Gournis and H. Stamatis, *Nanomaterials*, 2019, **9**, 1166.
  19. D. Collins, T. Luxton, N. Kumar, S. Shah, V. K. Walker and V. Shah, *PLOS ONE*, 2012, **7**, e42663.
  20. K. Spyrou, M. Calvaresi, E. A. K. Diamanti, T. Tsoufis, D. Gournis, P. Rudolf and F. Zerbetto, *Advanced Functional Materials*, 2015, **25**, 263-269.
  21. R. C. Dante, F. M. Sánchez-Arévalo, P. Chamorro-Posada, J. Vázquez-Cabo, L. Huerta, L. Lartundo-Rojas, J. Santoyo-Salazar, O. Solorza-Feria, A. Diaz-Barrios, T. Zoltan, F. Vargas, T. Valenzuela, F. Muñoz-Bisesti and F. J. Quiroz-Chávez, *Fullerenes, Nanotubes and Carbon Nanostructures*, 2016, **24**, 171-180.
  22. E. Laperdrix, G. Costentin, O. Saur, J. C. Lavalley, C. Nédéz, S. Savin-Poncet and J. Nougayrède, *Journal of Catalysis*, 2000, **189**, 63-69.
  23. O. N. Kovalenko, N. N. Kundo, V. M. Novopashina and V. M. Khanaev, *Reaction Kinetics and Catalysis Letters*, 1998, **64**, 129-137.
  24. Z. Li, N. Wang, Z. Lin, J. Wang, W. Liu, K. Sun, Y. Q. Fu and Z. Wang, *ACS Applied Materials & Interfaces*, 2016, **8**, 20962-20968.
  25. J. A. Rodriguez, T. Jirsak, M. Pérez, S. Chaturvedi, M. Kuhn, L. González and A. Maiti, *Journal of the American Chemical Society*, 2000, **122**, 12362-12370.
  26. F. Peng, Y. Sun, Y. Lu, W. Yu, M. Ge, J. Shi, R. Cong, J. Hao and N. Dai, *Nanomaterials*, 2020, **10**, 774.
  27. S. Yasyerli, G. Dogu, I. Ar and T. Dogu, *Industrial & Engineering Chemistry Research*, 2001, **40**, 5206-5214.
  28. G. E. Patil, D. D. Kajale, S. D. Shinde, V. G. Wagh, V. B. Gaikwad and G. H. Jain, in *Advancement in Sensing Technology: New Developments and Practical Applications*, eds. S. C. Mukhopadhyay, K. P. Jayasundera and A. Fuchs, Springer Berlin Heidelberg, Berlin, Heidelberg, 2013, DOI: 10.1007/978-3-642-32180-1\_17, pp. 299-311.
  29. S. Navale, M. Shahbaz, S. M. Majhi, A. Mirzaei, H. W. Kim and S. S. Kim, *Chemosensors*, 2021, **9**, 127.

30. Z. Huang, X. Wang, F. Sun, C. Fan, Y. Sun, F. Jia, G. Yin, T. Zhou and B. Liu, *Materials & Design*, 2021, **201**, 109507.
31. S. Cimino, L. Lisi, A. Erto, F. A. Deorsola, G. de Falco, F. Montagnaro and M. Balsamo, *Microporous and Mesoporous Materials*, 2020, **295**, 109949.
32. R. Sitthikhankaew, D. Chadwick, S. Assabumrungrat and N. Laosiripojana, *Fuel Processing Technology*, 2014, **124**, 249-257.
33. G. Basina, O. Elmutasim, D. A. Gaber, S. A. Gaber, X. Lu, V. Tzitzios, B. V. Vaithilingam, M. Baikousi, G. Asimakopoulos, M. A. Karakassides, I. Panagiotopoulos, K. Spyrou, E. Thomou, E. Sakellis, N. Boukos, D. Xu, M. Tsapatsis, N. A. Amoodi and Y. A. Wahedi, *Applied Catalysis B: Environmental*, 2020, **278**, 119338.

## **Chapter 6: Hierarchical porous carbon structures derived from sugar and coffee waste**

### **Abstract**

Hierarchical porous carbons were synthesized by incorporating sugar waste and spent coffee grounds in the materials used in the production process in an attempt to explore the potential waste reuse as part of the efforts towards a waste free society. Four different kinds of porous carbons were developed: for two of them molasses wastewater or sugar beet root extract waste was used in combination with silica as a composite starting material, one that was reinforced with spent coffee grounds in an attempt to introduce functional groups that could be beneficial for future applications, and in the fourth one two kinds of waste (molasses and spent coffee grounds) were combined. The properties and surface characteristics of the hierarchical porous carbons were studied with N<sub>2</sub> porosimetry and SEM measurements. Three samples were selected for CO<sub>2</sub> activation to maximize their specific surface area and introduce microporosity to their structures.

## 6.1. Introduction

The ever-increasing demands of modern society are energy and resources costly as well, apart from being highly challenging to sustain, and require the development of high-performance materials that can lead to breakthroughs and keep up with that pace. Porous carbons have been proven to be one of the greatest assets towards this effort as they can efficiently perform in a vast range of fields such as energy storage (Li-ion batteries, supercapacitors),<sup>1-5</sup> desalination,<sup>6</sup> environmental remediation (heavy metals, dyes),<sup>7-9</sup> catalysis (electrocatalysis, fuel cells),<sup>10-12</sup> as well as gas capture and storage (CO<sub>2</sub>, H<sub>2</sub>, CH<sub>4</sub>)<sup>13-15</sup>.

Hierarchical porous carbon (HPC) is one of the forms of porous carbon that has attracted great attention over the last few years because it has been proven to be highly efficient for a plethora of applications. Its major assets are the light weight, low cost, the possibility of physical and chemical manipulation,<sup>16</sup> and the well-defined maze-like network formed by the interconnected meso- and micropores along with the presence of the larger macropores. Another advantage resides in the controllability of pore size, which can be changed by simply modifying synthetic parameters like the size of the silica used as a template as described below, or the silica to glucose ratio. Through tuning of the pore size the accessibility of active sites distributed throughout the whole volume of the sorbent and at the surface can be improved.

HPCs can be prepared through (hard or/and soft) templating methods as well as through template-free synthetic pathways, or by combining templating and activation methods.<sup>17</sup> Activation can hugely boost the specific surface area of the material and consists in removing carbon atoms from the carbon solid to create extra pores by either exposing the solid to oxidative gases (CO<sub>2</sub>, O<sub>2</sub>, NH<sub>3</sub> and H<sub>2</sub>O steam<sup>18</sup>) at high temperatures or by pyrolysis when an activating agent (KOH,<sup>19, 20</sup> NaOH,<sup>20</sup> CaCl<sub>2</sub>,<sup>21</sup> ZnCl<sub>2</sub>,<sup>22</sup> K<sub>2</sub>C<sub>2</sub>O<sub>4</sub>)<sup>23</sup> is mixed with the sample.<sup>24</sup>

A major challenge in the greener, more sustainable, and environmentally friendlier production of carbons with high porosity is the integration of biomass and waste products in the production process. Apart from complying with the global efforts towards a waste free world, employing such products as precursors is also convenient because they are low cost, renewable and easily accessible. Thus far, numerous porous carbons that

originate from biomass including celtuce leaves, bamboo, olive stones, almond shells, sawdust, chitosan and coffee grounds have been reported in the literature.<sup>25</sup>

Coffee is probably the second most popular beverage after water, with millions of tons being produced and consumed globally per year, leading to excessive amounts of ground coffee waste. Composed of lignin, cellulose,<sup>26</sup> tannins, protein, caffeine, and phenols,<sup>27</sup> spent coffee grounds are a cheap and abundant precursor and has already been used for the development of porous carbons for use in applications like in batteries,<sup>28</sup> supercapacitors,<sup>29</sup> water purification,<sup>30</sup> as well as CO<sub>2</sub> adsorbents.<sup>31</sup>

The production of another popular product, sugar, yields waste streams with high organic load in the form of molasses wastewater, vinasses, root extract from sugar beet, *etc.* Molasses wastewater is mainly composed of carbohydrates, protein and cellulose, and highly demanding in oxygen, which renders it easily harmful for the environment.<sup>32</sup> Therefore the treatment of molasses wastewater,<sup>33</sup> or ways to reuse it are under continuous development; it has already successfully been used<sup>34</sup> as an acidifying agent.

In this chapter we report on the preparation of hierarchical porous carbons using spent coffee waste, as well as waste derived from the sugar industry. More specifically, the approach followed was based on the one introduced by Giannelis and collaborators in 2013,<sup>35</sup> where high performance hierarchical porous carbons are produced through the controlled combination of an ice template, a hard template and physical activation, as schematically illustrated in Figure 6.1. Macropores are created by means of a cryo-template applied to a matrix made of glucose and colloidal silica (hard template). Mesopores are successively introduced in the sample by subjecting it to carbonization and etching of the silica with NaOH. The meso/microporous carbon's porosity can be further improved by physical activation with CO<sub>2</sub> that can produce micropores and consequently a higher specific surface area. In our study, the glucose used in the original method was substituted by sugar containing waste, and the matrix was in some cases further reinforced/functionalized with coffee waste.

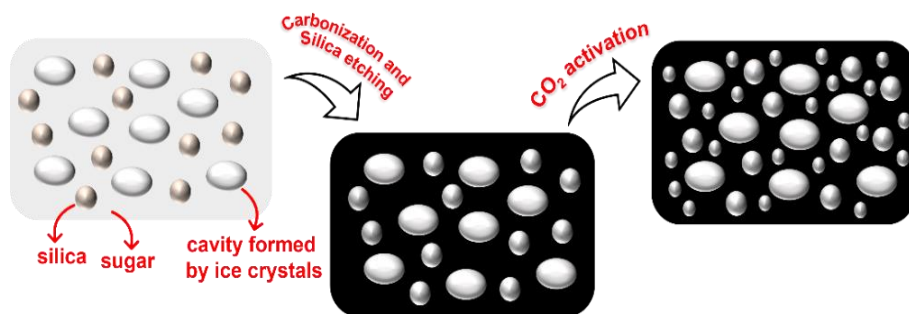


**Figure 6.1.** Schematic illustration of the synthetic procedure for hierarchical porous carbons

## 6.2. Materials and methods

### 6.2.1. Materials

12nm LUDOX colloidal silica HS-30 (30 wt.% suspension in water) was purchased from Sigma-Aldrich, sodium hydroxide (pellets for analysis), and sucrose (99 %) from Alfa Aesar. Concentrated liquid sugar beet root wastewater and molasses, a syrup obtained in the processing after the crystalized sugar is removed and which has a 47 % total sugar content according to ICUMSA GS4/3-9 analytical method, were provided by Cosun Beet Company (the Netherlands). Spent coffee grounds (from now on to referred as FC) was collected from a household filter coffee machine, dried prior to use in an oven at 80 °C for 24 h to remove any remaining humidity and ground with mortar and pestle. All chemical reagents were used as received without further purification and were of analytical grade. Distilled deionized water was used for all the experiments.

### 6.2.2. Materials synthesis

#### *HPC-FC*

The ratio of silica to sucrose/coffee was chosen to be 1:1. Consequently, three different HPCs were synthesized by keeping the amount of silica to 1.00 g and modifying the ratio of sucrose to coffee so that their total mass was always 1.00 g. The process was conducted for 0.20, 0.35 and 0.50 g of coffee. Sucrose was dissolved in 10 mL of H<sub>2</sub>O before adding FC and stirring for 10 minutes. Thereafter the mixture was added to the silica and stirred for half hour. The mixture was then transferred to two plastic falcon

tubes and submerged in liquid nitrogen for 15 minutes prior to placing them in a freeze dryer for ~ 3 days. The monoliths (Figure 6.2(c)) that were collected, were pyrolyzed at 800 °C for 3 h with a heating rate of 10 °C/min under argon flow. As seen on the photographs in Figure 6.2(e) and (f), the shape of the monoliths was maintained up to a high degree during pyrolysis. To enhance the effect of the etching procedure for removing the silica, the monoliths were all ground. A spherical flask was placed in an oil bath and ~1.0 g of HPC and 200 mL NaOH 3M were added and maintained at 80 °C at medium stirring overnight. While still warm, the mixture was filtered with a Gooch crucible (Por. 4, Pore-Diameter 10 - 16 µm) and washed repeatedly with lukewarm water till the pH value reached an almost neutral value. The filter was placed in a drying oven at 50 °C and left overnight; the powder was collected the next day and the etching procedure was repeated to remove any remaining silica and the sample was dried again at 50 °C.

### ***HPC-M***

Following a similar experimental path, the sucrose was substituted by molasses wastewater and the freeze-dried monoliths shown in Figure 6.2(d) were formed. Bearing in mind that the actual sugar content of the molasses wastewater was ~47 % w/w, two porous carbons were prepared with 1:1 and 2:1 ratio of silica to sugar, respectively. Molasses although it instantaneously dissolves in water, was stirred with 10 mL of H<sub>2</sub>O for 10 minutes prior to being added to the silica and stirred again for 15 minutes until a homogeneous mixture was achieved. The samples were frozen as above, and the same calcination and etching protocol was followed.

### ***HPC-M/FC***

The same procedure as in HPC-M was followed with the only difference that 1.0 g of filter coffee waste was added to the molasses aqueous solution and stirred for 10 minutes before adding it to the silica and moving on to the succeeding steps. The process was performed for both ratios. The corresponding freeze-dried monoliths are shown in Figure 6.2(b).

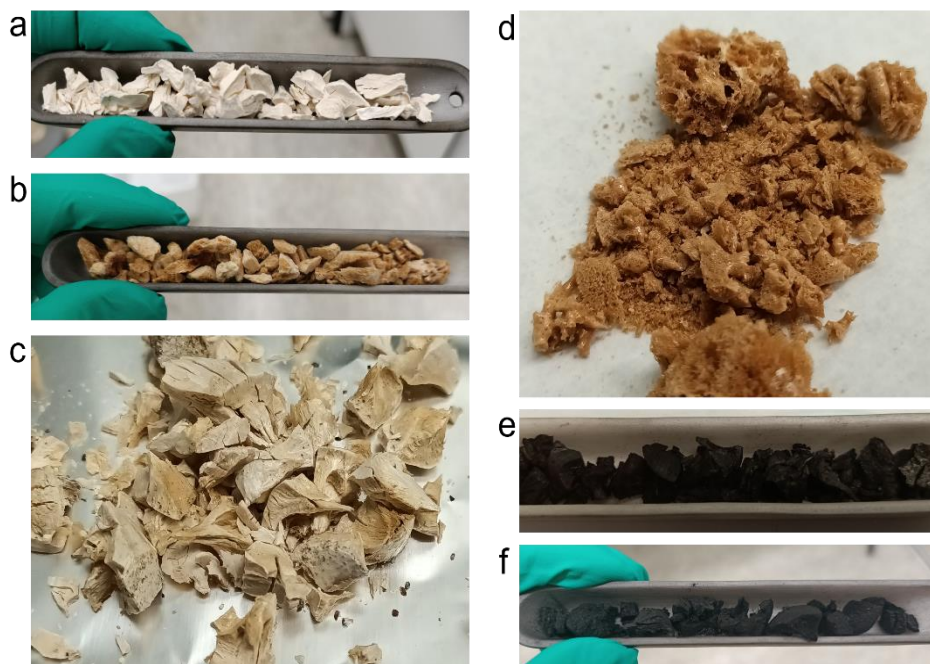


**Figure 6.2.** Optical images of the monoliths of hierarchical porous carbon produced after the freeze-drying procedure (a – HPC-B, b – HPC-M/FC, c – HPC-FC, d – HPC-M), as well as two examples of calcination products that showcase that the monolith form is preserved in the process (e-f)

### ***HPC-B***

Working in an analogous fashion, porous carbons were created from concentrated liquid sugar beet root extract. The percentage of sugar in this case was much lower (~10 % w/w) making it difficult to work with the above experimental volumes. For this reason, it was chosen that two samples would be synthesized where in 1.0 g of silica 10 and 20 mL of sugar beet root extract was added, respectively. After 15 minutes of stirring, the freezing, calcination, and etching procedures were followed as described above. The corresponding freeze-dried monoliths are shown in Figure 6.2(a).

### **6.2.3. CO<sub>2</sub> activation**

A partially home-made CVD system consisting in a quartz vacuum tube surrounded by a commercial heater (Carbolite) and connected to gas injection lines was used. The selected samples were placed in the quartz



tube, then first pumped to a base pressure of  $7 \times 10^{-4}$  mbar before being exposed to 0.2 mbar of Argon ( $\geq 99.9999\%$ , SOL Nederland B.V.) for 15 minutes to establish an inert environment, and thereafter heated up to  $800\text{ }^\circ\text{C}$  with a heating rate of  $10\text{ }^\circ\text{C}/\text{min}$ . When the target temperature was reached, the samples were exposed to 0.7 mbar of  $\text{CO}_2$  (99.995%, Sigma Aldrich) for 2 hours (the Argon flow was removed with the  $\text{CO}_2$  gas introduction). Afterwards, the  $\text{CO}_2$  flow was switched off and the samples were cooled down to room temperature in 0.2 mbar of Ar. The activated samples are identified by “Act” after the sample name in the following.

### 6.3. Results and Discussion

Porous structures were successfully synthesized making use of one single waste product derived from coffee or sugar or of a combination of two waste products. Before initiating the synthesis, a fast analysis of the waste products was performed in order to have an estimation of the composition so that the ratios would be kept almost identical with respect to the original protocol<sup>35</sup> upon which the project was based. For this reason, the soluble carbohydrates were analysed through anion exchange chromatography which was performed using a Dionex system. The molasses waste sample was estimated to contain sucrose, glucose, and fructose, in weight concentrations of respectively about 37.9, 0.14 and 0.20 %w/w. In the case of the sugar beet root extract, the dominant monosaccharide was arabinose with about 7 %w/w, followed by glucose and fructose with 1.27 and 0.46 %w/w, respectively. There were only negligible amounts of sucrose detected, which can only be considered as traces. Sucrose is a disaccharide made up of one molecule of glucose and one molecule of fructose joined together. The structures of all the monosaccharides present in the sugar beet root extract are shown in Figure 6.3.

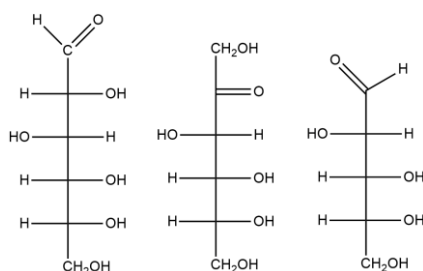


**Figure 6.3.** Two-dimensional depiction of glucose (left), fructose (middle) and arabinose (right)

The first set of samples was prepared by following the original protocol<sup>35</sup> and simply adding coffee waste in the mixture. Spent coffee grounds have been reported<sup>26</sup> to have a high sugar content on their own but since here we used them as ‘reinforcements’ to an already existing composite matrix made of sucrose and colloidal silica, we decided to not proceed with further analysis. The porosity of the carbons was evaluated through N<sub>2</sub> adsorption and desorption. The corresponding isotherms are presented in Figure 6.4; all samples show a characteristic hysteresis loop, which identifies them as type IV according to the IUPAC classification and is associated with capillary condensation taking place in mesopores. The hysteresis becomes less noticeable as the amount of coffee waste integrated increases, and the specific surface area decreases. The BET (Brunauer, Emmett and Teller) theory and BJH (Barrett-Joyner-Halenda) method<sup>36</sup> were used to evaluate the gas adsorption data and calculate the specific surface area, which ranged between 580 and 1009 m<sup>2</sup>/g for the three HPC-FC samples. The pore volume was found to amount to between 0.32 and 0.91 cm<sup>3</sup>/g and the pore size was determined to be between 2.9 and 4.3 nm. All the morphological characteristics for the HPC-FC are summarized in Table 6.1.

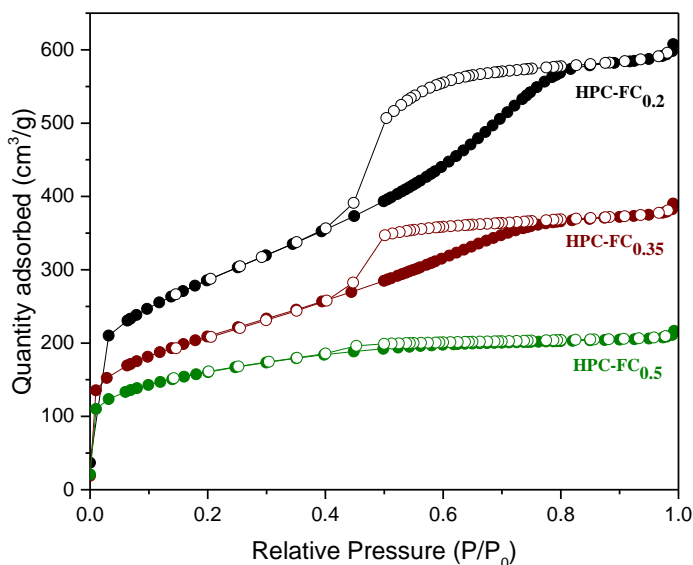


**Figure 6.4.** N<sub>2</sub> adsorption (full symbols) – desorption (empty symbols) isotherms of hierarchical porous carbon produced with three different loadings of spent coffee grounds (HPC-FC)

**Table 6.1.** Morphological characteristics of hierarchical porous carbon produced with filter coffee waste (HPC-FC), based on the measured N<sub>2</sub> adsorption at 77 K, analysed with the Barrett-Joyner-Halenda method

Sample	Specific surface area (m <sup>2</sup> /g) according to BET	Pore size (nm)	Pore volume (cm <sup>3</sup> /g)
HPC-FC <sub>0.2</sub>	1009	4.3	0.91
HPC-FC <sub>0.35</sub>	736	3.7	0.58
HPC-FC <sub>0.5</sub>	580	2.9	0.32

Characteristic SEM images of the HPC-FC structures are shown in Figure 6.5 (a-c). HPC-FC is made up of micron-sized particles consisting of a three-dimensional network of connected macroporous channels with thin carbon walls. The different contrast in each area hints the presence of empty cavities and there seems to be disordered porosity. In the image with the higher magnification one can clearly distinguish the rough surface structure that is usually seen in mesoporous materials.

The next synthetic step was to substitute commercial sucrose with waste products from sugar production. Two attempts were made: first we replaced sucrose with molasses and then we employed sugar beet root extract as sugar source. The morphology of the result, of the first attempt, HPC-M<sub>1:1</sub>, which has quite similar morphology as HPC-FC, can be seen in the SEM images shown in Figure 6.5 (d-e) and that of the two loadings applied in the second attempt, HPC-B<sub>10</sub> and HPC-B<sub>20</sub>, in Figure 6.8. The similarity to the previously reported<sup>37</sup> fishbone-like structure is an indication for the successful synthesis of HPCs.

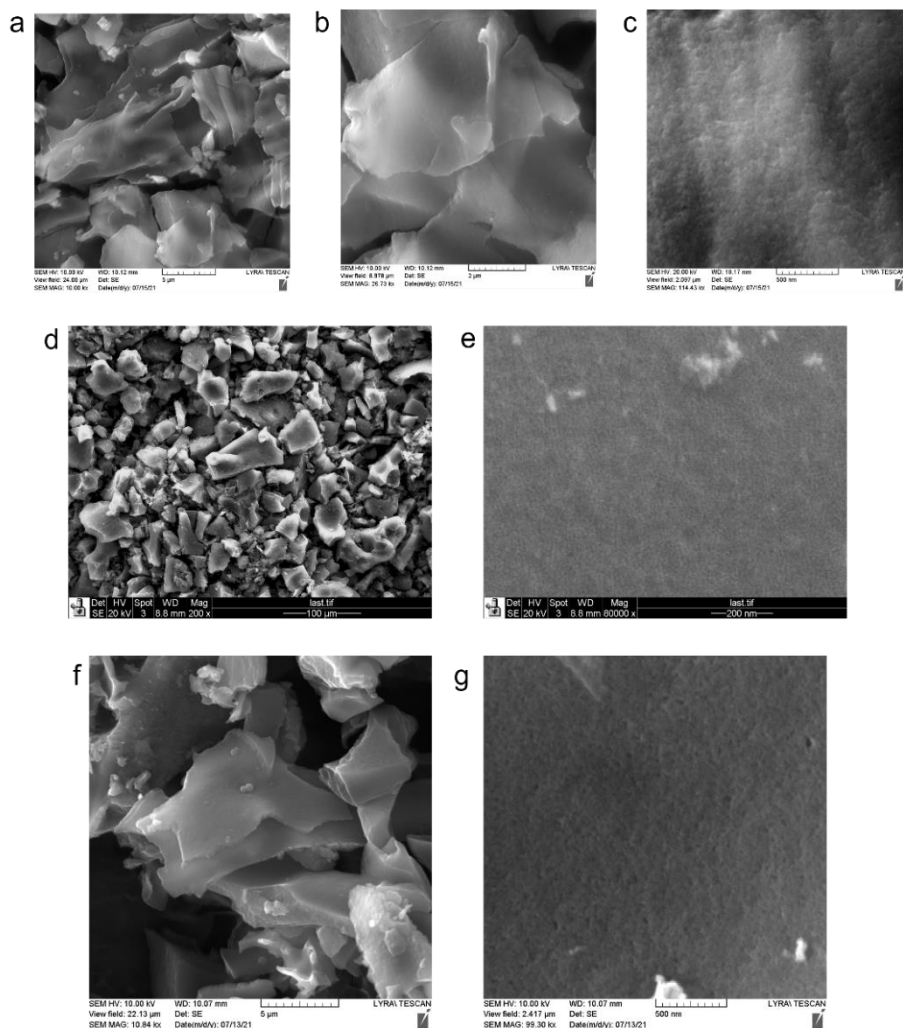


**Figure 6.5.** SEM images of hierarchical porous carbon produced with (a-c) filter coffee waste - HPC-FC, (d, e) molasses wastewater - HPC-M<sub>1:1</sub> and (f, g) filter coffee waste and molasses wastewater - HPC-M/FC<sub>1:1</sub>

The nitrogen adsorption-desorption isotherms for the two HPC-M samples are shown in Figure 6.6, while Figure 6.7 presents the isotherms for the two HPC-B samples. The data were analysed in the same way as described for the HPC-FC samples. The morphological characteristics are summarized in Table 6.2. Molasses wastewater proved to be a better potential candidate for substituting sucrose in the synthesis of the HPCs, since structures with a specific surface area of up to 862 m<sup>2</sup>/g could be produced.

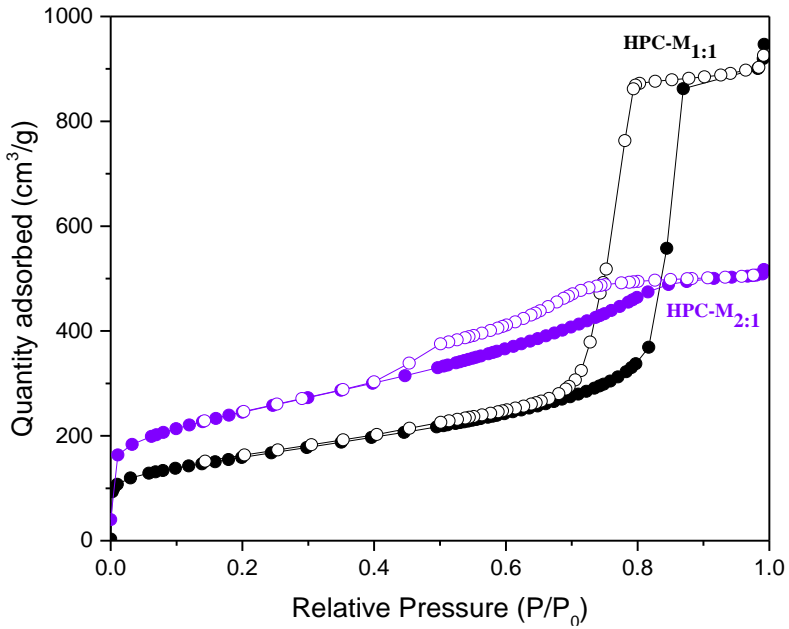


**Figure 6.6.** N<sub>2</sub> adsorption (full symbols) – desorption (empty symbols) isotherms of hierarchical porous carbon produced with two different loadings of molasses wastewater - HPC-M

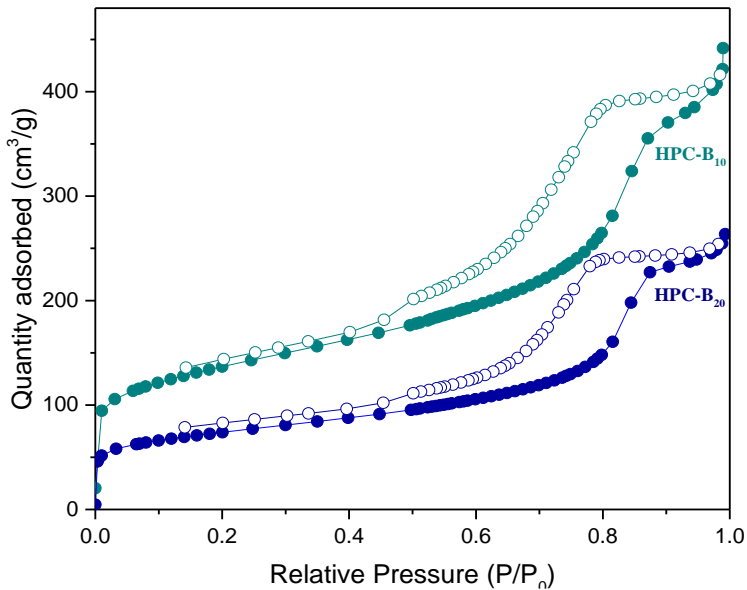


**Figure 6.7.** N<sub>2</sub> adsorption (full symbols) – desorption (empty symbols) isotherms of hierarchical porous carbon produced with two different loadings of sugar beet extract waste - HPC-B

As expected,<sup>37</sup> when increasing the silica to sugar ratio, the specific surface area is significantly higher than the one achieved for a 1:1 ratio. In the case of the beet root extract, it should be noted that when doubling the amount of waste added, the pore volume and surface area are decreasing by ~ 50 %, which can also be explained by the change in silica to sugar ratio.

As far as the adsorption-desorption isotherms are concerned, in both types of samples a hysteresis loop is found again, indicative of the existence of mesopores. In the SEM images of the HPC-B we observe a structure quite different from the rest of the porous carbons developed here. Due to the low percentage of sugar in the sugar beet root extract waste, the rest of the unidentified impurities that are present have an active role in the formation of the structure. The SEM image in Figure 6.8(c) shows that the hollow macroporous structure of the HPC-B that is created during sublimation remains unaltered throughout the calcination and etching procedure.

**Table 6.2.** Morphological properties of HPC-M, HPC-B and HPC-M/FC (measured by N<sub>2</sub> adsorption at 77 K with the BJH method)

Sample	Specific surface area (m <sup>2</sup> /g) according to BET	Pore size (nm)	Pore volume (cm <sup>3</sup> /g)
HPC-M <sub>1:1</sub>	559	12.1	1.40
HPC-M <sub>2:1</sub>	862	4.4	0.79
HPC-B <sub>10</sub>	482	7.8	0.64
HPC-B <sub>20</sub>	260	8.7	0.39
HPC-M/FC <sub>1:1</sub>	643	4.3	0.59
HPC-M/FC <sub>1:2</sub>	361	11.6	0.87

Finally, when molasses waste and filter coffee waste were employed in the synthesis, the resulting porous carbon structures gave rise to the adsorption-desorption isotherms presented in Figure 6.9. Analysis following BET gave specific surface area values of  $\sim 300\text{-}600\text{ m}^2/\text{g}$ ; this implies that the coffee waste affects negatively the porous structure, in agreement with our findings for the first set of samples (see Table 6.1). The morphological properties are summarized in Table 6.2. The properties that the coffee waste could add to the porous materials synthesized (*e.g.* the nitrogen content) should be explored and, depending on the target of the specific application envisioned, a balance between functionalities and porosity should be found.

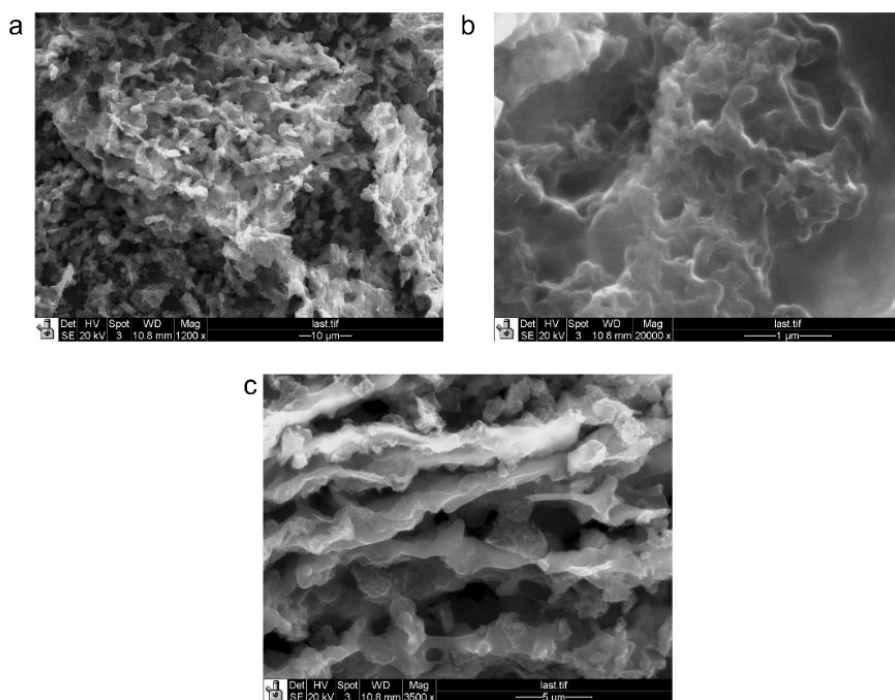


**Figure 6.8.** SEM images of hierarchical porous carbon produced with two different loadings of sugar beet extract waste (a, b ) HPC-B<sub>10</sub> and (c) HPC-B<sub>20</sub>

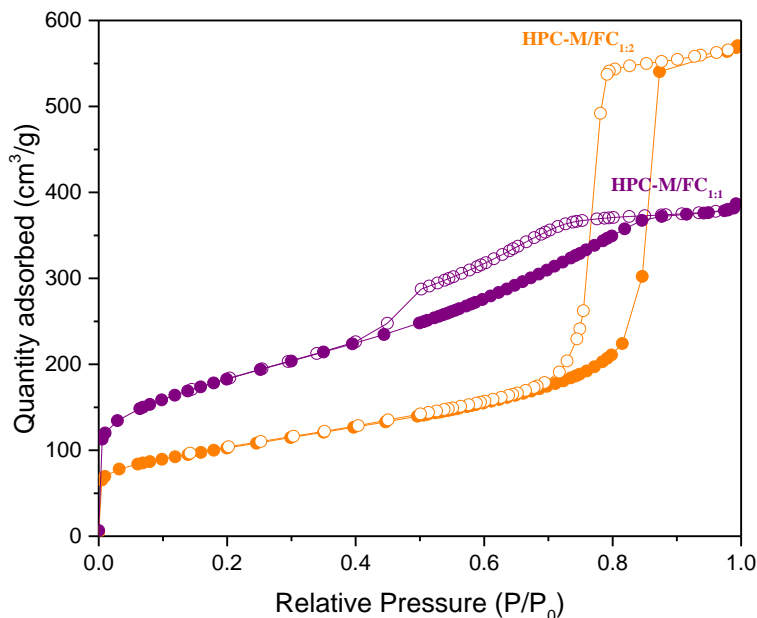
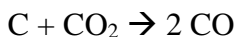


**Figure 6.9.**  $N_2$  adsorption (full symbols) – desorption (empty symbols) isotherms of hierarchical porous carbon produced with two different loadings of molasses wastewater and filter coffee waste - HPC-M/FC

After having ascertained that we had indeed been successful in the production of mesoporous carbons, three samples were selected for  $CO_2$  activation to enhance and improve their properties.  $CO_2$  activation is performed within the temperature range of 800-1000 °C; at this temperature the carbon structure interacts with the gas and carbon atoms are removed from the porous framework in a controlled way, thereby micropores are created and the pore volume of already existing smaller pores increases. The reaction that takes place is described by:



Flow rate, reaction time, temperature as well as the specific furnace design are parameters that can lead to completely different results.<sup>37, 38</sup> In the study described here we decided to keep all parameters the same and use a reaction time and temperature that were proven to produce positive results on the previously published HPCs on which we based our project. Activation in oxidative gases is a simple process that gives good control over porosity, despite the significant losses in carbon. The weight loss during the activation process for the selected samples was 51.5 % for



HPC-M<sub>2:1</sub>, 45.5 % for HPC-M/FC<sub>1:1</sub> and 61.0 %, for HPC-B<sub>10</sub>, which promises well for the success of the activation procedure.

The introduction of the micropores through the activation step was confirmed by the increase in specific surface area; the latter augmented by 54.9 % for HPC-M<sub>2:1</sub>, by 45.3 % for HPC-M/FC<sub>1:1</sub>, and by impressive 127.6 % in the case of HPC-B<sub>10</sub> (see Table 6.3). The nitrogen adsorption-desorption isotherms of the three activated samples are shown in comparison with the isotherms of the samples before the activation in Figures 6.10(a), 6.11(a) and 6.12(a). It is easily seen that all activated carbons show a steep nitrogen uptake at low pressure ( $p/p_0$ ) related to the filling of the micropores. The morphological properties are summarized in Table 6.3.

**Table 6.3.** Morphological properties of the three activated samples (Total surface area was calculated by the BET model and pore size distribution was calculated by the QSDFT method on adsorption isotherm.)

Sample	$S_{\text{BET}}$ (m <sup>2</sup> /g)	Total pore volume (cm <sup>3</sup> /g)	$V_{\text{micro}}$ (cm <sup>3</sup> /g)	$V_{\text{meso}}$ (cm <sup>3</sup> /g)
<b>HPC-M<sub>2:1</sub>Act</b>	1335 (862)*	1.15	0.34	0.81
<b>HPC-B<sub>10</sub>Act</b>	1097 (482)*	1.22	0.28	0.94
<b>HPC-M/FC<sub>1:1</sub>Act</b>	934 (643)*	0.86	0.17	0.69

\* The specific surface area before the activation is shown for comparison.

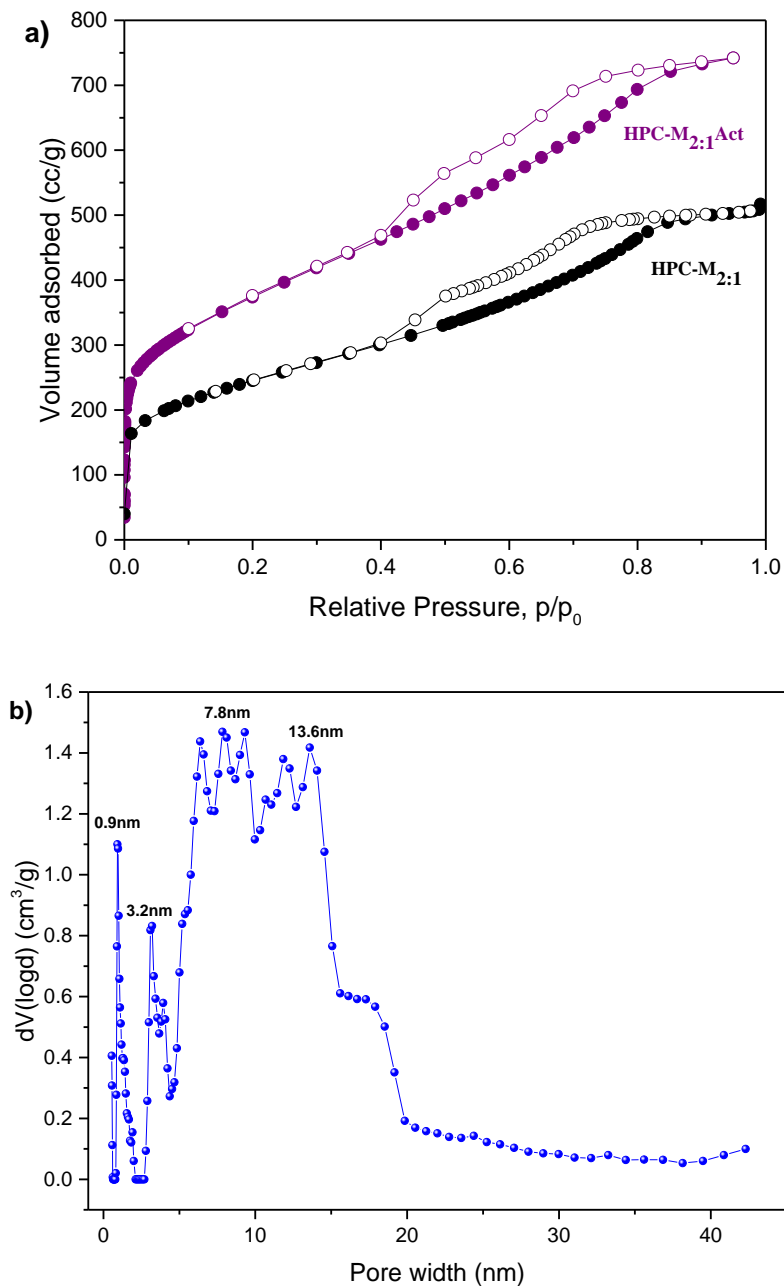


**Figure 6.10.**  $N_2$  adsorption (full symbols) – desorption (empty symbols) isotherms of HPC- $M_{2:1}$  before and after activation (a) and pore size distribution of the activated sample as derived by DFT (b)

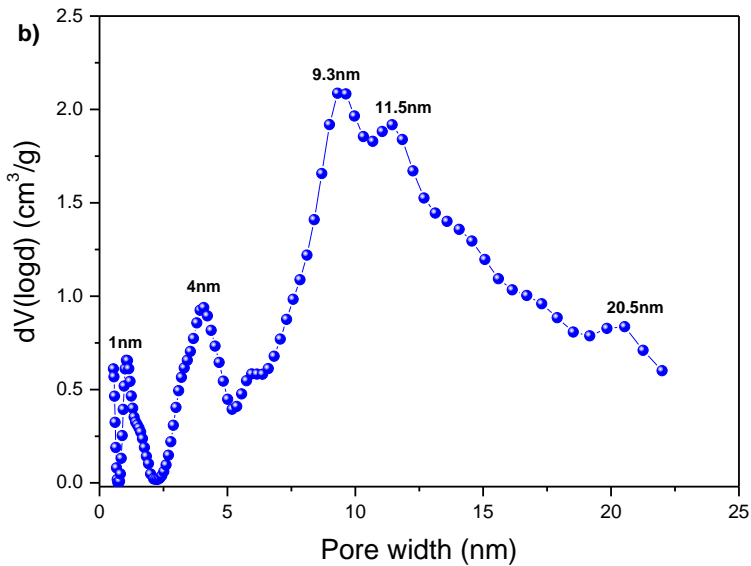
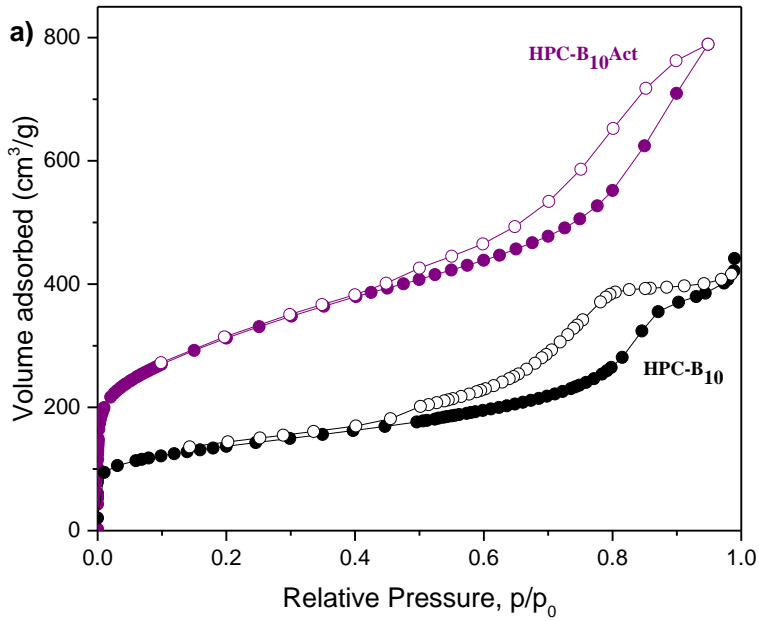


**Figure 6.11.**  $N_2$  adsorption (full symbols) – desorption (empty symbols) isotherms of HPC-B<sub>10</sub> before and after activation (a) and pore size distribution of the activated sample as derived by DFT (b)

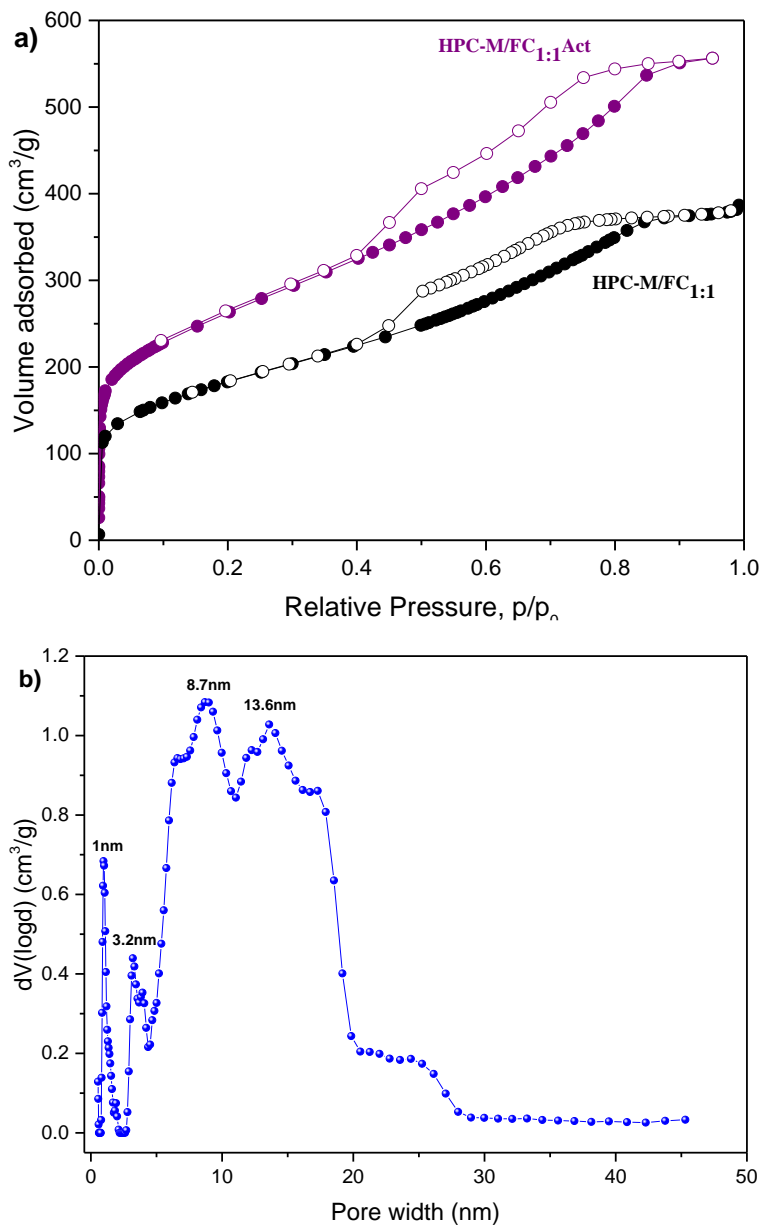


**Figure 6.12.**  $N_2$  adsorption (full symbols) – desorption (empty symbols) isotherms of HPC-M/FC<sub>1:1</sub> before and after activation (a) and pore size distribution of the activated sample as derived by DFT (b)

The pore diameter of the mesopores, which is centred around 11-13 nm for all samples (Figures 6.10(b), 6.11(b) and 6.12(b)), corresponds to the size of the colloidal silica used (12 nm) proving that the mesoporosity can be controlled through the choice of the hard template. The slightly bigger pores present could be caused by aggregation of the silica particles during the freeze-casting step, which happens because the amount of sugar is insufficient to ‘wrap’ them. In Figure 6.13, the SEM images of the samples after the activation process are presented.

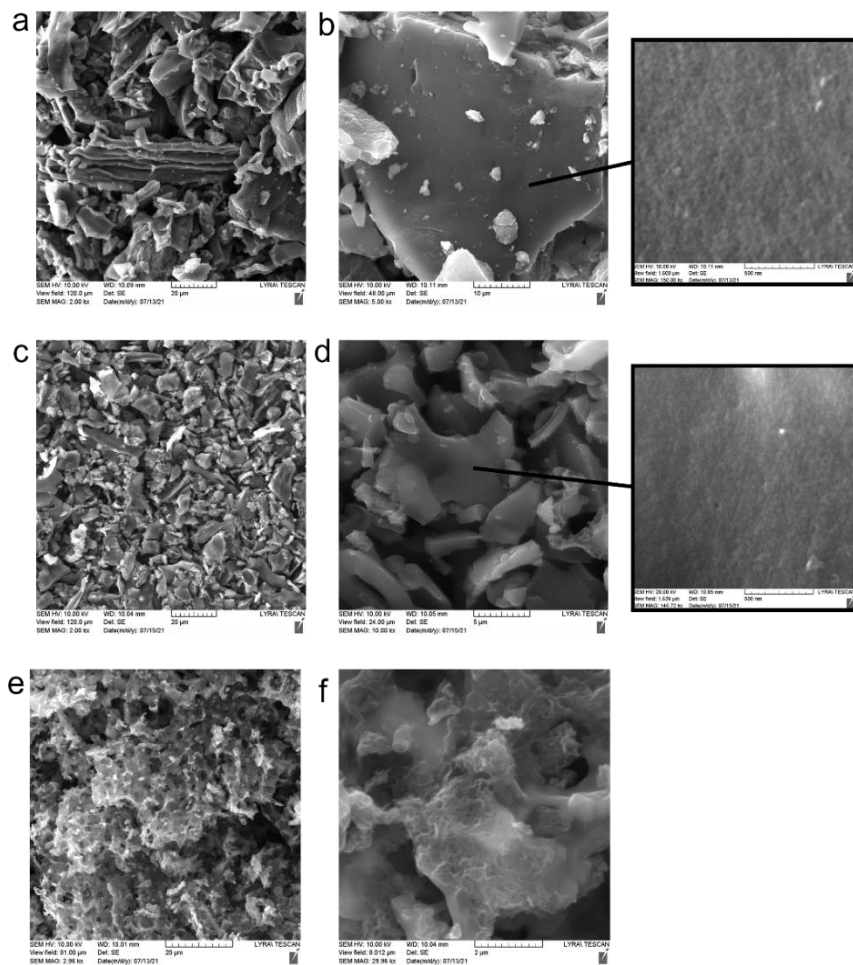


**Figure 6.13.** SEM images after the CO<sub>2</sub> activation of different types of hierarchical porous carbon produced with waste products: HPC-M<sub>2:1</sub> synthesized adding molasses wastewater (a-b), HPC-M/FC<sub>1:1</sub> synthesized adding molasses wastewater and filter coffee waste (c-d) and HPC-B<sub>10</sub> synthesized adding sugar beet extract waste (e-f)

The morphology of the porous carbons appears to be less dense, but the physical activation has not caused substantial changes to the structures.

#### **6.4. Conclusions**

In conclusion, four different types of porous carbons were produced adding waste products in the synthesis and following a facile approach that combined ice and hard (colloidal silica) templates, in order to create macropores and mesopores, respectively. The as-synthesized porous carbons possess specific surface areas ranging from 260 to 1009 m<sup>2</sup>/g, and after their porous characteristics were evaluated, three of them were also subjected to physical activation with CO<sub>2</sub>, which introduced micropores in the structures and led to even larger specific surface areas and pore volumes. The porous structures synthesized show a great potential and could be ideal candidates for sorption and supercapacitor applications.

## References

1. B. Yao, H. Peng, H. Zhang, J. Kang, C. Zhu, G. Delgado, D. Byrne, S. Faulkner, M. Freyman, X. Lu, M. A. Worsley, J. Q. Lu and Y. Li, *Nano Letters*, 2021, **21**, 3731-3737.
2. W. Yu, H. Wang, S. Liu, N. Mao, X. Liu, J. Shi, W. Liu, S. Chen and X. Wang, *Journal of Materials Chemistry A*, 2016, **4**, 5973-5983.
3. X. Lu, G.-P. Hao, X. Sun, S. Kaskel and O. G. Schmidt, *Journal of Materials Chemistry A*, 2017, **5**, 6284-6291.
4. Y. An, Q. Zhu, L. Hu, S. Yu, Q. Zhao and B. Xu, *Journal of Materials Chemistry A*, 2016, **4**, 15605-15611.
5. R. Sahore, L. P. Estevez, A. Ramanujapuram, F. J. DiSalvo and E. P. Giannelis, *Journal of Power Sources*, 2015, **297**, 188-194.
6. P. Zhang, J. Li and M. B. Chan-Park, *ACS Sustainable Chemistry & Engineering*, 2020, **8**, 9291-9300.
7. M. Sharma, J. Singh, S. Hazra and S. Basu, *Journal of Environmental Chemical Engineering*, 2018, **6**, 2829-2836.
8. X. Yuan, N. An, Z. Zhu, H. Sun, J. Zheng, M. Jia, C. Lu, W. Zhang and N. Liu, *Process Safety and Environmental Protection*, 2018, **119**, 320-329.
9. W. Xiao, X. Jiang, X. Liu, W. Zhou, Z. N. Garba, I. Lawan, L. Wang and Z. Yuan, *Journal of Cleaner Production*, 2021, **284**, 124773.
10. M. Li, F. Xu, H. Li and Y. Wang, *Catalysis Science & Technology*, 2016, **6**, 3670-3693.
11. W. Liu, D. Xu and X. Li, *ChemNanoMat*, 2019, **5**, 201-207.
12. L. Tong, Y.-C. Wang, M.-X. Chen, Z.-Q. Chen, Q.-Q. Yan, C.-L. Yang, Z.-Y. Zhou, S.-Q. Chu, X. Feng and H.-W. Liang, *Chemical Science*, 2019, **10**, 8236-8240.
13. N. Balahmar, A. C. Mitchell and R. Mokaya, *Advanced Energy Materials*, 2015, **5**, 1500867.
14. B. Adeniran and R. Mokaya, *Nano Energy*, 2015, **16**, 173-185.
15. D. Giasafaki, G. Charalambopoulou, C. Tampaxis, K. Dimos, D. Gournis, A. Stubos and T. Steriotis, *Carbon*, 2016, **98**, 1-14.
16. A. Stein, Z. Wang and M. A. Fierke, *Advanced Materials*, 2009, **21**, 265-293.
17. R.-w. Fu, Z.-h. Li, Y.-r. Liang, F. Li, F. Xu and D.-c. Wu, *New Carbon Materials*, 2011, **26**, 171-179.
18. F. Rodríguez-Reinoso, M. Molina-Sabio and M. T. González, *Carbon*, 1995, **33**, 15-23.

19. J. Wang and S. Kaskel, *Journal of Materials Chemistry*, 2012, **22**, 23710-23725.
20. M. A. Lillo-Ródenas, D. Cazorla-Amorós and A. Linares-Solano, *Carbon*, 2003, **41**, 267-275.
21. J. N. Burrow, J. P. Pender, J. V. Guerrero, B. R. Wygant, J. E. Eichler, D. C. Calabro and C. B. Mullins, *ACS Applied Nano Materials*, 2020, **3**, 5965-5977.
22. H. Teng and T.-S. Yeh, *Industrial & Engineering Chemistry Research*, 1998, **37**, 58-65.
23. A. M. Aljumaily and R. Mokaya, *Materials Advances*, 2020, **1**, 3267-3280.
24. A. Ahmadpour and D. D. Do, *Carbon*, 1996, **34**, 471-479.
25. X.-q. Zhang, W.-c. Li and A.-h. Lu, *New Carbon Materials*, 2015, **30**, 481-501.
26. L. F. Ballesteros, J. A. Teixeira and S. I. Mussatto, *Food and Bioprocess Technology*, 2014, **7**, 3493-3503.
27. P. S. Murthy and M. Madhava Naidu, *Resources, Conservation and Recycling*, 2012, **66**, 45-58.
28. P. Zhao, M. H. A. Shiraz, H. Zhu, Y. Liu, L. Tao and J. Liu, *Electrochimica Acta*, 2019, **325**, 134931.
29. J. Choi, C. Zequine, S. Bhoyate, W. Lin, X. Li, P. Kahol and R. Gupta, *C*, 2019, **5**, 44.
30. L. Khenniche and F. Benissad-Aissani, *Journal of Chemical & Engineering Data*, 2010, **55**, 4677-4686.
31. M. G. Plaza, A. S. González, C. Pevida, J. J. Pis and F. Rubiera, *Applied Energy*, 2012, **99**, 272-279.
32. C. Tsiptsias, D. C. Banti and P. Samaras, *Journal of Chemical Technology & Biotechnology*, 2016, **91**, 857-864.
33. B. Zhang, H. Zhao, S. Zhou, C. Shi, C. Wang and J. Ni, *Bioresource Technology*, 2009, **100**, 5687-5693.
34. G. Wei, L. Shao, J. Mo, Z. Li and L. Zhang, *Environmental Science and Pollution Research*, 2017, **24**, 15067-15077.
35. L. Estevez, R. Dua, N. Bhandari, A. Ramanujapuram, P. Wang and E. P. Giannelis, *Energy & Environmental Science*, 2013, **6**, 1785-1790.
36. E. P. Barrett, L. G. Joyner and P. P. Halenda, *Journal of the American Chemical Society*, 1951, **73**, 373-380.
37. L. Estevez, R. Dua, N. Bhandari, A. Ramanujapuram, P. Wang and E. P. Giannelis, *Energy & Environmental Science*, 2013, **6**, 1785-1790.



38. L. Estevez, V. Prabhakaran, A. L. Garcia, Y. Shin, J. Tao, A. M. Schwarz, J. Darsell, P. Bhattacharya, V. Shutthanandan and J.-G. Zhang, *ACS Nano*, 2017, **11**, 11047-11055.



## Summary

The demands of modern society for new materials, novel applications and cutting-edge technologies are increasing day by day, and the scientific community seems to be involved in a never-ending race for new breakthroughs. Time weighs in on the emergent need for replacement of traditional materials by new and more efficient ones, especially when nearly depleted sources are involved in their production. Furthermore, any new approach has to conform with the demands for a greener, waste-free, and less energy- and resource-demanding future.

Nanoporous materials have been exploited since antiquity, and are nowadays applied in the fields of catalysis, energy (hydrogen storage, supercapacitors, Li-ion batteries, fuel cells and sensors), environmental remediation (molecular sieves/adsorbents, NO<sub>x</sub> and H<sub>2</sub>S removal, CO<sub>2</sub> capture), and even medicine because of their controllable pore size, diverse geometries, surface properties and their ability to interact with molecules and atoms or adsorb/release them. Since carbon is amongst the most abundant elements on earth, and can be found in a plethora of forms, carbon materials are excellent candidates for applications that involve porosity.

Porosity in materials can be obtained in many ways; in this PhD project the focus lays on porous carbons resulting from carbonization, chemical etching, template synthesis and activation, or 'Parthenon like' structures. The latter were constructed through the intercalation of robust organic and/or inorganic pillars between graphene sheets in order to keep the layers apart and create interconnected void spaces, combining in this way the properties of graphene with porosity.

This thesis is divided in two parts; the first half is devoted to pillared graphenes (Chapters 3 & 4), and the second part (Chapters 5 & 6) is dedicated to highly porous carbon structures.

In Chapter 3, a rapid synthetic procedure to create highly porous heterostructures with tailored properties through the silylation of organically modified graphene oxide is presented. Three distinct silica precursors (1,4-bis(triethoxysilyl)-benzene - BTB, tetraethylorthosilicate

– TEOS and (3-aminopropyl)triethoxysilane - APTEOS) with different structural characteristics were used as building blocks for pillars between organo-modified graphene oxide layers. The idea was to develop high yield silica networks within the interlayer space through sol-gel reactions. Thermal decomposition enabled the removal of the organic molecules thereby generating porous heterostructures with very high surface area and sponge-like make-up, which are very attractive for potential use in catalysis, sorption and as fillers in polymer nanocomposites. The final products were fully characterized with a combination of techniques (X-ray diffraction, Fourier transform infrared and X-ray photoelectron spectroscopies, thermogravimetric analysis, scanning electron microscopy and porosity measurements) and the degree of silylation of each reagent was evaluated. The porous heterostructure bridged with a phenyl group showed the maximum amount of silica content in the final heterostructure and subsequent pyrolysis was found to create the desired porous structure with a specific surface area up to  $550 \text{ m}^2/\text{g}$ . For this hybrid the potential as sorbent of  $\text{CO}_2$  was briefly explored and a high  $\text{CO}_2$  adsorption capacity of  $3.5 \text{ mmol/g}$  at 5 bar and  $0 \text{ }^\circ\text{C}$  was found, which is promising for further consideration as  $\text{CO}_2$  storage material.

Chapter 4 describes the intercalation of pillaring species between graphene oxide (GO) layers to create a robust 3-D network of graphene sheets. Octameric oligosiloxanes were formed through the hydrolytic polycondensation of N-[3-(trimethoxysilyl)propyl]-ethylenediamine (EDAPTEOS) and intercalated in three different loadings (1.5, 4.5 and 9 mmol). Silsesquioxanes, apart from helping to create a nanoporous structure, render the materials strong  $\text{CO}_2$  adsorbents due to the unreacted amine groups emanating in the open space between the GO sheets, which warrant  $\text{CO}_2$  binding. Air-drying and freeze-drying were used to achieve distinct morphologies, verified by SEM microscopy. The successful intercalation was confirmed by X-ray diffraction and FT-IR spectroscopy, the relative amount of silicon oxide for each loading was defined by thermogravimetric analysis, the atomic percentages of the elements present in the samples as well as an insight on the type of interactions were gained through X-ray photoelectron spectroscopy. The pore characteristics were studied by nitrogen porosimetry, and the  $\text{CO}_2$  adsorption behaviour for all samples was investigated by recording the corresponding adsorption isotherms at 273 K and 298 K, up to 1 bar. We could show that freeze-

drying significantly enhances the porosity as compared to air-drying and this morphology can lead to an enhanced CO<sub>2</sub> adsorption capacity if an optimal loading of the pillaring agent is chosen.

Chapter 5 focalises on a different environmental challenge, namely hydrogen sulfide removal. Based on the proven desulfurization performance of porous matrixes when combined with metal oxides, the use of copper enriched porous carbon cuboids in H<sub>2</sub>S capture is reported for the first time. Through a coordination reaction followed by a pyrolysis step, three different samples were prepared; a low-surface-area copper-rich structure, a highly porous carbon form without metal addition, and finally the same porous carbon decorated with copper. The pore characteristics of the samples were investigated by nitrogen adsorption-desorption analysis, and their metal content was determined by thermogravimetric analysis. X-ray photoelectron spectroscopy gave insight in the elemental composition and the chemical environment of the elements, while the morphology of the novel sorbents was studied with scanning electron microscopy. To explore how the high surface area and the presence of copper oxide can be balanced and how they synergistically affect hydrogen sulphide removal, the performance of the porous carbon cuboids was evaluated with a H<sub>2</sub>S chemisorption experiment at 150 °C. The sorbents with the higher porosity showed lower sorption capacity and were also catalytically active. The copper-rich sample with the lowest surface area was proved to function also as a catalyst, with selective oxidation of hydrogen sulphide taking place. This copper-rich sample was investigated a bit further and the chapter reports on ideas about the potential mechanism behind the catalytic activity put forward. Further improvement of the designed materials could lead in high performance catalysts suitable for H<sub>2</sub>S conversion.

Aiming at waste reuse for the development of high-performance sorbents, in Chapter 6, a set of novel hierarchical porous carbons (carbons that combine all three kinds of porosity), which were synthesized by incorporating sugar waste and spent coffee grounds, is presented for the first time. Four kinds of porous carbons were developed in total: one using molasses wastewater in combination with silica as a composite starting material; another one using sugar beet root extract waste and silica; a third one where spent coffee grounds served as reinforcement in an attempt to introduce functional groups that could be beneficial for future applications; and a last one where two kinds of waste (molasses and spent coffee

grounds) were combined. The properties and surface characteristics of all the produced hierarchical porous carbons were studied with N<sub>2</sub> porosimetry and scanning electron microscopy. Specific surface areas in the range of 260-1009 m<sup>2</sup>/g were achieved. Three of the samples were subjected to physical activation with CO<sub>2</sub>, that resulted in maximization of the specific area up to 127 % after the introduction of microporosity. All the synthesized samples show a great potential and could be ideal candidates for sorption, water remediation and supercapacitor applications.

# Samenvatting

De moderne samenleving eist altijd meer nieuwe materialen, nieuwe toepassingen en geavanceerdere technologieën, en de wetenschappelijke gemeenschap lijkt verwikkeld te zijn in een nooit eindigende race voor nieuwe doorbraken. De opkomende behoefte aan vervanging van traditionele materialen door nieuwe en efficiëntere materialen, vooral wanneer bijna uitgeputte bronnen betrokken zijn bij de productie, zijn urgenter dan ooit. Bovendien moet elke nieuwe aanpak voldoen aan de eisen voor een groenere, afvalvrije en minder energie- en bronnenverslindende toekomst.

Nanoporeuze materialen worden al sinds de oudheid gebruikt en worden tegenwoordig toegepast op het gebied van katalyse, energie (waterstofopslag, supercondensatoren, Li-ionbatterijen, brandstofcellen en sensoren), milieusanering (moleculaire zeven/sorptiemiddel, NO<sub>x</sub>- en H<sub>2</sub>S-verwijdering, CO<sub>2</sub>-afvang), en zelfs medicijnen vanwege hun controleerbare porie grootte, diverse geometrieën, oppervlakte-eigenschappen en hun vermogen om te interageren met moleculen en atomen of deze te adsorberen/af te geven. Omdat koolstof een van de meest voorkomende elementen op aarde is en in een overvloed aan vormen kan worden gevonden, zijn koolstofmaterialen uitstekende kandidaten voor toepassingen waarbij porositeit betrokken is.

Porositeit in materialen kan op vele manieren worden gegenereerd; in dit doctoraatsthesis lag de focus op poreuze koolstoffen die het resultaat zijn van carbonisatie, chemisch etsen, sjabloonsynthese en -activering, of 'Parthenon-achtige' structuren. De laatste werden geconstrueerd door de intercalatie van robuuste organische en/of anorganische pilaren tussen grafeenplaten om de lagen uit elkaar te houden en onderling verbonden lege ruimtes te creëren, waarbij de eigenschappen van grafeen op deze manier werden gecombineerd met porositeit.

Dit proefschrift is opgedeeld in twee delen; de eerste helft is gewijd aan grafenen met pilaren (Hoofdstukken 3 en 4) en het tweede deel (Hoofdstukken 5 en 6) is gewijd aan zeer poreuze koolstofstructuren.

In Hoofdstuk 3 wordt een eenvoudige synthetische procedure gepresenteerd om zeer poreuze heterostructuren met op maat gemaakte eigenschappen te creëren door de silylering van organisch gemodificeerd grafeenoxide. Drie verschillende silicaprecursoren (1,4-

bis(triethoxysilyl)-benzeen - BTB, tetraethylorthosilicaat - TEOS en (3-aminopropyl)triethoxysilaan - APTEOS) met verschillende structurele kenmerken werden gebruikt als bouwstenen voor pijlers tussen organogemodificeerde grafeenoxidelagen. Het idee was om silicanetwerken met een hoge opbrengst te ontwikkelen binnen de tussenlaagruimte door middel van sol-gelreacties. Thermische ontleding maakte de verwijdering van de organische moleculen mogelijk, waardoor poreuze heterostructuren met een zeer groot oppervlak en sponsachtige samenstelling werden gegenereerd, die zeer aantrekkelijk zijn voor mogelijk gebruik bij katalyse, sorptie en als vulstoffen in polymere nanocomposieten. De eindproducten werden volledig gekarakteriseerd met een combinatie van technieken (röntgendiffractie, Fouriertransformatie infrarood- en röntgenfoto-elektronspectroscopieën, thermogravimetrische analyse, scanning-elektronenmicroscopie en porositeitsmetingen) en de mate van silylering van elk reagens werd geëvalueerd. De poreuze heterostructuur overbrugd met een fenylgroep vertoonde de maximale hoeveelheid silica in de uiteindelijke heterostructuur en daaropvolgende pyrolyse bleek de gewenste poreuze structuur te creëren met een specifiek oppervlak tot  $550 \text{ m}^2/\text{g}$ . Voor deze hybride werd het potentieel als sorptiemiddel van  $\text{CO}_2$  kort verkend en werd een hoge  $\text{CO}_2$ -adsorptiecapaciteit van  $3,5 \text{ mmol/g}$  bij 5 bar en  $0 \text{ }^\circ\text{C}$  gevonden, wat veelbelovend is voor verdere ontwikkeling als  $\text{CO}_2$ -opslagmateriaal.

Hoofdstuk 4 beschrijft de intercalatie van pilaarvormende soorten tussen grafeenoxide (GO)-lagen om een robuust 3D-netwerk van grafeenlaagjes te creëren. Octameer oligosiloxanen werden gevormd door de hydrolytische polycondensatie van N-[3-(trimethoxysilyl)propyl]-ethyleendiamine (EDAPTEOS) en geïntercaleerd met drie verschillende ladingen (1,5, 4,5 en 9 mmol). Silsesquioxanen helpen niet alleen bij het creëren van een nanoporeuze structuur, maar maken de materialen ook sterke  $\text{CO}_2$ -adsorptiemiddelen vanwege de niet-gereageerde aminegroepen die  $\text{CO}_2$  binden. Luchtdrogen en vriesdregen werden gebruikt om verschillende morfologieën te creëren, geverifieerd door SEM-microscopie. De succesvolle intercalatie werd bevestigd door röntgendiffractie en FT-IR-spectroscopie, de relatieve hoeveelheid siliciumoxide voor elke lading werd bepaald door thermogravimetrische analyse, de atoompercentages van de elementen die in de monsters aanwezig zijn, evenals een inzicht in het type van interacties werden verkregen door middel van röntgenfoto-elektronspectroscopie. De porie kenmerken werden bestudeerd door stikstofporosimetrie en het  $\text{CO}_2$ -adsorptiegedrag van alle monsters werd onderzocht door de adsorptie-



isothermen bij 273 K en 298 K, tot 1 bar, te registreren. We konden aantonen dat vriesdrogen de porositeit aanzienlijk verbetert in vergelijking met drogen aan de lucht en deze morfologie kan leiden tot een verhoogde CO<sub>2</sub>-adsorptiecapaciteit als een optimale lading van het pilaarmiddel wordt gekozen.

Hoofdstuk 5 focust op een andere milieu-uitdaging, namelijk de verwijdering van waterstofsulfide. Op basis van de bewezen ontzwevelingsprestaties van poreuze matrices in combinatie met metaaloxiden, wordt voor het eerst het gebruik van met koper verrijkte poreuze koolstofblokken bij H<sub>2</sub>S-afvang gerapporteerd. Door een coördinatiereactie gevolgd door een calcineringsstap werden drie verschillende monsters bereid; een koperrijke structuur met een laag oppervlak, een zeer poreuze koolstofvorm zonder metaaltoevoeging en tenslotte dezelfde poreuze koolstof verrijkt met koper. De porie kenmerken van de monsters werden onderzocht door middel van stikstofadsorptie-desorptie-analyse en hun metaalgehalte werd bepaald door thermogravimetrische analyse. Röntgenfoto-elektronenspectroscopie gaf inzicht in de elementaire samenstelling en de chemische omgeving van de elementen, terwijl de morfologie van de nieuwe sorptiemiddelen werd bestudeerd met scanning-elektronenmicroscopie. Om te onderzoeken hoe het grote oppervlak en de aanwezigheid van koperoxide in evenwicht kunnen worden gebracht en hoe ze synergetisch de verwijdering van waterstofsulfide beïnvloeden, werd de prestatie van de poreuze koolstofblokjes geëvalueerd met een H<sub>2</sub>S-chemisorptie-experiment bij 150 °C. De sorptiemiddelen met de hogere porositeit vertoonden een lagere sorptiecapaciteit en waren ook katalytisch actief. Het koperrijke monster met het laagste oppervlak bleek ook als katalysator te werken, waarbij selectieve oxidatie van waterstofsulfide plaatsvond. Dit koperrijke monster werd verder onderzocht en het hoofdstuk doet verslag van de ideeën over het mogelijke mechanisme achter de katalytische activiteit. Verdere verbetering van de ontworpen materialen zou kunnen leiden tot hoogwaardige katalysatoren die geschikt zijn voor H<sub>2</sub>S-conversie.

Met het oog op hergebruik van afval voor de ontwikkeling van hoogwaardige sorptiemiddelen, wordt in Hoofdstuk 6 voor de eerste keer een reeks nieuwe hiërarchische poreuze koolstoffen (koolstoffen die alle drie soorten porositeit combineren), die werden gesynthetiseerd met suikerafval en verbruikt koffiedik, gepresenteerd. In totaal zijn vier soorten poreuze koolstoffen ontwikkeld: één met melasse-afvalwater in combinatie met silica als composiet uitgangsmateriaal; een andere die

afval van suikerbietenwortel extract en silica gebruikt; een derde waar gebruikte koffiedik als versterking diende in een poging om functionele groepen te introduceren die gunstig zouden kunnen zijn voor toekomstige toepassingen; en een laatste waar twee soorten afval (melasse en koffiedik) werden gecombineerd. De eigenschappen en oppervlaktekenmerken van alle geproduceerde hiërarchische poreuze koolstoffen werden bestudeerd met N<sub>2</sub>-porosimetrie en scanning-elektronenmicroscopie. Specifieke oppervlakten in het bereik van 260-1009 m<sup>2</sup>/g werden bereikt. Drie van de monsters werden fysiek geactiveerd met CO<sub>2</sub>, wat resulteerde in maximalisatie van het specifieke oppervlakte tot 127 % na de introductie van microporositeit. Alle gesynthetiseerde monsters vertonen een groot potentieel en zouden ideale kandidaten kunnen zijn voor sorptie-, watersanerings- en supercondensator toepassingen.

## Περίληψη

Οι ανάγκες της σύγχρονης κοινωνίας για νέα υλικά, καινοτόμες εφαρμογές και τεχνολογίες αιχμής, αυξάνονται μέρα με τη μέρα, και η επιστημονική κοινότητα δείχνει να βρίσκεται σε ένα συνεχή αγώνα δρόμου για νέες ανακαλύψεις. Η αντικατάσταση των παραδοσιακών υλικών από νέα και πιο αποδοτικά υλικά κρίνεται πλέον επιτακτική, ιδιαίτερα όταν για την παραγωγή τους γίνεται χρήση που βρίσκονται σε έλλειψη. Επιπλέον, κάθε νέα προσέγγιση πρέπει να εναρμονίζεται με τις απαιτήσεις για ένα πιο πράσινο μέλλον, χωρίς απόβλητα, και χαμηλότερο ενεργειακό και υλικό αποτύπωμα.

Τα νανοπορώδη υλικά, των οποίων η εκμετάλλευση απαντάται ήδη από την αρχαιότητα, βρίσκουν εφαρμογή στην εποχή μας στα πεδία της κατάλυσης, της ενέργειας (αποθήκευση υδρογόνου, πυκνωτές, μπαταρίες ιόντων λιθίου, κελιά καυσίμων και αισθητήρες), την περιβαλλοντική αποκατάσταση (μοριακά κόσκινα/προσροφητικά, απομάκρυνση οξειδίων αζώτου και υδρόθειου), ακόμη και την ιατρική, χάρη στη δυνατότητα ελέγχου του μεγέθους των πόρων, της ποικιλόμορφης γεωμετρίας, των επιφανειακών ιδιοτήτων και της ικανότητάς τους να αλληλοεπιδρούν με μόρια και άτομα, ή να τα απορροφούν/απελευθερώνουν. Δεδομένου ότι ο άνθρακας συγκαταλέγεται μεταξύ των πλέον άφθονων στοιχείων στη γη, και μπορεί να βρεθεί σε πληθώρα μορφών, τα υλικά άνθρακα αποτελούν εξαιρετικές επιλογές για εφαρμογές που περιλαμβάνουν πορώδες.

Το πορώδες στα υλικά μπορεί να σχηματιστεί με πολλούς τρόπους: η παρούσα διδακτορική διατριβή εστιάζει στους πορώδεις άνθρακες που προκύπτουν από την ανθρακοποίηση, τη 'χημική χάραξη' (chemical etching), τη σύνθεση με χρήση προτύπου και την ενεργοποίηση, αλλά και υποστρωμένες δομές που προσομοιάζουν αυτή του Παρθενώνα. Τα τελευταία κατασκευάστηκαν μέσω της παρεμβολής στιβαρών οργανικών ή/και ανόργανων πυλώνων μεταξύ φύλλων γραφενίου, ώστε να διαχωρίζονται τα στρώματα και να δημιουργούνται διασυνδεδεμένοι κενοί χώροι, συνδυάζοντας με τον τρόπο αυτό τις ιδιότητες του γραφενίου με το πορώδες.

Η διατριβή αυτή χωρίζεται σε δύο μέρη: το πρώτο που είναι αφιερωμένο στα υποστυλωμένα γραφένια (Κεφάλαια 3 & 4), και το δεύτερο μέρος (Κεφάλαια 5 & 6) που αναφέρεται σε υψηλού πορώδους δομές άνθρακα.

Στο Κεφάλαιο 3, παρουσιάζεται μία ταχεία συνθετική διαδικασία για τη δημιουργία ετεροδομών υψηλού πορώδους με προσαρμοσμένες ιδιότητες μέσω της πυριτίωσης οργανικά τροποποιημένου οξειδίου του γραφενίου. Τρεις ξεχωριστές οργανοπυριτικές πρόδρομες ενώσεις (1,4-δισ(τριαιθοξυσιλυλο)-βενζόλιο - BTB, τετρα(αιθοξείδιο) του πυριτίου - TEOS και 3-αμινο-προπυλο τριαιθοξείδιο του πυριτίου - APTEOS) με διαφορετικά δομικά χαρακτηριστικά χρησιμοποιήθηκαν ως δομικά στοιχεία για τη δημιουργία υποστυλωτών μεταξύ των στρωμάτων του οργανικά τροποποιημένου οξειδίου του γραφενίου. Η ιδέα ήταν να αναπτυχθούν υψηλής απόδοσης πυριτικά δίκτυα στον ενδοστρωματικό χώρο, μέσω αντιδράσεων sol-gel. Η θερμική αποσύνθεση επέτρεψε την απομάκρυνση των οργανικών μορίων δημιουργώντας έτσι πορώδεις ετεροδομές με πολύ υψηλή ειδική επιφάνεια και σπογγοειδή δομή, οι οποίες είναι πολύ ελκυστικές για πιθανή χρήση σε κατάλυση, προσρόφιση, αλλά και ως πληρωτικά υλικά σε νανοσύνθετα πολυμερή. Τα τελικά υλικά χαρακτηρίστηκαν πλήρως με έναν συνδυασμό τεχνικών (περίθλαση ακτίνων-X, φασματοσκοπίες μέσου υπερύθρου και φωτοηλεκτρονίων ακτίνων-X, θερμική ανάλυση, ηλεκτρονική μικροσκοπία σάρωσης και μετρήσεις ειδικής επιφάνειας) και αξιολογήθηκε ο βαθμός πυριτίωσης για κάθε αντιδραστήριο. Η γεφυρωμένη με φαινυλομάδες πορώδης ετεροδομή έδειξε την μεγαλύτερη περιεκτικότητα σε πυρίτιο στην τελική του δομή, και η επακόλουθη πυρόλυση έδειξε να δημιουργεί την επιθυμητή πορώδη δομή με μία ειδική επιφάνεια που άγγιξε τα 550 m<sup>2</sup>/g. Για το συγκεκριμένο υβριδικό υλικό διερευνήθηκε εν συντομία η δυνατότητα προσρόφισης διοξειδίου του άνθρακα, και διαπιστώθηκε η υψηλή ικανότητα προσρόφησης του έως και 3.5 mmol/g στα 5 bar και 0 °C, τιμή η οποία το καθιστά πολλά υποσχόμενο για περαιτέρω εξέταση ως υλικό αποθήκευσης διοξειδίου του άνθρακα.

Το Κεφάλαιο 4 περιγράφει την ένθεση των ειδών υποστύλωσης ανάμεσα στις στρώσεις οξειδίου του γραφενίου με σκοπό τη δημιουργία ενός στιβαρού τρισδιάστατου δικτύου φύλλων γραφενίου. Τα οκταμερή ολιγοσιλοξάνια σχηματίστηκαν μέσω της υδρολυτικής πολυσυμπύκνωσης της N[-3-(τριμεθοξυσιλυλο)προπυλο]-αιθυλενοδιαμίνης (EDAPTEOS) και εντέθηκαν σε τρία διαφορετικά φορτία (1.5, 4.5 και 9 mmol). Τα

σιλοξάνια πέραν της συνεισφοράς τους στη δημιουργία της νανοπορώδους δομής, καθιστούν τα υλικά ισχυρούς προσροφητές διοξειδίου του άνθρακα χάρη στις μη αντιδρώσες αμινομάδες τους που με την παρουσία τους στον ανοιχτό χώρο μεταξύ των φύλλων γραφενίου, εγγυόνται την δέσμευση του διοξειδίου του άνθρακα. Χρησιμοποιώντας ξήρανση σε αέρα αλλά και λυοφιλίωση, δύο διακριτές μορφολογίες επιτεύχθηκαν, οι οποίες επαληθεύτηκαν με τη χρήση μικροσκοπίας SEM. Η επιτυχής ένθεση επιβεβαιώθηκε με περίθλαση ακτίνων-X και φασματοσκοπία FT-IR, το σχετικό ποσοστό οξειδίου του πυριτίου για κάθε φορτίο ορίστηκε με θερμική ανάλυση, και τα ατομικά ποσοστά των στοιχείων που υπάρχουν στα δείγματα, καθώς και μία εικόνα για το είδος των αλληλεπιδράσεων, αποκτήθηκαν μέσω της φασματοσκοπίας XPS. Τα πορώδη χαρακτηριστικά μελετήθηκαν με ποροσιμετρία αζώτου, και η δυνατότητα προσρόφησης διοξειδίου του άνθρακα για όλα τα δείγματα διερευνήθηκε μέσω της καταγραφής ισοθέμων προσρόφησης στους 273 K και 298 K, μέχρι 1 bar. Καταφέραμε να δείξουμε ότι η λυοφιλίωση ενισχύει σημαντικά το πορώδες σε σχέση με την ξήρανση σε αέρα, και ότι η μορφολογία αυτή μπορεί να οδηγήσει σε ενισχυμένη ικανότητα προσρόφησης διοξειδίου του άνθρακα εάν επιλεγεί το βέλτιστο φορτίο παράγοντα υποστύλωσης.

Το Κεφάλαιο 5 επικεντρώνεται σε μια διαφορετική περιβαλλοντική πρόκληση, την απομάκρυνση του υδρόθειου. Με βάση την αποδεδειγμένη απόδοση των πορωδών μητρών σε διαδικασίες αποθείωσης όταν αυτές συνδυάζονται με οξείδια μετάλλων, η χρήση εμπλουτισμένου με χαλκό πορώδη κυβοειδή άνθρακα για δέσμευση υδρόθειου παρουσιάζεται για πρώτη φορά. Μέσω μιας αντίδρασης συντονισμού η οποία ακολουθήθηκε από ένα στάδιο πυρόλυσης, τρία διαφορετικά δείγματα παρασκευάστηκαν: μία δομή πλούσια σε χαλκό αλλά με χαμηλή ειδική επιφάνεια, μία μορφή άνθρακα με υψηλό πορώδες αλλά χωρίς προσθήκη μετάλλου, και τέλος την ίδια μορφή πορώδους άνθρακα αλλά αυτή τη φορά διακοσμημένης με χαλκό. Τα πορώδη χαρακτηριστικά των δειγμάτων μελετήθηκαν με ανάλυση προσρόφησης-εκρόφησης αζώτου, και η περιεκτικότητά τους σε μέταλλο προσδιορίστηκε με θερμική ανάλυση. Η φασματοσκοπία φωτοηλεκτρονίων ακτίνων-X έδωσε πληροφορίες για την στοιχειακή σύνθεση και το χημικό περιβάλλον των στοιχείων, ενώ η μορφολογία των νέων ροφητικών μέσων μελετήθηκε με μικροσκοπία SEM. Για να διερευνηθεί το πώς η υψηλή ειδική επιφάνεια

και η παρουσία οξειδίου του χαλκού μπορούν να εξισορροπηθούν, και το πώς επηρεάζουν συνεργατικά την απομάκρυνση του υδρόθειου, η απόδοση των πορωδών κυβοειδών ανθράκων αξιολογήθηκε με ένα πείραμα χημειορόφησης υδρόθειου στους 150 °C. Τα ροφητικά με το υψηλότερο πορώδες έδειξαν μικρότερη ικανότητα ρόφησης και ήταν παράλληλα καταλυτικά ενεργά. Το πλούσιο σε χαλκό αλλά με χαμηλή ειδική επιφάνεια δείγμα αποδείχτηκε ότι λειτουργεί επίσης ως καταλύτης, με επιλεκτική οξείδωση του υδρόθειου να λαμβάνει χώρα. Το δείγμα αυτό μελετήθηκε περαιτέρω και παρουσιάστηκαν ιδέες για τον πιθανό μηχανισμό που κρύβεται πίσω από την καταλυτική δραστηριότητα. Περαιτέρω βελτίωση των υλικών που σχεδιάστηκαν, θα μπορούσε να οδηγήσει σε καταλύτες υψηλής απόδοσης κατάλληλους για μετατροπή υδρόθειου.

Στοχεύοντας στην επαναχρησιμοποίηση αποβλήτων για την ανάπτυξη υψηλής απόδοσης ροφητικών υλικών, στο Κεφάλαιο 6 παρουσιάζεται για πρώτη φορά μία σειρά καινοτόμων ιεραρχημένων πορωδών ανθράκων (πορώδεις άνθρακες που συνδυάζουν και τα τρία είδη πορώδους) οι οποίοι συντέθηκαν με την ενσωμάτωση αποβλήτων ζάχαρης και καφέ. Τέσσερα είδη πορώδους άνθρακα αναπτύχθηκαν συνολικά: ένα που χρησιμοποιεί λύματα μελάσας σε συνδυασμό με διοξείδιο του πυριτίου ως σύνθετο αρχικό υλικό, ένα που χρησιμοποιεί απόβλητα εκχυλισμάτων ριζών ζαχαρότευτλων και διοξείδιο του πυριτίου, ένα τρίτο, όπου χρησιμοποιημένοι κόκκοι καφέ χρησίμευσαν ως ενίσχυση σε μια προσπάθεια εισαγωγής λειτουργικών ομάδων που θα μπορούσαν να είναι επωφελείς για μελλοντικές εφαρμογές, και ένα τελευταίο όπου δύο είδη αποβλήτων (μελάσα και χρησιμοποιημένοι κόκκοι καφέ) συνδυάστηκαν. Οι ιδιότητες και τα επιφανειακά χαρακτηριστικά όλων των παραγόμενων ιεραρχημένων πορωδών ανθράκων μελετήθηκαν με ποροσιμετρία αζώτου και ηλεκτρονική μικροσκοπία σάρωσης. Επιτεύχθηκαν ειδικές επιφάνειες στο εύρος των 260-1009 m<sup>2</sup>/g. Τρία από τα δείγματα υποβλήθηκαν σε φυσική ενεργοποίηση με διοξείδιο του άνθρακα, που είχε ως αποτέλεσμα τη μεγιστοποίηση της ειδικής επιφάνειας έως και κατά 127 % μετά την εισαγωγή μικροπορώδους. Όλα τα δείγματα παρουσιάζουν μεγάλες δυνατότητες και θα μπορούσαν να είναι ιδανικοί υποψήφιοι για εφαρμογές προσρόφησης και πυκνωτών, καθώς και αποκατάστασης λιμασμένων υδάτων.

## Acknowledgements

It has been a long trip, full of experiences, both positive and negative, that have formed me as a researcher and a person. There is a long list of people that have contributed to this journey to whom I would like to express my gratitude because it would not have been possible without their scientific or emotional contribution and support to reach the finish line and be holding this thesis in our hands.

This trip started 5 years ago with me asking my then daily supervisor for advice about whether I should do a PhD in Greece or abroad and she told me ‘You may find the best lab and the best university, but you will never find a better ‘teacher’ than Gournis’. There has not been one single day that I did not feel lucky to be under the caring supervision of **Dimitris Gournis**. I would never find enough words to describe my immense gratitude towards you. You have been a great mentor and teacher to me all these years. You helped me identify my strengths and weaknesses, and you taught me how to enjoy doing research keeping a healthy life-work balance. Working all those years by your side I have won a lot as a person and as a researcher, and you have always felt more like family than a supervisor. During my time abroad talking on the phone with you was always a boost of positivity.

After completing the first two years and moving to the Netherlands I got to work closely with my second supervisor **Petra Rudolf**. You pushed me out of my comfort zone, you made me test my limits and believe in my own potential and realize that nothing is impossible. You are an inspiring role model and working by your side I have acquired a lot of important skills; I became better at managing and completing tasks as well as communicating my research. Thank you for being patient with me, especially during the times that I was overwhelmed by stress and nerves, and for all the advice and efficient guidance you have provided me with. Also, I will always be grateful to both you and **Valerio** for the warmest welcome to the Netherlands and for the beautiful Christmas dinners you have organized for the group.

Next in line cannot be other than my daily supervisor **Kostas Spyrou**. I first met you on the day of my bachelor thesis defence, when you pointed

at all the mistakes I had done during the presentation. You guided me through my master and my PhD (maybe I should thank technology since the close supervision was possible even though we managed to be in different cities, countries or continents most of the time), we worked together on really interesting projects (I had never thought I would use eggs or pears in the chemistry lab or that I would set the lab fire alarm off by using a microwave oven), you taught me a lot about XPS and it was a comfort and reassurance knowing that I can count on your help 24/7 all these years.

The end of the journey seemed to be coming closer the day that this thesis reached the hands of the assessment committee. Prof. **Paolo Pescarmona**, Prof. **Alkiviadis Paipetis**, Prof. **George Froudakis** and Prof. **Cinzia Casiraghi**, thank you for your constructive comments and suggestions, and for agreeing to be part of this procedure.

Prof. **Michael Karakassides** and Dr. **George Romanos**, who formed alongside Gournis my three membered advisory committee and have contributed with their help whenever it was needed.

If I have to highlight one part of this journey, it is the importance of the Greek porous family (this is how I always have in my mind all of you who form this network). Most of my projects needed porosity measurements, and since the equipment arrived at our lab after I moved abroad, I had to make use of our network and spread my samples all over Greece. The labs of Prof. **Kostas Triantafyllidis**, Dr. **Theodore Steriotis**, Dr. **Georgia Charalambopoulou**, and Prof. **Pantelis Trikalitis** were always 'open' for me; my collaboration with all of you has been extremely valuable and pleasant, and I have learnt a lot. Special thanks to **Christos Tampaxis** for his patience and help with the measurements!

Prof. **George Evangelakis**, who warmly welcomed me into his XPS lab at the Physics department in Ioannina and together with **Kostas Prouskas** helped me every time I needed assistance with the setup. **Nikos Panagiotopoulos** and **Konstantina** made the time spent there even more pleasant.

All the people that made completing each one of my projects possible by either teaching me new methods and techniques or by performing measurements for me: **Christina Papachristodoulou**, who I had been



bombarding with XRD samples over the years; **Jur van Dijken** for all the TGA measurements that he performed for me; **Reinder de Vries** for helping me out with the freeze-drying equipment; **Kyriaki Tsirka** for the Raman measurements; Prof. **Alexandros Karantzalis** for teaching me how to use the SEM; Prof. **Yutao Pei** and **Liqiang Lu** for the wonderful SEM images; **Léon Rohrbach** for training me and always being pleasant and eager to help with the porosity measurements; Prof. **Edita Jurak** for the anion exchange chromatography analysis; Prof. **Wesley Browne** for the Raman training; The always kind **Jacob Baas** for the XRD training and for always trying to find solutions when I sought his help; **Kostas Dimos** for teaching me how to use the XPS in Ioannina.

Our secretary at the University of Ioannina, **Konstantina Kokkali**, and our secretary at the STF group, **Hilda Riemens**; **Annette Korringa**, **Ingrid Veltman**, all the people working at the PhD Scholarship Desk, as well as **Savvas Dimitriadis**, **Eleni Zogaki** and **Alexia Zotou** at the Research Committee of the University of Ioannina, who always were there to offer me help with official matters and bureaucracy whenever I needed them, making life a bit easier.

Throughout all these years, I was given the opportunity to be introduced to both of my supervisors' networks and collaborate with many excellent researchers, some of whom I also had the joy to collaborate with in publications: **Georgios Karanikolos**, **Yasser Al Wahedi**, **Andreas Sapalidis**, Prof. **Haris Stamatis** (and all of his lab members for always being good neighbours to us, especially **Vaso** and **Alexandra**), Prof. **Petros Katapodis**, **Nikos Rigopoulos**, Prof. **Dimitris Tasis**, Prof. **Dimitrios Bikiaris**, Prof. **Katja Loos**, Prof. **Athanasios Bourlinos**, Prof. **Vasilis Kyriakou**, Prof. **Konstantinos Salmas**, Prof. **Simeon Agathopoulos**, Prof. **Apostolos Avgeropoulos** (and all of the former and present members of his lab for the fruitful collaboration)

Doing a PhD means spending more time in the lab than with family and friends, and for this reason it is important to work in a pleasant environment surrounded by good colleagues. Therefore, I would like to thank all former and present members of the Layered and Nanoporous Materials Group and the Surfaces and Thin Films Group. I would like to specifically mention **Antonis**, **Nikos** and **Christina**.

**Georgia Basina:** your passion and dedication has always been an inspiration for me, and I feel lucky we have collaborated, since I highly appreciate you as a scientist and as a person. Our conversations and your advice have been really valuable for me.

Those who know me well, know that being surrounded by people and interacting with them in my daily life is important to me, so at this point I would like to thank all the people that I have briefly collaborated with, who were kind enough to provide help on campus, or with whom I have shared coffee and conversations especially on these gloomy days that everything seemed to go wrong on the experimental side and I just needed to chat with someone: **Jane, Mithyzi, Dina Boer, Zhiwen, Matteo, Aldo, Marco, Maryam, Saurabh, Qi, Apostolos, Ioannis, Lorenzo, Anna, Chognan, Nikolina, Aggelos, Lefteris, Elina, Doris, Mohammad, Jordi, Laura, Masyitha, Dina Maniar, Apostolis.**

**Miki,** for your professionalism and efficiency.

**Ali,** for welcoming me to Groningen and always being cheerful and happy to help. We have spent a nice time inside and outside the lab (especially the trips) with you and your family (sweet **Liany** – my ACLO partner, and little **Cici**) and I promise I will never forget the chicken feet you cooked for me, haha.

**Oreste,** thank you for trying to be an octopus and have hands on all equipment at the same time and for keeping all machines alive and running for us to finish our projects. And for all the nice dinners, walks and guitar sessions!

**Charmaine,** for all the good moments we have shared together (being housemates, office mates, sharing nice wine, working out in ACLO together, carrying huge furniture and partying together even when there was no party, hehe) and of course for the lovely nephew you have given us: **Nyasha.**

My fellow sufferers **Feng** and **Hamoon.** It seemed impossible at times, but we made it! Hehe! Thank you both for sharing all this experience and trying to give courage to each other. Feng, thank you for your originality and for the interesting conversations we have shared over coffee or drinks. And the delicious hot-pots of course!

The Greeks: **Theodosios**, **Lorena**, **Panagiotis** and **Eugenios** for all the good moments we shared!

My friends **Elli**, **Vlasis** and **Sotiris** for all the nice football weekends that we shared in the first half of my PhD following our favourite PAS around Greece and which I have really missed.

My good friend **Lefkothea** for always being there, **Akis** for the endless number of cups of coffee we shared, **Georgia**, **Mihalis** and **Xanthipi** for the refreshing getaway weekends, **Sara** for helping me into a healthier way of life.

Mi querida **Estela**: You said that I was a Deus ex machina for you when I arrived at Zernike, but I think it was the other way around. I always admired your knowledge, dedication to learning and enthusiasm about everything. You were a positive anchor for me, and you were always able to brighten up my day. Thank you also for taking me to the most unexpected places and for showing me nice spots in Groningen.

**Dimitra**, for being such a good friend and support, and always making me face reality whenever someone needed to do it. We have shared our parallel PhD journeys trying to cope with failure and emotions, talking and finding comfort in each other. Our conversations have always been important for me and there were countless days that I wished we could relax and chat drinking coffee together.

**Fedor**, for all the gezelligheid, the nice excursions and the lekker snackjes that helped me get through the last and more stressful months of my PhD.

My crazy friend **Antonis**: I am glad I spotted you on your first day at our campus and for having you around ever since. We have spent really nice moments together; nice dinners, nice (?) muffins, baking Greek delicacies. Coffee breaks with you would always cheer me up, you showed me all the tricks of the Dutch system, and it is nice having someone to share my suffering whenever PAS is playing :D

My friend **Bouke**: Thank you for all the deep conversations we have had, for always being direct with me and making me open up and talk more about what I think, trying to make me happy with your buyitos, pushing me out of my comfort zone and for being a kind of life coach to me. I value our friendship a lot.

My first bachelor student and friend, **Viktoria Sakavitsi**: I was a bit scared when I had to start supervising for the first time, but we instantly understood we had a natural fit, and our collaboration has always been pleasant and productive. It has been a joy to guide you through your bachelor and master theses and now see you doing your PhD as well. You are a good and fast learner and it is comforting to know I have a 'right hand' I can trust with experimental procedures. You have helped me a lot during these 5 years, even from far away. Most people know you as 'Ela', since they would hear me replying to one of our numerous daily phone calls.

Sometimes the right people enter unexpectedly into your life when you most need it; one of them is **Semina**. It is quite strange for me to be so close with you, only having interacted in person so little. Maybe the fact that we have been born on the same day means something, maybe not, but either way I felt like I found a soul mate, someone that completely understands how I feel and act. You would always come to the rescue every time there was a porosity emergency (teaching me a lot and not only solving my problem), you gave me a lot of strength all these past months and I hope that our daily conversations have been for you as beneficial as they have been for me.

In the mid of the PhD and pandemic madness I got to be the maid of honour in the wedding of my two beloved friends **Vasilis** and **Kyriaki-Marina**. I met both of you in the beginning of my master and you have both been excellent colleagues (Vasilis, I learned a lot working by your side in the lab, and Marina, you were the best lab partner I could ask for) and supporting friends all these years, and from now on it is just an honour and pleasure to be able to consider you family.

Mi carissima **Giovanna**: What can I say for you? I think that having survived sharing the same office and the same house for the last 1.5 years (once in a box, always in a box), celebrating together birthdays, name days, Easters, and Christmas, ringing on the wrong doorbells, coping with a heavy winter and a pandemic (I know that coping with my mood and incessant talking might have been even harder than all of these combined, even being spat at), does say a lot. Despite my complaining, I feel lucky to have had a little chef at home enjoying delicious meals and desserts that everyone is jealous of (your pizza is one of the best I have tried, no matter

what you say). I might still be listed as ‘Lena lab’ in your contacts, but you feel like a second ‘small’ sister to me, and I feel very lucky to have you around as a friend and see you grow as a scientist. I cannot even imagine how I would have coped all this time without you. ΣΕ ΕΥΧΑΡΙΣΤΩ.

Last but not least, my family: My beloved grandfather **Giannis**, my dad **Kostas**, my mom **Athena**, and my sister **Iphigenia**. The ones that are always there supporting me no matter what, even though they are still struggling to understand what I do in the lab and wondering what I am doing there all day long. Their patience and love have always been unconditional.



## List of publications

1. Graphene/Carbon Dot Hybrid Thin Films Prepared by a Modified Langmuir–Schaefer Method, A. Kouloumpis, **E. Thomou**, N. Chalmpes, K. Dimos, K. Spyrou, A.B. Bourlinos, I. Koutselas, D. Gournis and P. Rudolf, *ACS Omega* **2017**, 2, 2090–2099
2. Co-N Doped Reduced Graphene Oxide As Oxygen Reduction Electrocatalyst Applied To Photocatalytic Fuel Cells, D. Raptis, A. Ploumistos, E. Zagoraiou, **E. Thomou**, M. Daletou, L. Sygellou, D. Tasis and P. Lianos, *Catalysis Today* **2018**, 315, 31-35
3. Optimization of Silver Nanoparticle Synthesis by Banana Peel Extract Using Statistical Experimental Design, and testing of their Antibacterial and Antioxidant Properties, N. Rigopoulos, **E. Thomou**, A. Kouloumpis, E.R. Lamprou, V. Petropoulea, D. Gournis, E. Poulis, H.C. Karantonis and E. Giaouris, *Current Pharmaceutical Biotechnology* **2019**, 20, 10
4. Antibacterial and Algicidal Effects of Porous Carbon Cuboid Nanoparticles, D. Karageorgou, **E. Thomou**, N. T. Vourvou, K.-M. Lyra, N. Chalmpes, A. Enotiadis, K. Spyrou, P. Katapodis, D. Gournis and H. Stamatis, *ACS Omega* **2019**, 4, 3, 4991-5001
5. Highly conductive metallic state and strong spin-orbit interaction in annealed germanane, Q. Chen, L. Liang, G. Potsi, P. Wan, J. Lu, T. Giousis, **E. Thomou**, D. Gournis, P. Rudolf and J. Ye, *Nano Letters* **2019**, 19, 3, 1520-1526
6. Enzymatic Conversion of Oleuropein to Hydroxytyrosol Using Immobilized  $\beta$ -Glucosidase on Porous Carbon Cuboids, A. V. Chatzikonstantinou, E. Gkantzou, **E. Thomou**, N. Chalmpes, K.-M. Lyra, V. G. Kontogianni, K. Spyrou, M. Patila, D. Gournis and H. Stamatis, *Nanomaterials* **2019**, 9, 1166
7. Smectite clay pillared with copper complexed polyhedral oligosilsesquioxane for adsorption of chloridazon and its metabolites, F. Yan, K. Spyrou, **E. Thomou**, S. Kumar, H. Cao, M. C. A. Stuart, Y. Pei, D. Gournis and P. Rudolf, *Environmental Science: Nano* **2020**, 7, 424-436
8. Lipase immobilized on magnetic hierarchically porous carbon materials as a versatile tool for the synthesis of bioactive quercetin derivatives, A. V. Chatzikonstantinou, A. C. Polydera, **E. Thomou**,

- N. Chalmpes, T. N. Baroud, A. Enotiadis, L. Estevez, M. Patila, M. A. Hammami, K. Spyrou, E. P. Giannelis, A. G. Tzakos, D. Gournis and H. Stamatis, *Bioresource Technology Reports* **2020**, 9, 100372
9. Advances in Fluorescent Carbon Dots for Biomedical Applications, P. Koutsogiannis, **E. Thomou**, H. Stamatis, D. Gournis and P. Rudolf, *Advances in Physics: X* **2020**, 5, 1, 1758592
  10. On the selective oxidation of H<sub>2</sub>S by heavy loaded Nanoparticles Embedded in Mesoporous Matrix (NEMMs), G. Basina, O. Elmutasim, D. Gaber, S. Gaber, X. Lu, V. Tzitzios, B. V. Vaithilingam, M. Baikousi, G. Asimakopoulos, M. A. Karakassides, I. Panagiotopoulos, K. Spyrou, **E. Thomou**, E. Sakelis, N. Boukos, D. Xu, M. Tsapatsis, N. Al Amodi, *Applied Catalysis B: Environmental* **2020**, 278
  11. New Porous Heterostructures Based on Organo-Modified Graphene Oxide for CO<sub>2</sub> capture, **E. Thomou**, E. K. Diamanti, A. Enotiadis, K. Spyrou, E. Mitsari, L. G. Boutsika, A. Sapolidis, E. Moretón Alfonsín, O. De Luca, D. Gournis and P. Rudolf, *Frontiers in Chemistry* **2020**, Vol. 8, Article 564838
  12. Highly Efficient Remediation of Chloridazon and Its Metabolites: The Case of Graphene Oxide Nanoplatelets, F. Yan, S. Kumar, K. Spyrou, A. Syari'ati, O. De Luca, E. Thomou, E. Moreton Alfonsín, D. Gournis and P. Rudolf, *ACS EST Water* **2021**, 1, 1, 157-166
  13. A diamino-functionalized silsesquioxane pillared graphene oxide for CO<sub>2</sub> capture, **E. Thomou**, V. Sakavitsi, G. K. Angeli, K. Spyrou, K. G. Froudas, Evmorfia K. Diamanti, G. E. Romanos, G. N. Karanikolos, P. N. Trikalitis, D. Gournis and P. Rudolf, *RSC Advances* **2021**, 11, 13743-13750
  14. H<sub>2</sub>S removal by copper enriched porous carbon cuboids, **E. Thomou**, G. Basina, K. Spyrou, Y. Al Wahedi, P. Rudolf and D. Gournis, submitted to *Carbon Trends*, 30/08/2021
  15. MgH<sub>2</sub> nanoparticles confined in reduced graphene oxide pillared with organosilica: a novel type of hydrogen storage material, F. Yan, E. Moreton Alfonsín, P. Ngene, S. de Graaf, O. De Luca, H. Cao, K. Spyrou, L. Lu, **E. Thomou**, Y. Pei, B. J. Kooi, D. Gournis, P. E. de Jongh and P. Rudolf (to be submitted)



## The author

Born in Ioannina (Greece) on the 27<sup>th</sup> of May 1988, Eleni Thomou obtained her first Degree (Dipl. Eng.) in Materials Science and Engineering at the University of Ioannina in 2013. In 2016, she completed a two-year cross-departmental master course programme in Materials Chemistry and Technology at the University of Ioannina. Her research project aimed at the development and study of novel hybrid superstructures and nanoporous materials based on carbon and was

performed in the Ceramics and Composites Laboratory under the supervision of Dr. Dimitrios Gournis. She then started a joint PhD programme between the Department of Materials Science and Engineering of the University of Ioannina and the Zernike Institute for Advanced Materials of the University of Groningen (Netherlands) under the supervision of Dr. Petra Rudolf and Dr. Dimitrios Gournis. Her daily supervisor was Dr. Konstantinos Spyrou.

